NASA TechBriefs

National Aeronautics and
Space Administration
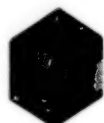
- ▷ Electronic Components and Circuits

- Electronic Systems

- Physical Sciences

- Materials

- Computer Programs

- Mechanics

- ✿ Machinery

- Fabrication Technology

- Σ Mathematics and Information Sciences

- Life Sciences

95-026003

INTRODUCTION

Tech Briefs are short announcements of new technology derived from the research and development activities of the National Aeronautics and Space Administration. These Briefs emphasize information considered likely to be transferable across industrial, regional, or disciplinary lines and are issued to encourage commercial application.

Availability of NASA Tech Briefs and TSP's

Distribution of NASA Tech Briefs, a monthly periodical publication, is limited to engineers in U.S. Industry and to other domestic technology transfer agents. Requests for individual Tech Briefs or for Technical Support Packages (TSP's) announced herein should be addressed to

NASA Center for AeroSpace Information
Technology Utilization Office
P.O. Box 8757
Baltimore, MD 21240.
Telephone No. (301) 859-5300, Ext. 243, 245

Please reference the three-letter, five-digit control number located at the end of each Tech Brief. Information on NASA's Technology Utilization Program, its documents, and services is also available at the same facility.

Technology Utilization Officers and Patent Counsels are located at NASA field installations to provide technology-transfer access to industrial users. Inquiries can be made by writing to NASA field installations listed below.

Technology Utilization Officers and Patent Counsels

Ames Research Center
Technology Utilization Officer
Mail Code 223-3
Moffett Field, CA 94035

Patent Counsel
Mail Code 200-11
Moffett Field, CA 94035

Goddard Space Flight Center
Technology Utilization Officer
Mail Code 702-1
Greenbelt, MD 20771

Patent Counsel
Mail Code 204
Greenbelt, MD 20771

Lyndon B. Johnson Space Center
Technology Utilization Officer
Mail Code IC-4
Houston, TX 77058

Patent Counsel
Mail Code AL3
Houston, TX 77058

John F. Kennedy Space Center
Technology Utilization Officer
Mail Stop PT-PMO-A
Kennedy Space Center, FL 32899

Patent Counsel
Mail Code PT-PAT
Kennedy Space Center, FL 32899

Langley Research Center
Technology Utilization Officer
Mail Stop 143
Hampton, VA 23665

Patent Counsel
Mail Code 279
Hampton, VA 23665

Lewis Research Center
Technology Utilization Officer
Mail Stop 7-3
21000 Brookpark Road
Cleveland, OH 44135

Patent Counsel
Mail Code LE-LAW
21000 Brookpark Road
Cleveland, OH 44135

Jet Propulsion Laboratory
Technology Utilization Officer
Mail Stop 156-211
4800 Oak Grove Drive
Pasadena, CA 91109

NASA Resident Office-JPL
Technology Utilization Officer
Mail Stop 180-801
4800 Oak Grove Drive
Pasadena, CA 91109

Patent Counsel
Mail Code 180-801
4800 Oak Grove Drive
Pasadena, CA 91109

George C. Marshall Space Flight Center
Technology Utilization Officer
Code AT01
Marshall Space Flight Center, AL 35812

Patent Counsel
Mail Code CC01
Marshall Space Flight Center, AL 35812

John C. Stennis Space Center
Technology Utilization Officer
Code HA-30
Stennis Space Center, MS 39529

NASA Headquarters
Technology Utilization Officer
Code CU
Washington, DC 20546

Assistant General
Counsel for Patent Matters
Code GP
Washington, DC 20546

Dryden Flight Research Center
Technology Utilization Officer
M/F D21-31
Bldg. 4832 Whse 7
Lily Dr.
Edwards, CA 93523

BLANK PAGE

2

Electronic Components and Circuits

Hardware, Techniques, and Processes

Cheap, Easy-To-Read Frequency Monitor for Pulsed Laser

A simple bar-graph display shows the approximate relative frequency at a glance.

NASA's Jet Propulsion Laboratory, Pasadena, California

The figure illustrates an electronic circuit that provides a bar-graph display of the difference between the carrier frequency of a pulsed laser transmitter and the frequency of another laser that serves as the local oscillator in a receiver. The display device is a linear array of light-emitting diodes (LED's), each of which represents a 1-MHz portion of the beat-frequency range from 20 to 40 MHz. The middle LED represents the frequency of 30 MHz, which lies at the middle of the passband of the receiver. The middle LED and its neighbors are green; the LED's that represent the edges of the passband are yellow; the LED's of frequencies outside the passband are red. Thus, the operator can determine the approximate relative frequency of the transmitter at a glance by observing the color and position of the illuminated LED.

In the pulsed-lidar system for which the frequency monitor was designed, the pulse-repetition frequency is about 4 Hz. Typically, the carrier frequency jitters about 1 MHz, from pulse to pulse. It is much easier to read this bar-graph display than it would be to read a more-precise digital frequency display because the reader does not have to process mentally the many digits that would change repeatedly at the pulse-repetitionpulserepetition rate. In addition, the incremental linear display enhances the operator's perception of the jitter and overall excursion from the middle frequency.

The monitor is based on heterodyne and gated-counter concepts. In the photodetector of the receiver, part of the scattered transmitter signal is mixed with the local-oscillatorlocaloscillator signal, producing the beat-frequency (intermediate-frequency) receiver signal. Some of the beat-frequency signal is diverted from the receiver to the monitor, where a high-speed comparator generates transistor/transistor-logic-level pulses at the beat-frequency rate. These pulses are fed to the clock-input terminal of a binary counter. The count is started, stopped, and reset to zero during each transmitter
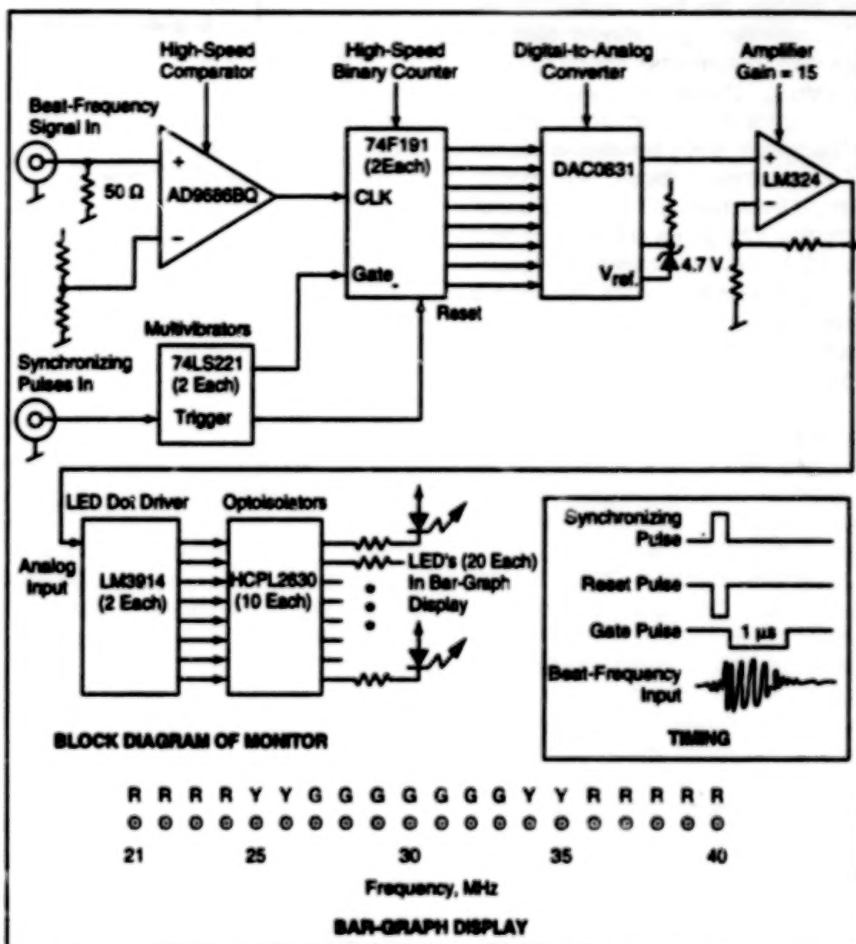
The Frequency Monitor counts the number of cycles during a 1ms portion of the beat-frequency pulse associated with each transmitter pulse (which lasts somewhat longer than 1 ms). One of the LED's in the linear array is illuminated; its position represents the number of cycles and, therefore, the relative carrier frequency of the transmitter.

pulse by two multivibrators that are triggered by a synchronizing pulse from the transmitter. The counting period is 1 ms If, for example, the count is 30 at the end of the period, then the average frequency during the period was about 30 MHz.

The output of the binary counter is converted to an analog voltage, then redigitized by an LED-dot-bar driver the frequency increments of the display. (This approach results in a simpler circuit than does an all-digital approach.) The output of the LED-dot-bar driver is fed to a set of

optoisolators, which drive the LED's in the display. To enable verification that the bar-graphbargraph display is calibrated, a digital readout is also provided. However, the bar-graph display is meant to be the focus of attention at high pulse-repetition rates.

This work was done by Carlos Esproles of Caltech for **NASA's Jet Propulsion Laboratory.** *Further information is contained in a TSP [see page 1].*
NPO-18596

Preventing Overcharge and Overdischarge of Lithium Cells

Cathode additives act as sinks or sources of lithium.

NASA's Jet Propulsion Laboratory, Pasadena, California

Secondary lithium cells that operate at ambient temperature can be protected against overcharge and overdischarge by

use of cathode additives that act as the sources and sinks of the electroactive chemical species, which is lithium. The

additive in a cathode limits the excursion of the voltage of the cell during both overcharge and overdischarge. In addition to

protecting the cell, the additive thus also serves as part of a state-of-charge indicator: the attainment of the greater or lesser limiting voltage indicates the end of charge or end of discharge, respectively. This concept has been applied to the Li/TiS_2 system, and should also be applicable to such other lithium systems as Li/MoS_2, $Li/NbSe_3$, and Li/V_2O_5.

The cycle-life performance of the Li/TiS_2 system is very sensitive to the limits of operating voltages, the recommended limits being 2.7 V for the end of discharge. Charging a cell to more than about 2.8 V results in oxidative degradation of the electrolyte solvent; discharging to less than about 1.5 V results in irreversible intercalation of Li into TiS_2 and reduction of the electrolyte salt. This limits the cycle-life performance of the cell. Repeated overcharge and overdischarge have also been found to result in venting or explosion of cells. Hence, there is a need for built-in means to prevent both overcharge and overdischarge.

A cathode additive that can protect against both overcharge and overdischarge may contain one or two materials that, in combination, exhibit the following characteristics: (1) The additive must be capable of undergoing a reversible reaction with lithium. (2) The lithium-titration curve of the additive must contain two well-defined voltage plateaus separated by about 1 V. (3) The upper plateau voltage of the additive must slightly exceed the charge cutoff voltage of the cathode material. (4) The lower plateau voltage of the additive must be slightly less than the discharge cutoff voltage of the cathode material. (5) If the additive is a single compound, it should preferably be one that exhibits a sharp transition from one plateau to the other. (6) The additive must be chemically stable in the presence of the cathode active material and the electrolyte. (7) The additive must be highly conductive with respect to electrons and lithium ions.

The titration curve of TiS_2 cathode material and an ideal single-compound cathode additive is shown in Figure 1, which illustrates the range of operating voltages of the TiS_2 and the range of voltages that lie within the protective capability of the additive material. During overcharge (an attempt to charge the cell to more than the upper plateau value of 2.7 V), the additive material is activated and keeps the cell voltage from rising above 2.7 V. During overdischarge (an attempt to discharge the cell to less than the lower plateau voltage of 1.7 V), the additive is also activated and keeps the cell voltage from falling below 1.7 V.
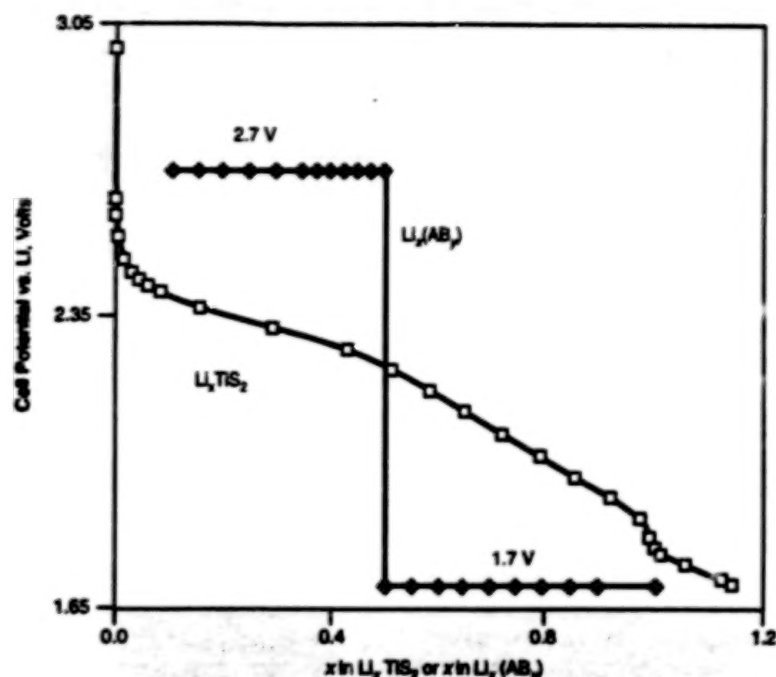
Figure 1. The Coulometric Titration Curves of Li in TiS_2 cathode materials is shown along with that of an ideal additive compound AB_y that would protect an Li/TiS_2 cell against both overcharge and overdischarge.
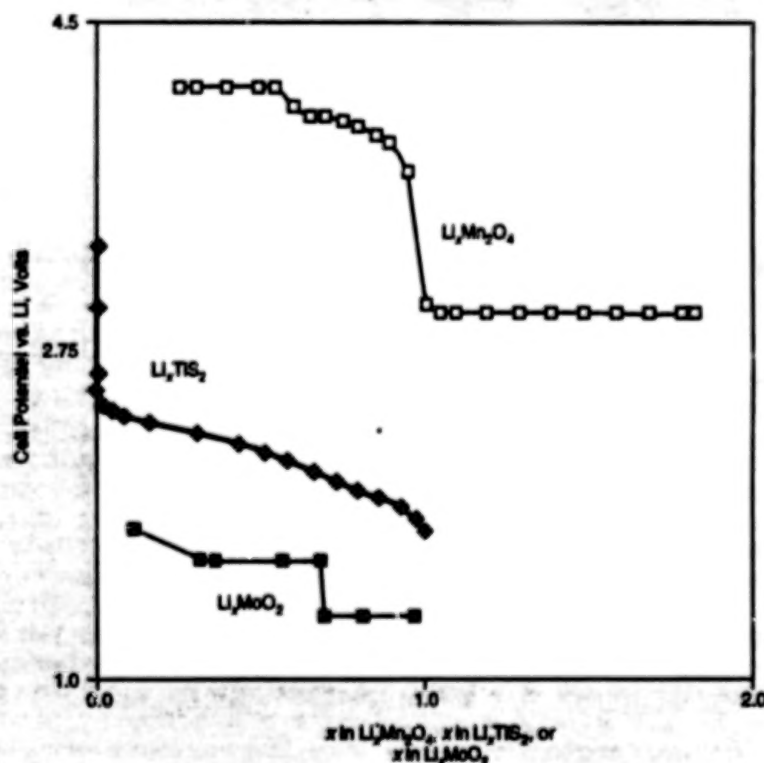
Figure 2. The Two-Compound Additive Mixture of $Li_2Mn_2O_4$ and $Li_{0.1}MoO_2$ protects an Li/TiS_2 cell against both overcharge and overdischarge, as can be seen from the coulometric titration curves of Li in TiS_2, Mn_2O_4, and MoO_2.

Theoretically, these requirements could be met by an additive that consists of one or two individual compounds (transition-metal oxides or sulfides).

One example of an additive that consists of two compounds is a mixture of $Li_2Mn_2O_4$ and $Li_{0.1}MoO_2$. The $Li_xMn_2O_4$ system exhibits an upper plateau volt-

age around 2.9 V (vs. Li), and thus protects the cells against overcharge; the Li_xMoO_2 system exhibits a lower plateau voltage around 1.6 V (vs. Li), and thus protects the cells against overdischarge (see Figure 2).

Tachometer Derived From Brushless Shaft-Angle Resolver

Output is directly proportional to the rate of rotation.   *Marshall Space Flight Center, Alabama*

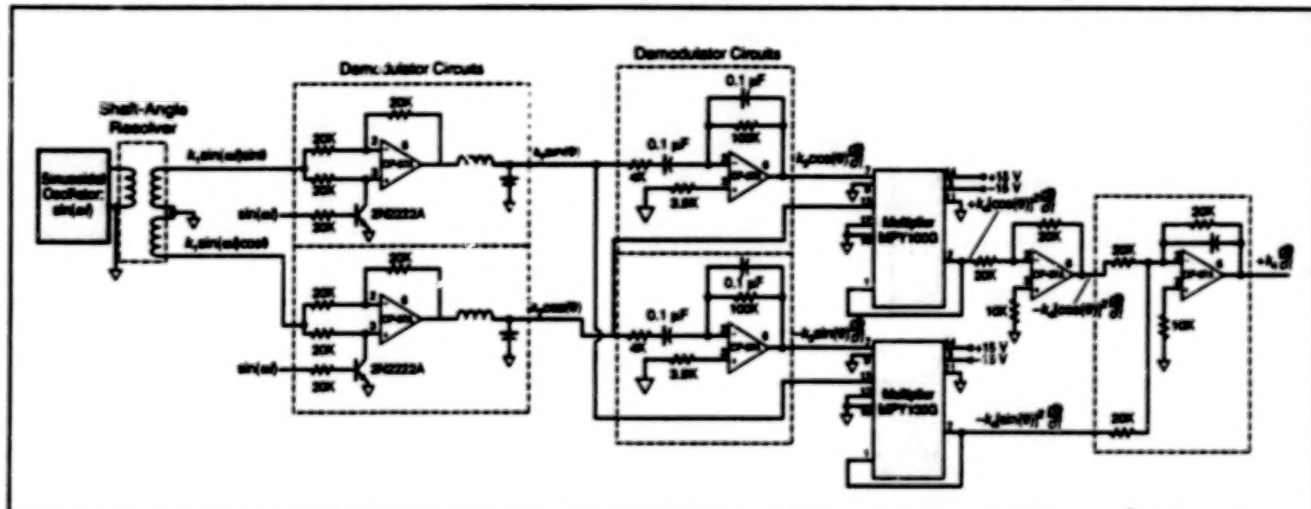The **Tachometer Circuit** operates in conjunction with a brushless shaft-angle resolver. By performing a sequence of straightforward mathematical operations on the resolver signals and utilizing a simple trigonometric identity, it generates a voltage proportional to the rate of rotation of the shaft.

The figure illustrates an analog tachometer circuit that processes the input and output signals of a two-phase, brushless, transformer-type shaft-angle resolver into a signal with instantaneous amplitude proportional to the instantaneous rate of rotation of the shaft. The processing in this circuit effects a straightforward combination of mathematical operations leading to a final operation based on the well-known trigonometric identity $[\sin(x)]^2 + [\cos(x)]^2 = 1$ for any value of x. This circuit is related to a tachometer circuit, described previously in *NASA Tech Briefs* and based on the same mathematical principles, that required two shaft-angle resolvers. By eliminating the need for a second resolver, the present circuit reduces the overall size, weight, and cost of the tachometer.

As is customary, the resolver is excited with a periodic waveform; a sinusoid is indicated in the figure, but a square, triangular, or other periodic waveform could be used instead. Thus, the two outputs of the resolver are $k_1\sin(\omega t)\sin(\theta)$ and $k_1\sin(\omega t)\cos(\theta)$, where k_1 is a constant proportional to the amplitude of excitation and to a factor that depends on the geometric and electromagnetic properties of the resolver, ω is $2\pi \times$ the frequency of excitation, t is time, and θ is the instantaneous shaft angle.

The two outputs of the resolver are then processed, along with a replica of the sinusoidal excitation, by demodulators. The two outputs of the demodulators are thus $k_2\sin(\theta)$ and $k_2\cos(\theta)$, where k_2 is a constant proportional to k_1 and to the gain of the demodulators. These signals are then differentiated with respect to time in two differentiator circuits. The outputs of these circuits are thus $k_3\cos(\theta)[d\theta/dt]$ and $-k_3\sin(\theta)[d\theta/dt]$, where k_3 is a constant proportional to k_2 and to the gain of the differentiator circuits. Note that $d\theta/dt$ is the rate of change of the shaft angle and is the quantity that one seeks to measure.

Next, a multiplier circuit forms a product of the demodulator and differentiator outputs proportional to $\sin(\theta)$, while another multiplier circuit forms the product of the demodulator and differentiator outputs proportional to $\cos(\theta)$. The outputs of the multiplier circuits are thus $+k_4[\cos(\theta)]^2[d\theta/dt]$ and $-k_4[\sin(\theta)]^2[d\theta/dt]$, where k_4 is a constant proportional to k_2k_3 and to the gain of the multiplier circuits. The output of the cosine multiplier is fed to a unit-gain inverting amplifier to obtain $-k_4[\cos(\theta)]^2[d\theta/dt]$.

The voltages $-k_4[\sin(\theta)]^2[d\theta/dt]$ and $-k_4[\cos(\theta)]^2[d\theta/dt]$ are fed to an inverting unit-gain adder circuit. By virtue of the trigonometric identity $[\sin(\theta)]^2 + [\cos(\theta)]^2 = 1$

and the inversion, the output of this circuit is simply $+k_4[d\theta/dt]$.

One advantage of this tachometer circuit is the use of a brushless shaft-angle resolver as the main source of the rate signal: there are no brushes to wear out, there is no brush noise, and brushless resolvers have a history of proven robustness. Unlike in some older tachometer circuits, there is no switching of signals to generate noise. Another advantage is that in a typical application, a shaft-angle resolver is already being used as a shaft-angle sensor, and thus the tachometer input can be obtained without adding another sensor. This circuit also offers an advantage over conventional rate sensors based on permanent magnets and windings: If a winding becomes short-circuited, it gives rise to a parasitic drag torque. The present circuit is not susceptible to this type of malfunction.

Combining Video Memory Operations

Designs can be simplified.

Lyndon B. Johnson Space Center, Houston, Texas

The designs of video random-access memory (VRAM) integrated circuits that operate under control by external logic circuits can be simplified according to a concept of combining two memory operations that have been performed separately heretofore.

Usually, a VRAM integrated circuit of the type in question contains a dynamic random-access memory (DRAM) that buffers parallel digital video data from the source, plus a serial data register (SDR) that loads parallel data from the DRAM prior to clocking of this data serially out to a display circuit (see figure). The four main operations of the VRAM are (1) loading the DRAM, (2) refreshing the DRAM, (3) loading the SDR, and (4) clocking data serially out of the SDR. According to older design concepts, only operations 1 and 4 can be performed simultaneously; operations 1, 2, and 3 are performed sequentially because they have to be synchronized with common control signals that an arbiter logic circuit feeds
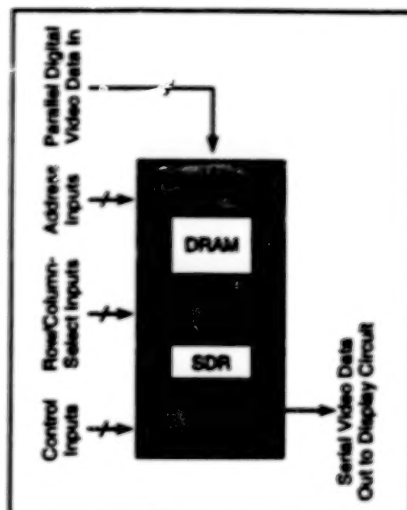
A VRAM Performs Four Main Operations on video data during each operating cycle. Combining two of them simplifies the ancillary control and timing circuitry.

sequentially to the portions of the circuits that effect these operations.

The present simplified design concept can be applied to a VRAM that clocks data out to a display unit continuously. Because operations 2 and 3 occur periodically in continuous clocking, it is possible to combine these operations, provided that a suitable number of rows of the DRAM are refreshed on each cycle. This concept eliminates the need for DRAM-refresh timers and counters, thus reducing the amount of circuitry needed to control the VRAM and thereby also reducing the time needed to design the VRAM. This simplification also reduces the time needed to redesign the DRAM-refresh logic circuitry when adapting a VRAM design to another VRAM for which timing specifications are different.

This work was done by Michael J. Kania and Jim S. Eiche of International Business Machines Corp. for **Johnson Space Center.** *Further information is contained in a TSP [see page 1].*
MSC-22417

Growth of δ-Doped Layer on Silicon CCD

Response to ultraviolet light is enhanced.

NASA's Jet Propulsion Laboratory, Pasadena, California

A back-side-illuminated silicon charge-coupled device has been fabricated that exhibits nearly 100% internal quantum efficiency in the near ultraviolet, by using molecular beam epitaxy to grow a thin crystalline-silicon layer that contains a high concentration of boron (p-type dopant). By confining the dopant atoms to one or a few atomic layers in the silicon lattice, the concentration-vs.-depth profile can be made to resemble the Dirac δ function, and the resulting silicon layer is said to be "δ-doped." In the CCD, the δ-doped layer is located at the back surface of a thinned commercial device (EG&G Reticon RA0512J). The δ-doped layer is formed by stripping the native oxide from the CCD and depositing boron atoms on the heated silicon surface, followed by growing a thin layer of crystalline silicon to encapsulate and protect the dopants from oxidation.

Previously, the growth of thin, precise films by molecular-beam epitaxy on the back sides of preprocessed CCD's was not feasible because of the high processing temperatures that were used.
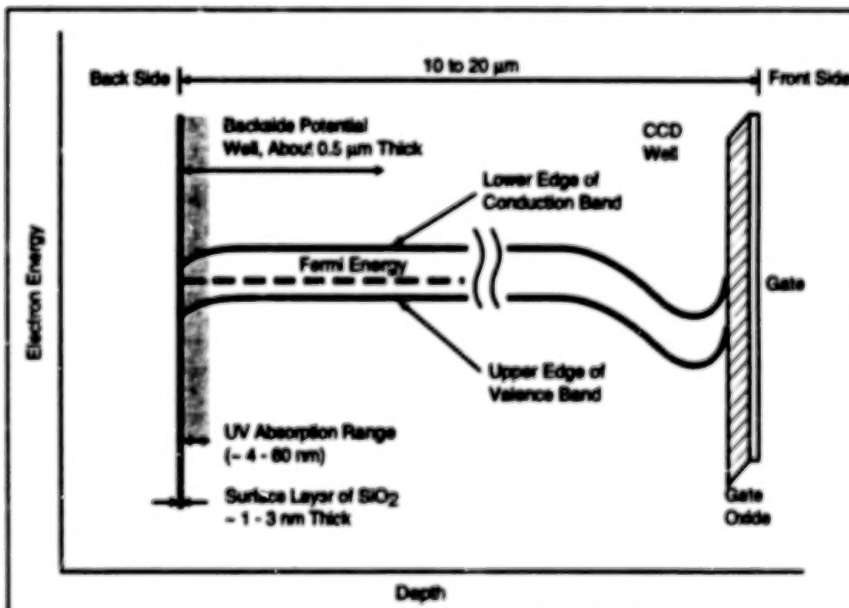
Figure 1. The **Potential Well** on the back side of a non-δ-doped, back-side-illuminated CCD traps charge carriers that are photogenerated near the back side. Because most ultraviolet photons are absorbed near the back side, this effect reduces or eliminates the response of the device to ultraviolet.

Two developments have made it possible to decrease the processing temper-

atures to such an extent that now the required precise δ-doped layer can be

NASA Tech Briefs, March 1995

formed. The first of these developments is a substrate-cleaning process in which an atomically clean silicon surface can be prepared at a temperature as low as 200 °C. The previous substrate-cleaning process for molecular-beam epitaxy required a temperature ≥800 °C.

The second development is a commercial high-temperature Knudsen cell for the evaporation of elemental boron. By use of this cell, one can grow a highly p-doped epitaxial layer of silicon at a temperature <450 °C. Previously, p doping of silicon in molecular-beam epitaxy was obtained by evaporation of compounds like HBO2 and B2O3, and it was necessary to heat the device to a temperature ≥550 °C to prevent incorporation of oxygen into the growing layer of silicon.

An explanation of some of the physical effects that occur in the CCD is prerequisite to an explanation of the improvement afforded by the δ-doped layer. The oxide layer on the back side is nonuniform in thickness, composition, and density of defects, and generally exhibits a substantial fixed positive electric charge. This charge bends the conduction and valence electron-energy bands downward, forming a potential well at the back surface.

The range of absorption depths for ultraviolet photons in silicon is such that photogeneration of electron/hole pairs occurs within 4 to 60 nm of the illuminated (in this case, the back) surface. The potential well at the back surface traps most of these photogenerated charge carriers. The back-surface oxide is full of interface quantum states and localized traps in which most of the charge carriers are annihilated by recombination of electrons and holes. The net result is low quantum efficiency
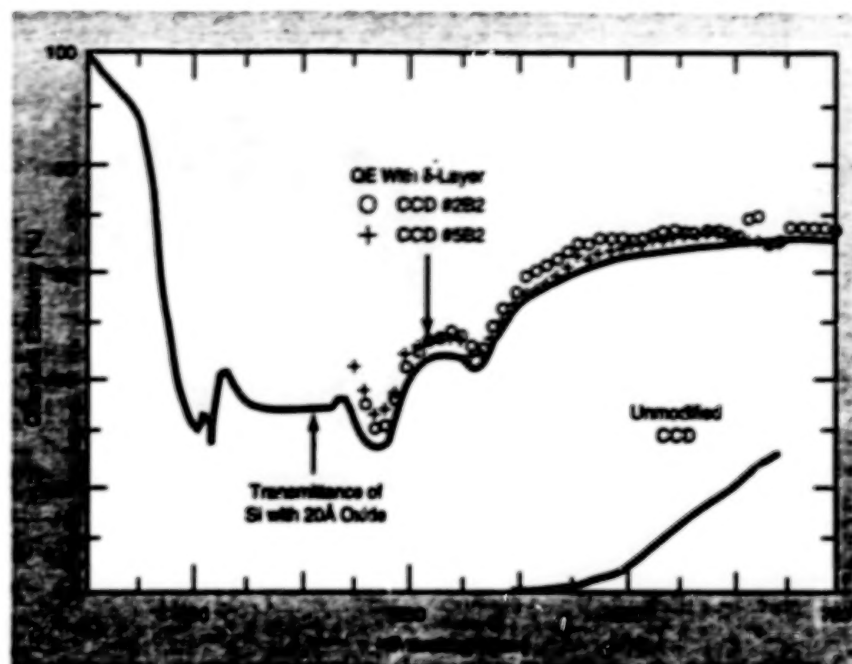
Figure 2. **Measured Quantum Efficiency of Two CCD's** is modified with the growth of a δ-doped silicon layer. The transmittance of silicon, calculated from published optical constants of Si and SiO2, determines the shape of the observed quantum efficiency spectra. For comparison, the quantum efficiency of an unmodified CCD is also shown in the figure.

and low sensitivity of the CCD under ultraviolet illumination.

In principle, a δ-doped layer one atomic layer thick would give rise to a dipole layer of charges less than 0.5 nm wide, nearly eliminating the back-surface potential well. Figure 2 shows the measured quantum efficiency of two δ-doped CCD's. The observed quantum efficiency follows closely the silicon transmittance curve, which accounts for losses due to reflection from the silicon surface and absorption in the oxide. These data indicate that the internal quantum efficiency of a δ-doped CCD is nearly 100% throughout the near UV.

This work was done by Michael E. Hoenk, Paula J. Grunthaner, Frank J.

Electronic Systems

Hardware, Techniques, and Processes

Real-Time Connected-Element Radio-Interferometer System

Receiving stations communicate data and
time signals via optical fibers.

NASA's Jet Propulsion Laboratory,
Pasadena, California

A real-time connected-element radio-
interferometer system incorporates two
receiving stations, separated by a rela-
tively short baseline of only 21 km, that
communicate via fiber-optic data and
timing links. The system, located at
NASA's Deep Space Network tracking
complex at Goldstone, California, pro-
vides accuracies of 50 to 100 nanoradi-
ans for measuring angular positions of
interplanetary spacecraft and extra-
galactic quasars. The overall system
and various components may be adapt-
able to such terrestrial uses as naviga-
tion and the distribution of precise time
and frequency reference signals.

Figure 1 shows the principal functional
blocks of the system. A 100-MHz timing
and frequency reference signal is generat-
ed at station A and transmitted to station
B on one of two fiber-optic communica-
tion links. The radio signals received at
each station are processed via a wide-
band data-acquisition terminal developed
previously for use in very-long-baseline
interferometry. Each data-acquisition ter-
minal performs downconversion, sam-
pling, 1-bit quantization, time-tagging,
and formatting. The output of each data-
acquisition terminal is a 112-Mbit/s bit
stream, which is sent to a real-time corre-
lator at station B; in the case of the bit
stream that originates at station A, the
other fiber-optic link is the medium for
transmission to the correlator at station B.

The real-time correlator performs
cross-correlation of the A and B quan-
tized radio signals in as many as 14 dif-
ferent receiving frequency channels
simultaneously. Bit streams from the 2
sets of 14 channels first enter bit syn-
chronizers, which recover the radio-sig-
nal data and clock components, then
pass to a 28-by-28 crossbar switch,
which can be set by the user to connect
any frequency channel to any correlator
channel. The radio-signal data are then
passed through digital delay lines, which
are driven by 28 separate delay models
sent from an external control computer
to a station processor that is part of the
correlator. The outputs of the delay lines
are fed to both a tone-extractor circuit
board and a cross-correlator circuit
board. On the tone-extractor board,
there is 1 tone extractor for each chan-
nel, but it is time-multiplexed to enable 4
different tones to be extracted from
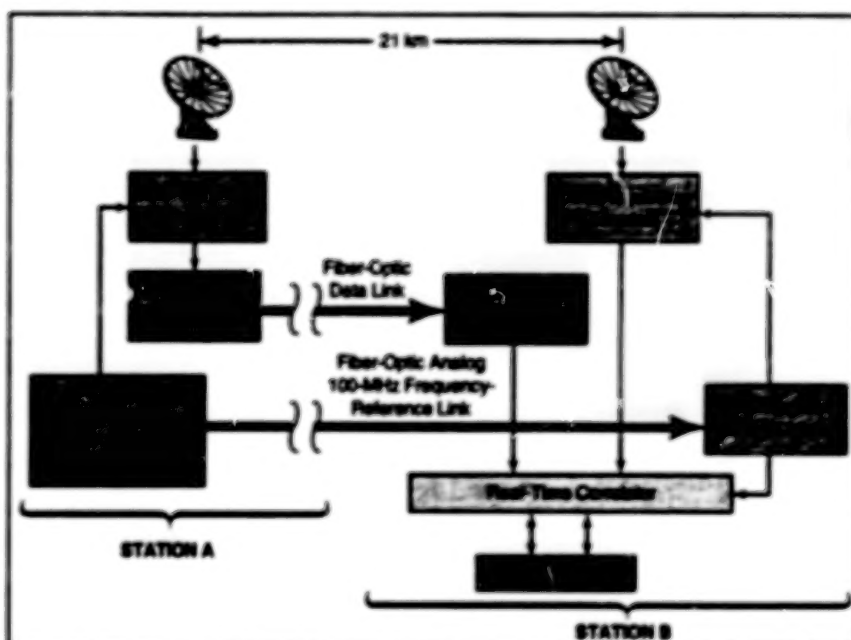
Figure 1. Fiber-Optic Links and a Real-Time Correlator make it possible to compute radio-
interferometric delays in real time. Even though the baseline is much shorter than in very-
long-baseline interferometry, the delay measurement is precise enough to provide acceptable
angular precision.
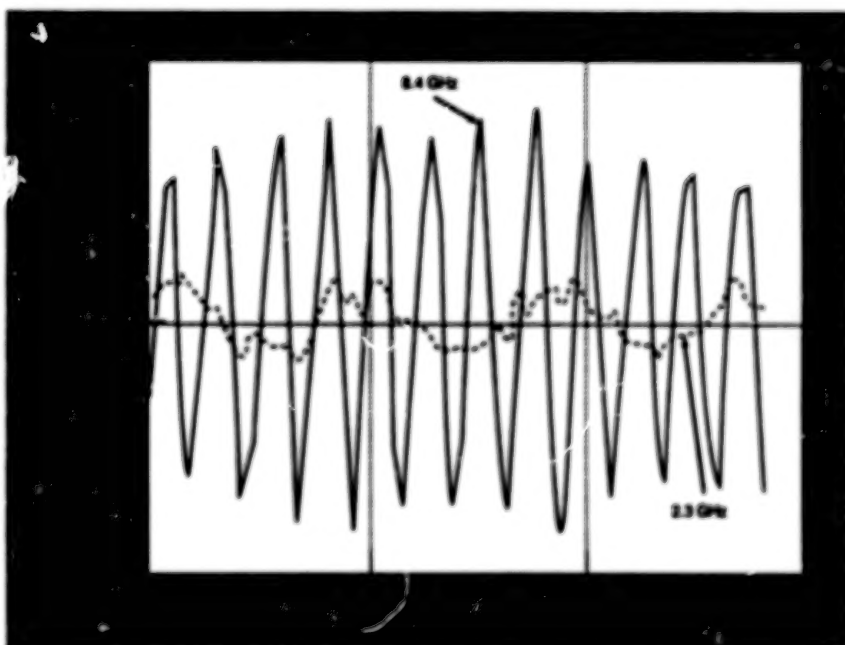
Figure 2. These Correlation Fringes were obtained in an initial test of the system, using 2.3-
and 8.4-GHz signals transmitted by the Magellan spacecraft on June 18, 1991.

each channel, and hence 112 different
phase polynomial tone models are sent
by the control computer to the station
processor.

The connections from the delay lines
to the cross-correlator board are
arranged to correlate the 14 A channels
with the corresponding 14 B channels.

The user can choose to correlate 14
channels with 8 lags each, 7 channels
with 16 lags each, or 1 channel with 112
lags. The 112-lag option would normal-
ly be used for searching clock delay with
a delay range of 28 μs. The cross-corre-
lation board is driven by 14 phase mod-
els and 14 fractional delay models for

each of the 2 receiving stations; these models are also generated by the external control computer and sent to the station processor.

The output of the correlator, displayed in real time on a video terminal, shows the state and quality of the data being received from each station, plots of the correlation fringes for all channels versus time (see Figure 2), plots of the phases of all tones for one channel versus time, and plots of integrated delay and rate-of-change-of-delay patterns for one channel.

Circuit Stops Prelasing in a Q-Switched Laser

Premature emission of laser light triggers a turnoff relay.

Langley Research Center,
Hampton, Virginia
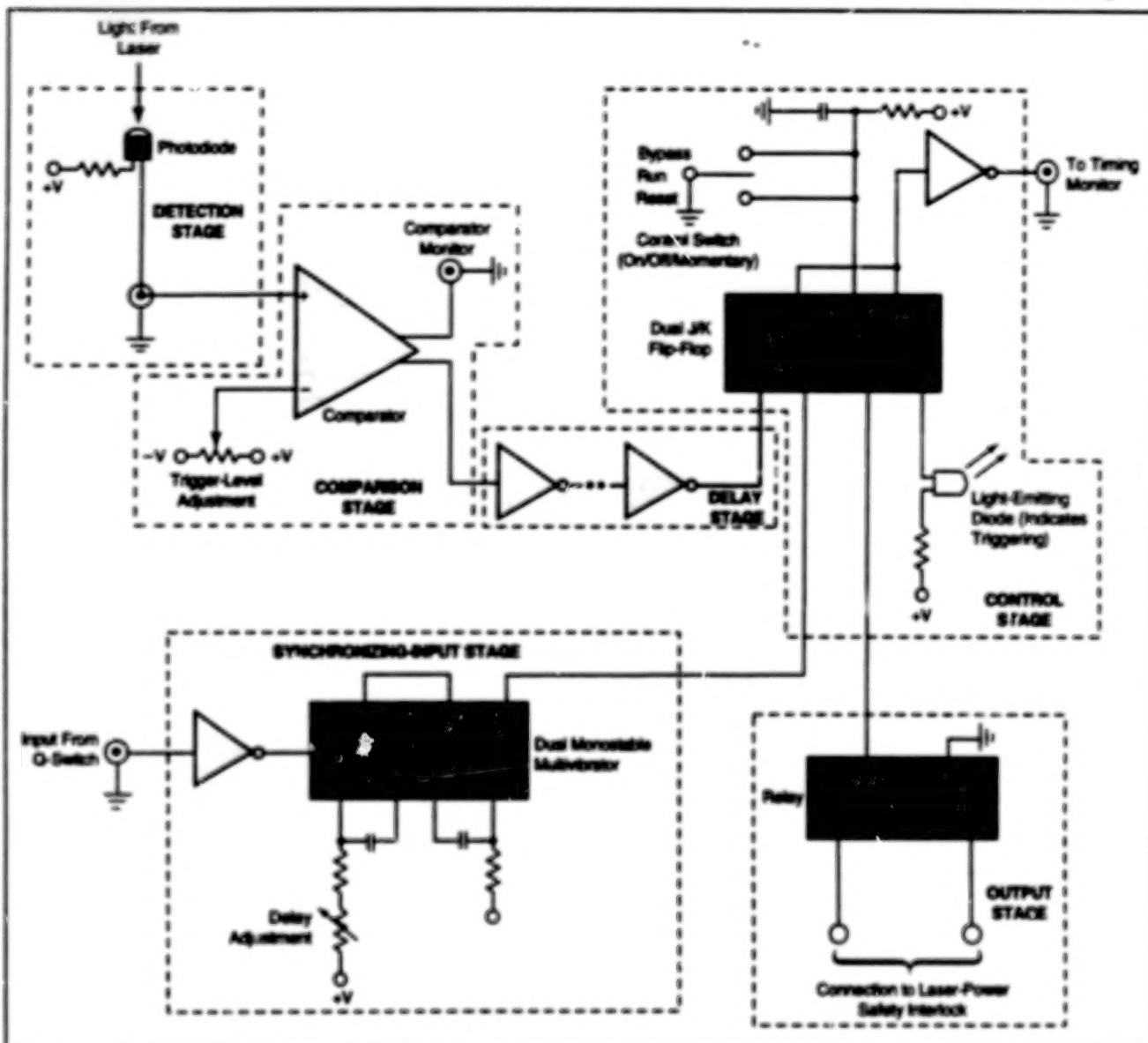
The Protective Shutdown Circuit (shown here in simplified form) turns off the laser power supply when it detects laser light before the end of the Q-switch-trigger pulse.

A protective shutdown circuit stops prelasing in a Q-switched laser that operates at a pulse-repetition rate of about 10 Hz. During normal operation, the Q-switch prevents the emission of light from the laser cavity during the application of the Q-switch-trigger pulse. Sometimes, the Q-switch is unable to hold off emission of laser light during the Q-switch-trigger pulse; "prelasing" is the name of the resulting premature emission. Prelasing is considered undesirable, because it can damage the optical components of the laser and associated equipment, and because it results in uncontrollable variations in the timing and power of the laser output.

The protective shutdown circuit is designed according to the premise that the desired laser output occurs after the Q-switch-trigger pulse, and any laser out-

put that occurs prior to this pulse is considered to be prelasing. When this circuit detects prelasing, it triggers a relay that turns off the laser power supply. The circuit can be integrated into almost any Q-switched-laser system, provided that one can gain access to the laser light, the Q-switch-trigger pulse, and the safety-interlock line of the laser power supply.

The protective shutdown circuit (see figure) consists of six sections — the detection, comparison, delay, synchronizing-input, control, and output stages. A sample of the laser output is band-pass filtered at the designated laser wavelength and fed to a photodiode in the detection stage. The output of the detection stage is fed to the comparator, which issues a logic pulse if the detected laser output exceeds a preset adjustable trigger level. This signal is fed to the delay stage, which consists of a series of inverters; the delay stage imposes a fixed delay that compensates for the difference between other delays, generated elsewhere in the circuit, between the Q-switch-trigger pulse and the photodiode signal. The delayed signal is fed to the "clock" input terminal of the control stage, which is a dual J/K flip-flop with "preset" and "clear" options.

The synchronizing-input stage samples and conditions the Q-switch-trigger pulse and provides an adjustable delay. The output of this stage is fed to the "clear" input terminal of the control stage, which compares the timing of its two inputs. If the delayed signal from the detector stage arrives before the signal from the synchronizing-input stage (representing the detection of laser output before the Q-switch-trigger pulse), then the control stage sends a turnoff signal to the output stage, which is a normally closed relay switch connected to the safety-interlock line of the laser power supply. The turnoff signal opens this switch, causing the power to be turned off.

Compensating for Unbalance in Pulse-Code Phase Modulation

Modulation index or data rate can be decreased, or power can be increased.

NASA's Jet Propulsion Laboratory, Pasadena, California

An algorithm has been proposed for use in a pulse-code phase-modulation transmitter in which non-return-to-zero (NRZ) or biphase data are modulated directly onto a radio-frequency residual carrier signal. The algorithm was devised to compensate somewhat for the effect, upon a distant receiver, of unbalance in the stream of transmitted data. "Unbalance" as used here means inequality between the time-averaged number of transmitted +1s and the time-averaged number of transmitted −1s. Unbalance can give rise to spectral components that can degrade the ability of the receiver to track the phase of the carrier signal, as it must do to read the data stream correctly. Serious degradation can occur when the probability, p, of transmitting a +1 pulse (also called "probability of mark") deviates from 1/2.

The algorithm exploits the discovery that the effects of unbalance in the data can be mitigated to some extent by decreasing the modulation index: within limits, the symbol-error rate decreases with the modulation index. This is because as the modulation index decreases, (1) more power is allocated to the residual carrier (this causes phase jitter to decrease) and (2) less power is allocated to the dc component created by the unbalance (this causes interference with carrier tracking to decrease).

Of course, while a decrease in the modulation index increases the carrier
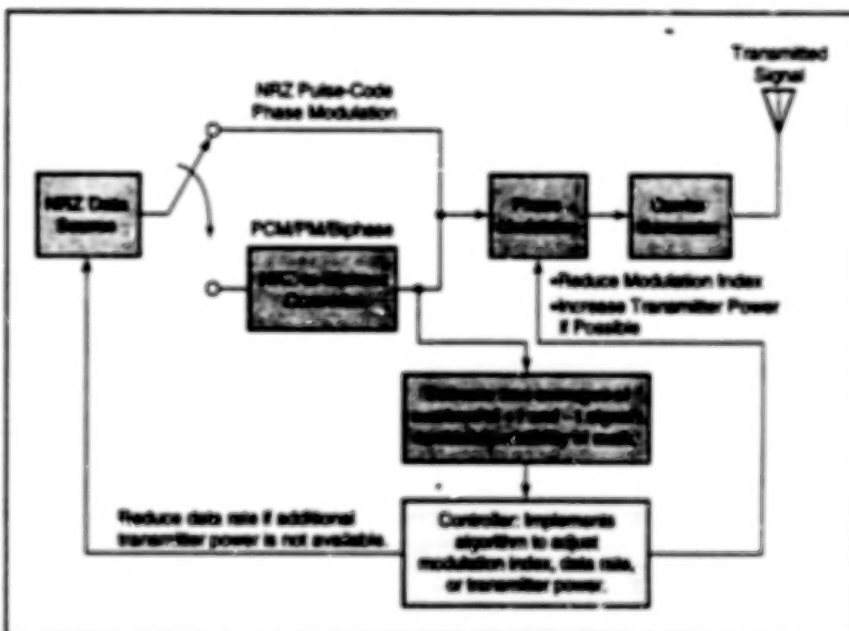
This **Simplified Diagram** of the functional blocks of a transmitter shows the major actions that would be taken by a control unit implementing the algorithm to compensate for unbalance in the data stream.

margin, it decreases the data margin. This consideration places a limit on the improvement achievable solely by reducing the modulation index. The data margin can be increased by decreasing the data rate, and both the data and carrier margins can be increased by increasing the transmitter power. Accordingly, the algorithm is formulated to compute combinations of modulation index, data rate, and transmitter power that compensate

for the measured unbalance in the transmitted data stream (see figure).

The steps of the algorithm can be summarized as follows:

1. Compute the actual carrier and data margins for the communication link for the actual modulation index, m.
2. Compute the threshold modulation index, m_t, for the required data margin and data rate.
3. Compute a modulation index, m_{opt}

that results in a specified amount of degradation of the bit signal-to-noise ratio when $p < 0.45$.

4. If $m_T \leq m_{opt} < m$, then one can reduce m to m_{opt} without taking any other compensatory action.

5. If $m \geq m_T > m_{opt}$, then reducing m to m_{opt} would cause the data margin to

become unacceptably low. The data rate must be decreased and/or the power increased. If additional transmitter power is available, increase the power by an amount computed to maintain the required data margin.

6. If $m > m_T > m_{opt}$ and the transmitter power cannot be increased, then

decrease the data rate by an amount that maintains the required data margin.

This work was done by Tien M. Nguyen and Sami M. Hinedi of Caltech for **NASA's Jet Propulsion Laboratory.** *Further information is contained in a TSP [see page 1].*
NPO-19126

# Computational System for Rapid CFD Analysis in Engineering

A modular, all-electronic system will promote utilization of CFD.

Marshall Space Flight Center, Alabama

A computational system that comprises modular hardware and software subsystems is being developed to accelerate and facilitate the use of techniques of computational fluid dynamics (CFD) in an engineering environment. Although the hardware and software used in CFD are well developed, the utilization of CFD to its full potential has been impeded by the length of time needed to conduct a typical CFD analysis. The total analysis time is long because of the need to preprocess design and flow-geometry data for processing by the CFD software, and to postprocess flow-field data computed by the CFD software into informative displays and summaries. Heretofore, preprocessing and postprocessing hardware and software have been developed separately, without a view toward standardization or integration with each other or with the CFD hardware and software.

The present development addresses the integration of all aspects of the CFD analysis process, including definition of hardware surfaces, generation of computational grids, the CFD flow solution, and postprocessing. The system incorporates interfaces for integration of all the hardware and software tools needed to perform a complete CFD analysis. The system includes tools for efficient definition of flow geometry, generation of computational grids, computation of flows on the grids, and postprocessing of flow data. Multiple options exist within each functional block, and the modularity of the system enables the analyst to select the most appropriate optional tool at each step of the analysis process. To ensure modularity, common data formats are utilized between the major steps in the analysis process. Whenever possible, the common format is based on a national standard to ensure commonality with other CFD systems.

The system accepts geometric input from any of three basic sources: computer-aided design (CAD), computer-
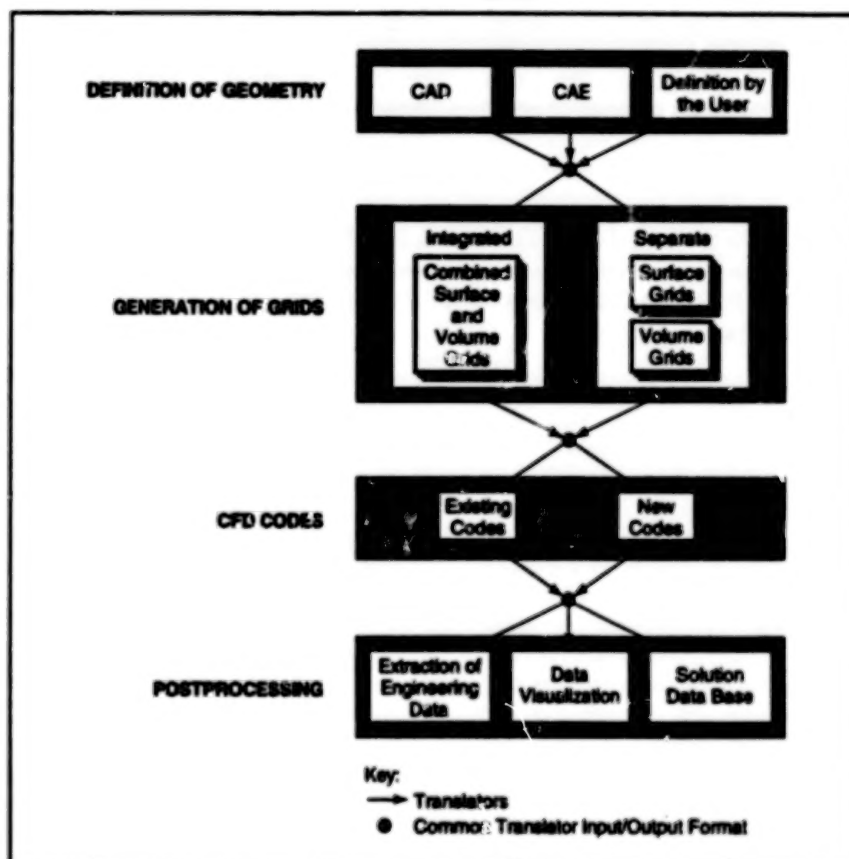
The Relationships Among the Functional Blocks of the system reflect those among the four major steps of the CFD analysis process.

aided engineering (CAE), or definition by the user. CAD and CAE systems typically have native- and standard-format output options. Geometric descriptions defined by the user are typically generated through relatively simple computer codes written by the user, and their outputs can generally be written in any desired format. For acceptance by this system, the definition of geometry must be translated into the Initial Graphics Exchange Standard (IGES) format. The definition of geometry can then be transferred readily to any of the grid-generating subsystems within this system.

The grid generators in this system are divided into two categories, maintaining

the highest level of modularity possible. The first category includes those grid generators that simultaneously generate surface and volume grids. A grid generator in the second category contains separate modules first to generate grids on surfaces, then generate volume grids based on the surface grids. Typically, surface and volume grids are generated sequentially through algebraic techniques, then smoothed with elliptic techniques, as needed.

The system provides for selection of any of several CFD codes that have been developed by various experts and that implement a variety of theoretical and numerical approaches. These codes

have been modified for integration into the system. Any of these codes can read any grid represented in the common format of the system. The outputs of all of these codes are in a common format for postprocessing. The common input and output formats provide a conceptual framework for incorporating new CFD codes.

Postprocessing is needed to reduce the large volume of output information to a form in which it can be readily assimilated and integrated with other products of engineering analysis. As defined within this system, postprocessing encompasses three major functions: extraction of engineering data, visualization of data, and generation of a post-processing data base.

For extraction of engineering data, this system implements a two-step approach to postprocessing intended to maintain a high level of modularity. First, a subroutine is developed and embedded within each CFD code. This subroutine accesses other portions of the code as needed, computes appropriate quantities, and writes them in a common data format.

The Flow Analysis Software Toolkit (FAST) computer program is the first visualization tool to be selected for inclusion in this system. FAST, a product of NASA's Ames Research Center, is a collection of software modules for use in visualizing geometries, grids, and computed flows.

The development of a postprocessing data base is still in an early stage. The large number of data generated in CFD analyses calls for significant effort to develop hardware and software to handle the data. Storage of a complete data base of all final solutions in the common output format would necessitate significant investment in mass-storage devices. Currently, a limited data base of graphical images is being considered. Even so, typical image files can exceed one million bytes each. A possible alternative to storing image files is to maintain a data base of FAST scripts: Given a solution file, one need not store images, but only the script file used to generate the images in FAST. This provides the ability to regenerate previous images quickly, and offers the additional flexibility of being able to modify images within FAST.

This work was done by Steven L. Barson, Edward P. Ascoli, Michelle E. DeCroix, and Munir M. Sindir of Rockwell International Corp. for Marshall Space Flight Center. Further information is contained in a TSP [see page 1].
MFS-29966

Improved Microwave Fiber-Optic Link

Microwave signals can be transmitted long distances with high stability.

NASA's Jet Propulsion Laboratory, Pasadena, California

High-stability transmission of microwave signals along fiber-optic cable has been achieved in experiments by extending previously developed high-stability fiber-optic techniques to microwave frequencies. This system uses an external modulator to amplitude-modulate the intensity of light from a continuous wave (CW) laser at various frequencies from 2 to 12 GHz. The CW laser used in the experiments comprised a neodymium:yttrium aluminum garnet (Nd:YAG) laser pumped by a semiconductor laser diode. The external modulator was a lithium niobate traveling-wave electro-optical Mach-Zehnder interferometer. The phase noise of this system is -110 dBc in a 1 Hz bandwidth, 1 Hz from an 8.4 GHz carrier. The modulated optical signal was transmitted over a 29-km fiber-optic cable connecting two Deep Space Stations in the NASA/JPL Goldstone Deep Space Communications Complex (DSCC). The signal-to-noise ratio of the signal after transmission was > 100 dB·Hz and the Alan deviation was 1×10^{-15} for 1,000 seconds averaging time.

The high power output and narrow linewidth of the Nd:YAG laser and external modulator combination enable higher stability and higher dynamic range fiber-optic transmission of microwave signals over longer distances than is achievable with directly modulated semiconductor-laser based systems. This system is a proto-
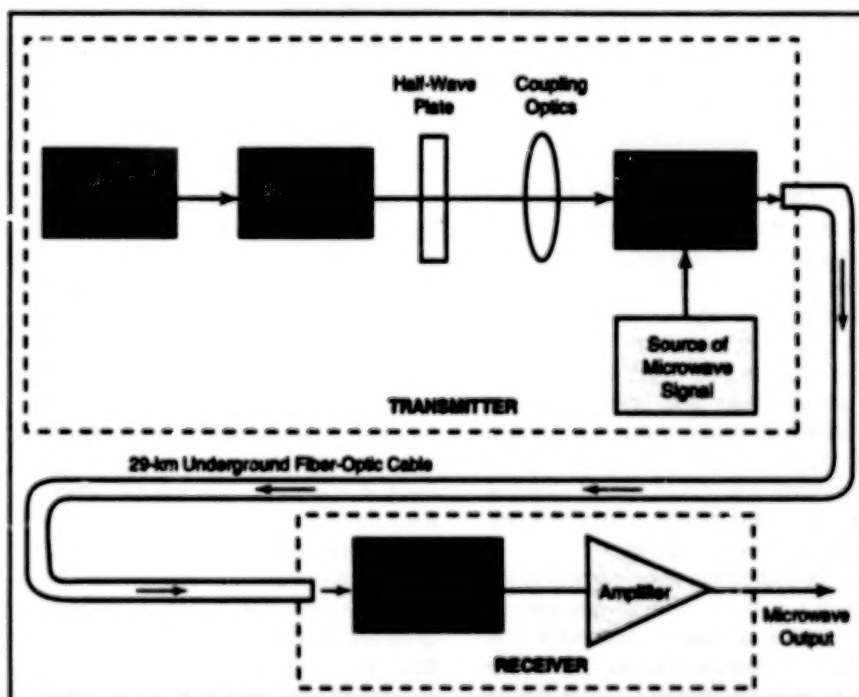
Light From the Nd:YAG Laser is amplitude-modulated with a microwave signal. The modulated light is used to send the microwave signals over the 29-km fiber-optic cable.

type to test the concept of high fidelity transmission of received microwave signals over fiber-optic cables, without the need to downconvert the microwave signals for transmission as is done now in a DSCC. This type of fiber-optic system should also prove useful in distribution of future, more stable, frequency reference signals, phased array radar systems, and aircraft landing systems using bistatic radar.

This work was done by Ronald T. Logan and George F. Lutes of Caltech for NASA's Jet Propulsion Laboratory. Further information is contained in a TSP [see page 1].
NPO-19007

Optoelectronic Instruments for Analysis of Surface Defects

Structured-light microscopes are combined with modern data-acquisition and -processing circuits.

John F. Kennedy Space Center, Florida

A family of portable optoelectronic instruments is being developed to facilitate the inspection of surface flaws like gouges, scratches, raised metal, and dents on large metal workpieces that are subject to surface-finish requirements. Previously, impressions of flaws were taken in a polymeric material, and the hardened polymeric samples were carried to a laboratory, where they were sectioned and examined under an optical comparator to determine dimensions of the flaws: this process was labor-intensive and took hours for each flaw. The present optoelectronic instrument is brought to the workpiece and semiautomatically makes an electronic record of the three-dimensional shape of a flaw. With this instrument, the entire inspection process takes only minutes.

The prototype instrument includes a structured-light microscope, which represents a variation of a concept that has been the basis of a number of optical inspection instruments since the year 1932. The basic concept involves the projection of a known pattern of light [one or more line(s) and/or dot(s)] onto the surface to be inspected. The topography of the surface is then determined from the distortion of the pattern as viewed through the instrument, by use of the known proportionality between the distortion of the pattern at a given point and the deviation in the depth of the surface at that point. In this case, the pattern (laser line) is created by a miniature projector located in an optical head that is placed upon the workpiece at the location of the defect. The optical head also contains the microscope that is used to view the pattern.

The output of the video camera is fed through a cable to a frame-grabber circuit board in a desktop computer. The computer software enables the technician to view the image (whether live or frozen) at high resolution on the cath-
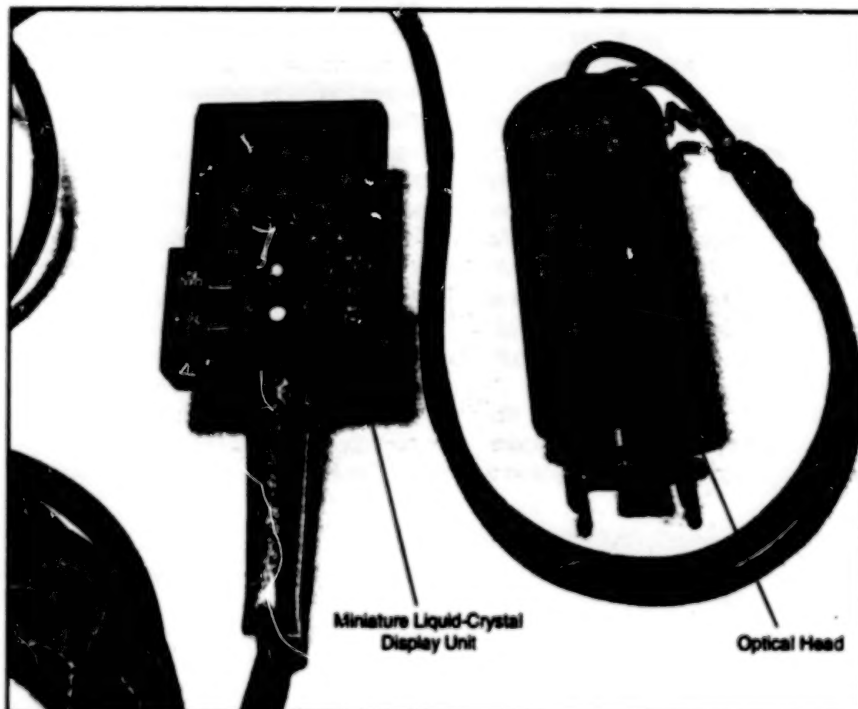
The **Optical Head** contains a structured-light microscope equipped with a miniature video camera. The liquid-crystal display unit provides a low-resolution image that assists in positioning the optical head over a surface flaw.

ode-ray-tube display unit of the computer, or at low resolution on a liquid-crystal display unit, which is mounted on top of the optical head (see figure). The low-resolution image helps the technician to find the defect and center it in the field of view when positioning the optical head on the workpiece.

The computer software provides cursors that the technician can move about in the image for measuring surface flaws. (For this purpose, the instrument must first have been calibrated against known standards.) After an image has been captured and the cursors set, the computer generates a report in the form of an annotated graphical image of the flaw. The image can be printed by use of a miniature high-resolution ink-jet printer and/or stored on a floppy disk.

The prototype instrument has a measurement range of about 0.001 to 0.020 in. (about 25 µm to 0.51 mm) in width and depth, with a resolution of about 0.0002 in. (about 5 µm) and an accuracy of about 0.0005 in. (about 12 µm). However, the range of measurement can be readily changed simply by changing the optics to increase or decrease the magnification.

Optoelectronic Alignment and Ultrasonic Ranging Apparatus

A beam of light guides alignment, then range is measured by use of ultrasound.

John F. Kennedy Space Center, Florida

An optoelectronic/ultrasonic apparatus facilitates the three-dimensional alignment of a spot on one object with respect to a facing (but not touching)

spot on another nearby object. The apparatus was designed to help in positioning the external tank of the space shuttle between the two solid rocket

boosters, and should be useful in other applications in which one seeks to align large components that are to be locked together in assemblies.

The apparatus includes a sensor head mounted on one of the two objects that are to be aligned with each other. The head contains a bright red light-emitting diode with a focusing lens that projects a spot of light about 3/4 in. (about 19 mm) wide at a distance of about 1 ft (about 30 cm). The light is turned on and off at a rate of 1 Hz to increase its visibility. Alignment in the plane perpendicular to the beam is achieved by moving the objects relative to each other until an alignment mark on the other object becomes centered in the beam.

The sensor head also contains an ultrasonic range sensor that measures the distance between the two objects by the well-known pulse/echo-delay technique. This ultrasonic technique was chosen over optical and microwave techniques because of its lower cost, lower risk, and suitability for rapid development. The ultrasonic sensor used in the prototype of the apparatus is a commercial unit that consists of ultrasonic transducers connected via a cable to a microprocessor-controlled measurement circuit that produces the distance information.

An added microprocessor is used to convert the raw distance to the desired units (inches in the original application), subtract out the length of protrusion of the transducer, and compensate for variations in the speed of sound with changes in temperature of the air. The added microprocessor can also compute the distance through which a crane must move to position one of the objects (the external tank).

The added microprocessor drives a 16 × 4-character liquid-crystal display, indicating distances measured by two sensor heads, temperature, and remaining battery life. Processing and display are powered by a 12-V nickel/cadmium battery. The apparatus measures distances with a resolution of 1/16 in. (about 1.6 mm).

This work was done by J. David Collins and Jorge Rivera of Kennedy Space Center and Robert Youngquist, J. Steven Moerk, William Haskell, Robert Cox, and Kenneth Rose of I-NET. Further information is contained in a TSP [see page 1].
KSC-11654

Holographic Helmet-Mounted Display Unit

This unit would be used to develop innovative concepts for display of information to pilots.

Langley Research Center, Hampton, Virginia

The helmet-mounted display unit shown in the figure has been designed for use in testing innovative concepts for the display of information to aircraft pilots. It weighs about 4.8 lb (about 2.3 kg), but its weight is distributed so that the wearer senses no imbalance. It operates in conjunction with computers that generate graphical displays. A magnetic sensory device tracks the orientation of the unit to provide data for variation of displays with the change in orientation of the wearer's head.

The display unit includes two ocular subunits containing miniature cathode-ray tubes and optics that provide a 40° vertical, 50° horizontal field of view to each eye, with or without stereopsis. Each ocular subunit is adjustable to vary the overall horizontal field of view from 50° to 100°, with corresponding variation in the stereoscopic overlap region. The optical components are fully color-corrected, though the miniature cathode-ray tubes are monochrome; this provides for upgrading to color as color display technology matures.

The Helmet-Mounted Display Unit would offer the flexibility to operate in a variety of modes for investigation of human and technological factors in the display of information to pilots.

In a future color application, each ocular subunit would include a trichromatic holographic combiner tuned to the red, green, and blue wavelengths of the phosphors most likely to be used in the development of miniature color display devices.

This work was done by James R. Burley II of Langley Research Center and Joseph A. LaRussa of Technology Innovation Group. Further information is contained in a TSP [see page 1].
LAR-14603
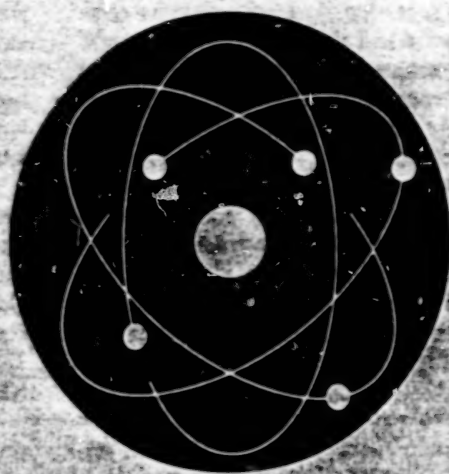
Physical Sciences

Hardware, Techniques, and Processes

Books and Reports

Liquid-Feed Methanol Fuel Cell With Membrane Electrolyte

Advantages include relative simplicity and elimination of corrosive electrolytic solutions.

NASA's Jet Propulsion Laboratory, Pasadena, California

The figure illustrates a fuel cell that generates electricity from a direct liquid feed stream of methanol/water solution circulated in contact with an anode, plus a direct gaseous feed stream of air or oxygen in contact with a cathode. This cell offers an advantage of simplicity over some prior methanol fuel cells in which the methanol must be vaporized and humidified to form gaseous fuel feed streams. Unlike other prior liquid-feed methanol fuel cells, this one does not contain a corrosive acid or alkaline electrolyte solution, which is hazardous and can react with other cell materials to form contaminants that degrade performance. The operation of this cell does not involve the complex water- and thermal-management systems of prior cells. Overall, this fuel cell offers the potential for reductions in the size, weight, and complexity, and for increases in safety of fuel-cell systems.

The electrolyte in this cell is a perfluorinated polymeric membrane than can be maintained conductive by contact with the methanol/water solution. The membrane serves as both a proton-exchange medium and a barrier that resists diffusion of methanol to the cathode. The membrane also acts as a separator between the anode and cathode. The use of such a membrane electrolyte instead of liquid electrolytes mitigates the problem of parasitic shunt currents in a fuel cell stack. Unlike corrosive liquid electrolytes, the solid electrolyte membrane does not form contaminants that can degrade operation.

The membrane electrolyte and the electrodes are formed into a unit by hot-pressing them together. The anode contains a platinum/ruthenium alloy that acts as a catalyst for the anode half-cell reaction (electro-oxidation of methanol). The anode is structured to permit the methanol, water, carbon dioxide, and hydrogen ions to diffuse through it. The cathode contains platinum, which acts as a catalyst for the cathode half-cell reaction (electroreduction of oxygen). The cathode is also structured to permit gases to diffuse through it. Carbon dioxide generated in the anode half-cell reaction diffuses out of the anode and forms bubbles that escape by rising
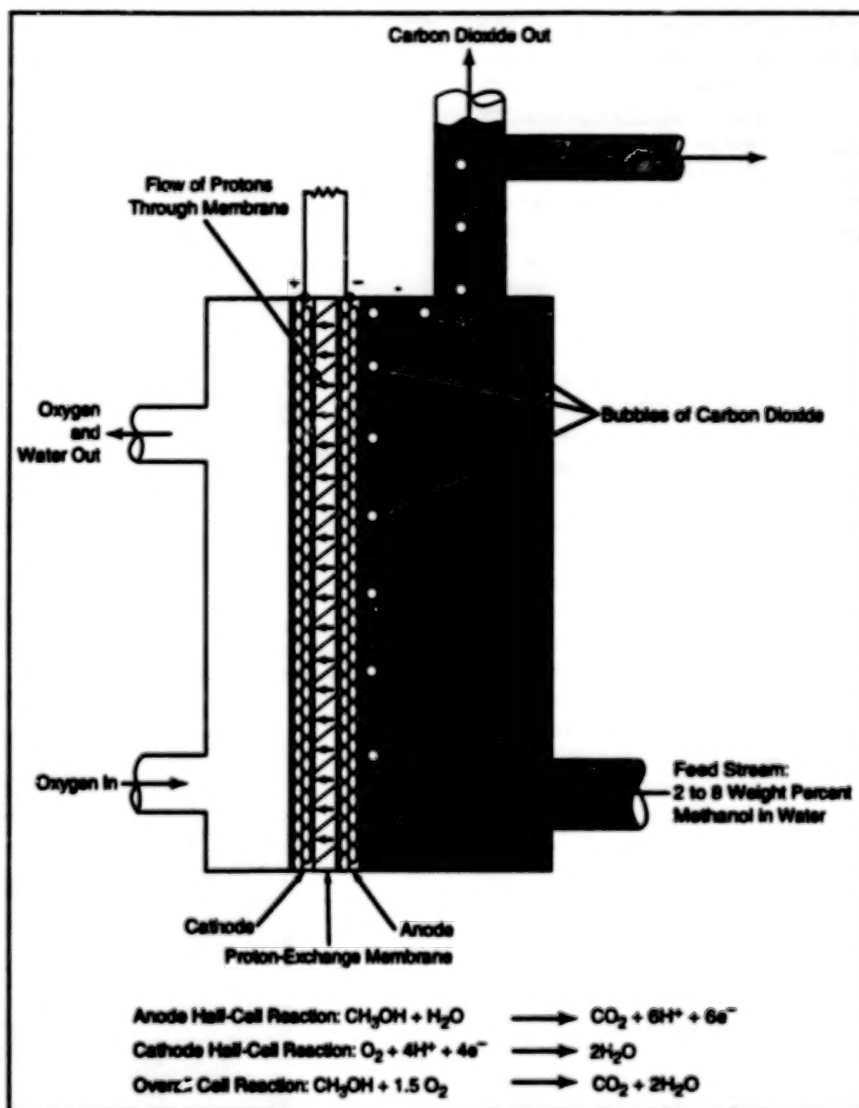
This Fuel Cell is fed directly by streams of methanol/water solution and air (or oxygen). A laboratory version of this cell delivered a potential of 0.53 V at a current density of 100 mA/cm^2 and 0.48 V at 300 mA/cm^2. These voltage and current levels are higher than those of prior direct-oxidation methanol fuel cells and are high enough to warrant consideration for practical applications.

through the methanol/water feed stream. Thus, disposal of the carbon dioxide does not present a problem.

This work was done by Subbarao Surampudi, S. R. Narayanan, Gerald Halpert, Harvey Frank, and Eugene Vamos of Caltech for NASA's Jet Propulsion Laboratory. Further information is contained in a TSP [see page 1].

*In accordance with Public Law 96-517, the contractor has elected to retain title to this invention. Inquiries concern-*ing rights for its commercial use should be addressed to

William T. Callaghan, Manager
Technology Commercialization
JPL-301-350
4800 Oak Grove Drive
Pasadena, CA 91109
Refer to NPO-19046, volume and number of this NASA Tech Briefs issue, and the page number.

Flow Splitter for Measuring Large Leaks

The range of a sensitive leak detector is extended.

Lyndon B. Johnson Space Center, Houston, Texas

A flow splitter increases the size of a leak that can be measured by a helium mass-spectrometer leak detector. Ordinarily, such a leak detector can measure leakage of helium at rates no greater than 1×10^{-5} standard cm^3/s. The flow splitter multiplies the maximum measurable rate of leakage by a factor of 1,000.

The flow splitter is a manifold that can be adjusted to send only a small portion of the flow — typically 0.1 percent — to the leak detector. The manifold (see figure) contains three valves and a thermocouple vacuum transducer. It includes compression O-ring fittings that provide for quick attachment to the source of the leak, the leak detector, and a large-capacity mechanical vacuum pump.

The setup is calibrated prior to measurement of a leak. First, a multirate calibrated leak source is connected to the manifold in place of the source that contains the leak to be measured. A technician adjusts the valves to make the desired fraction of total flow register on the leak detector. Then by use of all the calibrated rates of the calibrated leak source, the technician creates a calibration error curve. Typically, the curve is nearly linear. A leak of unknown size within the range of this curve can be quantified.

Maintaining the same valve settings, the technician then replaces the calibrated source with the true source that contains the leak to be measured. The rate of leakage is determined by relating the leak-detector reading to the calibration curve. The vacuum transducer monitors manifold pressure.

This work was done by William S. Hyatt of Ball Corp. for Johnson Space Center. No further documentation is available.
MSC-22042
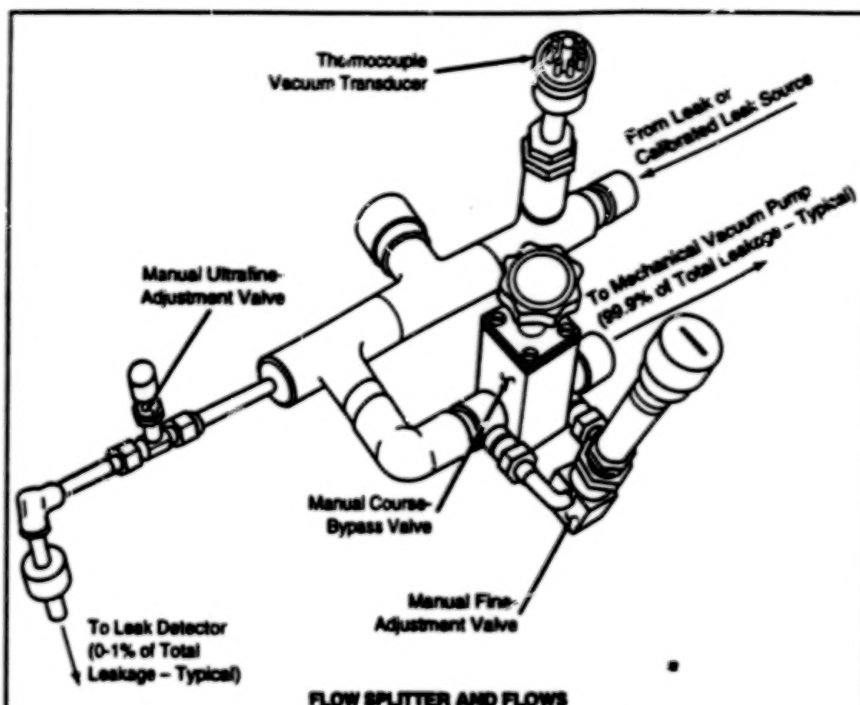
FLOW SPLITTER AND FLOWS

FLOW SPLITTER AND CALIBRATED LEAK SOURCE

Leaking Gas Flows into the manifold, where a small fraction of the flow is diverted to a leak detector. The bulk of the flow — typically 99.9 percent — is removed by the mechanical vacuum pump.

Improved Linear-Ion-Trap Frequency Standard

Some previous design constraints could be relaxed.

NASA's Jet Propulsion Laboratory, Pasadena, California

An improved design concept for a linear-ion-trap (LIT) frequency-standard apparatus has been proposed. The improved design is intended to increase the long-term frequency stability of the apparatus while reducing its size, mass, and cost.

To explain the improved design, it is necessary to first explain the basic principle of operation. A linear-ion-trap frequency standard of the type now in use (see Figure 1) includes a four-bar linear ion trap in a precisely defined magnetic field shielded from disturbance by the ambient magnetic field. Mercury ions are created in the trap by a pulse of electrons onto a weak vapor of neutral mercury atoms. The basic opera-

tion of this and other atomic frequency standards is a comparison between (1) a stable reference frequency of the trapped ions acting as an atomic oscillator and (2) the frequency, multiplied by a known integer, of a local or "flywheel" oscillator that one seeks to standardize by making it resonate with the atomic oscillator.

The ions must be prepared for this comparison in a way that creates a difference between the populations of ions in the hyperfine levels of the ground state. This preparation is effected by optical pumping with ultraviolet light from a laser or a discharge lamp. After preparation, the laser or lamp is turned off and the ions are irradiated by a microwave pulse at the multiplied local-oscillator frequency. After the microwave pulse, the laser or lamp is turned on again and the intensity of fluorescent light emitted by the ions is measured to determine whether the microwave radiation has changed the population of the hyperfine levels: Any deviation of the multiplied frequency of the local oscillator from the reference atomic frequency changes the intensity of the fluorescent light measured when the laser or lamp is turned on. These changes are converted to a voltage that is fed back to the frequency-control port of the local oscillator to keep it tuned to the reference atomic frequency.

The physical basis for the improved design lies in the observation that ions can be moved along the axis of the trap by use of applied dc voltages. This makes it possible to separate the state-preparation-/fluorescence-interrogation region from the more critical microwave-resonance region. The separation would make it feasible to relax some of the constraints on the designs of present units. For example, the microwave-resonance region could be designed with no consideration of optical issues. A simple set of cylindrical shields and solenoid could supply a very nearly uniform and stable magnetic environment; in the proposed configuration shown in Figure 2, the volume of the microwave-resonance region would be about a hundredth of that of present units because the diameter of the magnetic shields would be about a tenth that of present units. Inasmuch as the temperature of the apparatus must be regulated and the temperature of the microwave-resonance region must be regulated most strictly, the reduction in size could simplify the problem of thermal control.

Similarly, the optical state-preparation/interrogation region could be designed without concern for magnetic fields that could perturb the microwave/atomic resonance. In practice, this means that the optical components would no longer be required to be nonmagnetic as in the previous design and that as a consequence, cheaper and smaller optical components and associated hardware could be used. Relaxation of the requirement of nonmagnetism in this region would also simplify the design

of the electron gun and its power supply because of reduction in concern about suppressing stray magnetic fields generated by filament supply currents.

Finally, the largest shift in frequency and the potential instability could be reduced greatly by selecting a somewhat greater trapping length in the resonance region. The shift in frequency stems from the nonzero diameter of the ion cloud: ions spend time in regions of large radio-frequency trapping fields, where their motions result in frequency pulling via the second-order Doppler or relativistic time-dilatation effect. The magnitude of this shift is proportional to the linear ion density; that is, the number of ions per unit length. An increase in the resonance trapping length to about 200 mm would reduce, to about a fourth of the present value, the sensitivity of the apparatus to variations in the number of ions.

This work was done by John D. Prestage of Caltech for NASA's Jet Propulsion Laboratory. Further information is contained in a TSP [see page 1].

This invention is owned by NASA, and a patent application has been filed. Inquiries concerning nonexclusive or exclusive license for its commercial development should be addressed to the Patent Counsel, NASA Resident Office–JPL [see page 1]. Refer to NPO-19081.
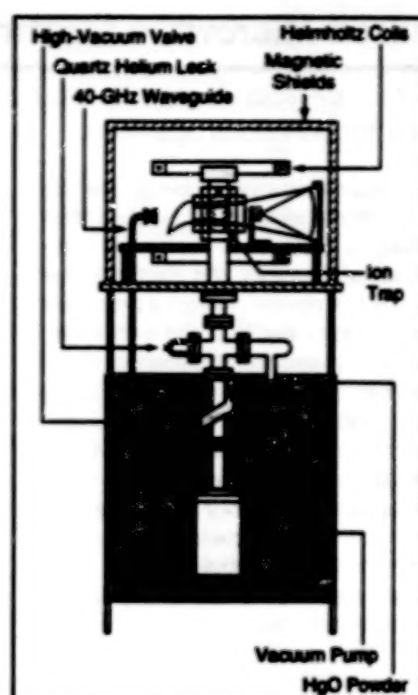
Figure 1. In the Present Frequency-Standard Apparatus, ^{199}Hg$^+$ ions are prepared in the appropriate quantum-state populations, exposed to microwaves from a local oscillator, and interrogated optically for deviation of the microwaves from resonance with a hyperfine transition of the ions. All processing of ions takes place in the same volume in a linear ion trap in an applied magnetic field in a magnetically shielded housing. The apparatus is about 2 m high by 1 m on a side.
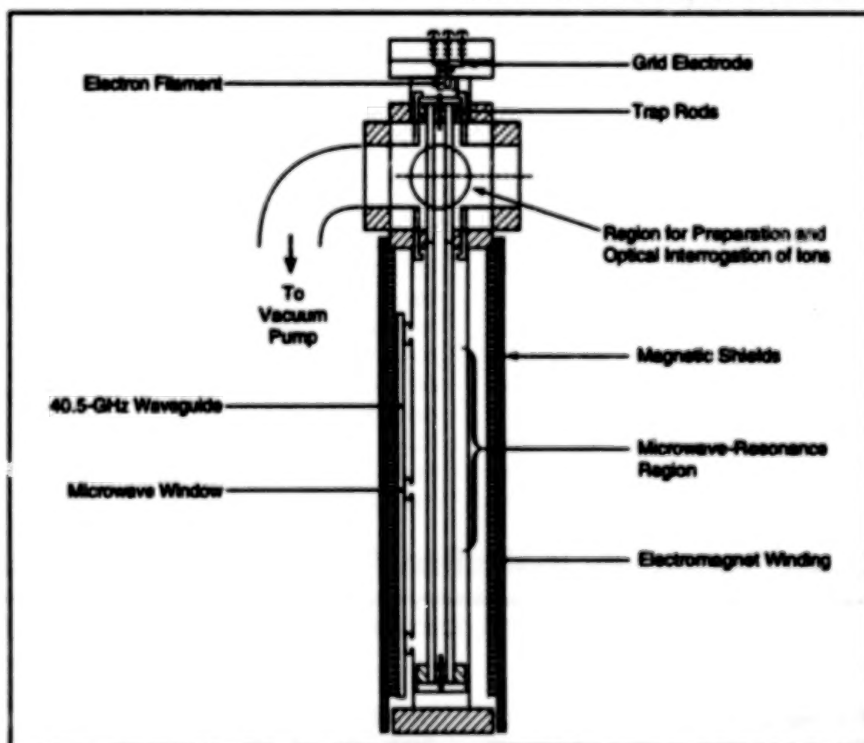
Figure 2. The Proposed Frequency-Standard Apparatus would contain a lengthened linear ion trap, and ions would be processed alternately in two regions: the ions would be prepared in the upper region of the trap, then transported to the lower region for exposure to the microwave radiation, then returned to the upper region for optical interrogation. The overall dimensions of the apparatus would be about 10 by 50 cm.

Pulsed-Microwave Electrothermal Thrustors

Pulsed operation is expected to suppress instabilities seen in continuous operation.

Pulsed-microwave electrothermal thrustors are being investigated as alternatives to continuous-microwave electrothermal thrustors. (An electrothermal thrustor is a device in which a propellant gas is heated electrically in a chamber, causing it to expand and flow out of the chamber through a nozzle to create thrust.) Although the pulsed-microwave electrothermal thrustors were originally intended for use in spacecraft propulsion systems, they may also prove useful on Earth in some material-processing and manufacturing applications.

The design of a microwave-heated electrothermal thrustor involves, among other things, a choice of microwave frequency and dimensions of the chamber (regarded as a waveguide or resonant cavity) to support a specified electromagnetic mode in which the microwave electrical field is concentrated in a region away from the walls. The microwave power supplied to the chamber must be sufficient to initiate and sustain an electric discharge in the propellant gas in this region. Cold propellant gas that flows across the discharge plasma is heated by a combination of conduction, diffusion, radiation, and convection. Placement of the discharge away from the walls reduces the loss of heat and erosion of the walls.

In experiments in which microwave power was supplied to the chambers continuously, the discharges exhibited instability in that they tended to move toward the microwave power sources. This phenomenon gave rise to the present concept of using pulsed instead of continuous microwave power: after each short heating pulse, the discharge is extinguished and thereby pr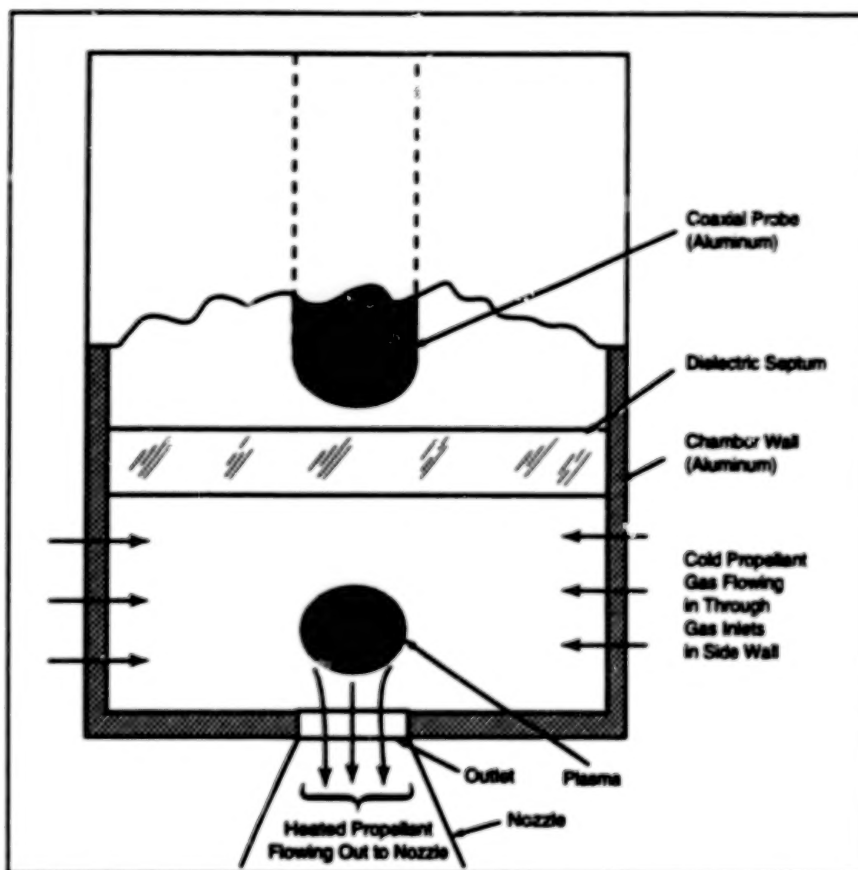evented from moving a significant distance toward the microwave power source. Any ionized gas remaining upstream after the pulse would be swept back downstream, into

Pulsed Microwave Power, delivered via the coaxial probe, would be focused in a region near the outlet, where it would heat the propellant gas and form a plasma. Pulsing would suppress the tendency of the plasma to move upstream toward the probe.

and through the discharge region, by the flow of cold propellant gas.

The figure illustrates part of a conceptual cylindrical pulsed-microwave electrothermal heater similar to one that is being used in experiments to test the feasibility of the concept. Microwave power would be supplied to the chamber by a coaxial probe. The probe and cavity would be designed to support the TM_{011} mode, which features two maximums of the electromagnetic field on the cylindrical axis: one in the vicinity of

the probe and one at the lower end of the chamber, just above the outlet to the nozzle. By use of a dielectric (e.g., quartz) septum, the propellant gas could be kept away from the probe, thus allowing the discharge to occur only at the desired position near the outlet.

This work was done by Juergen Mueller and Joel C. Sercel of Caltech for **NASA's Jet Propulsion Laboratory.** *Further information is contained in a TSP [see page 1].*
NPO-18766

Higher-Sensitivity Ionization Trace-Species Detector

The electron source and electron optics are modified to increase output.

The electron source and electron optics of a reversal electron-attachment detector have been modified to increase its sensitivity. The original version of this apparatus was described in "High-Sensitivity Ionization Trace-Species

Detector" (NPO-17596), *NASA Tech Briefs*, Vol. 14, No. 2 (February 1990) page 38. The apparatus is used to detect molecules of a particular chemical species of interest (e.g., narcotics, explosives, or organic wastes) that may be

present in the air at low concentrations, and which are known to attach extremely low-energy electrons. The apparatus does this by ionizing molecules from the sampled atmosphere, then detecting the ions of the species of interest.

Like the original version of the apparatus, the modified reversal electron-attachment detector (see figure) includes a cathode at electrostatic potential V_1 that is heated to emit electrons, plus a number of other electrodes at various electrostatic potentials. Together, these other electrodes act as an electron-optical system that extracts electrons from the cathode, then accelerates and focuses the electrons into an electrostatic mirror, wherein the electrons are decelerated to zero longitudinal velocity and nearly zero radial velocity at reversal plane R. A small sample of the atmosphere to be tested is injected into the vacuum of the apparatus at R. The kinetic energy of the electrons at R is low enough that some electrons become attached to the molecules of interest, forming either parent negative ions, and/or fragment ions through dissociative attachment.

The voltages V_5, V_6, and V_7 on the electrodes of the electrostatic mirror are square-wave modulated by electronic switches S1, S2, and S3 in such a way that during the first half of the modulation cycle, the electron beam is brought to R to ionize the molecules in a field-free region, then during the second half of the cycle, the negative ions are extracted. The extracted ions are deflected by a 90° electrostatic analyzer (which helps to ensure that only negative ions pass through) and focused into a quadrupole mass spectrometer. The ion signal of the mass spectrometer is produced by a channel electron multiplier, amplified, and fed to a pulse counter and a multichannel analyzer.

The electron emitter in the original version of the apparatus was planar. The emitter in the modified apparatus is an indirectly heated spherical cathode, which has a larger emission area and therefore emits a larger electron current than did the planar cathode. Because of
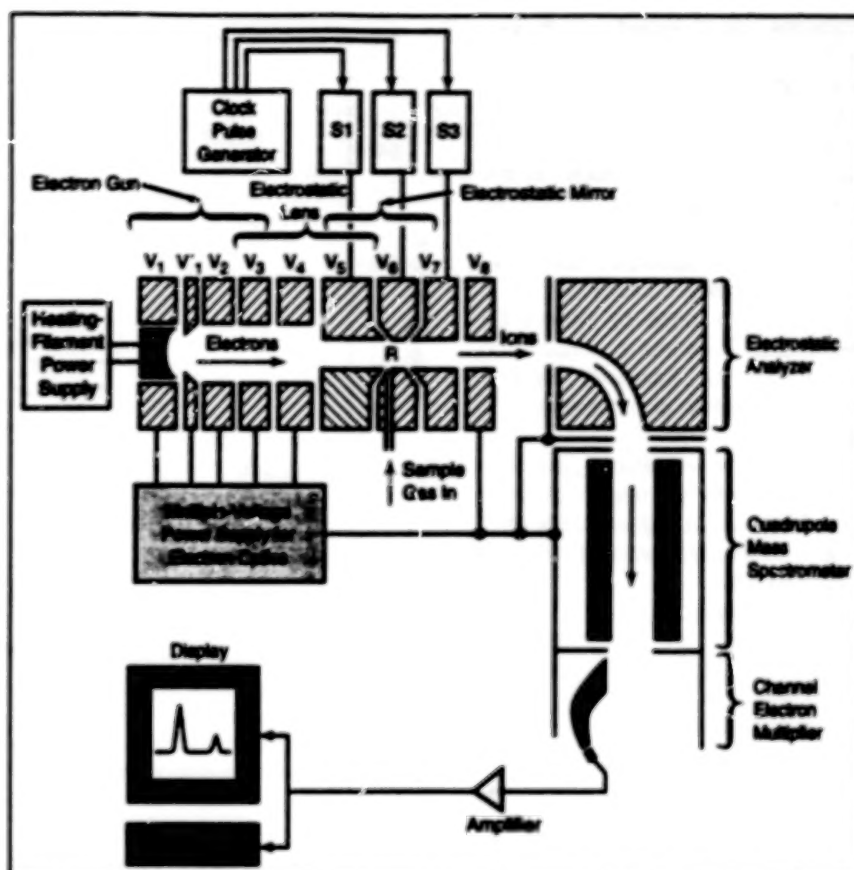
The Modified Reversal Electron-Attachment Detector features an indirectly heated spherical cathode and redesigned electron optics that, together, deliver more electrons at low kinetic energy to the reversal plane, R. The greater electron current generates more ions for detection.

the larger current, the electrode system had to be redesigned: this was done with the help of a computer program written specifically to analyze electrostatic fields and trajectories of electrons in those fields, including the effects of space charge. The apparatus was tested to determine its sensitivity in the detection of small amounts of known molecules carried in nitrogen gas. For example, in the case of 10 parts per trillion of carbon tetrachloride in nitrogen, the modified apparatus put out a signal about 25 times that of the original version.

A Real-Time Nonvolatile Residue (NVR) Monitor

Preliminary measurements confirm expectations.

John F. Kennedy Space Center, Florida

This work is a new development and application of the device described in "Surface-Acoustic-Wave Piezoelectric Microbalance," NASA Tech Briefs, Vol. 17, No. 4 (April, 1993), page 42. The active sensing element of the Real-Time NVR Monitor comprises a pair of piezoelectric surface-acoustic-wave resonators that resonate at a frequency of 200 MHz. A bare, uncoated resonator is exposed to the atmosphere and directly in contact with airborne volatile and nonvolatile materials that leave residues on its surface. The resonant frequency of the exposed resonator decreases with increasing mass of adsorbed residue; the resulting beat frequency between the two resonators increases with the mass and thus serves as a sensitive real-time indication of airborne contaminants or nonvolatile residue. A two-week test of a prototype instrument inside a Kennedy Space Center clean room confirmed that the device performed well and according to design calculations. A gradual increase in the beat-frequency shift with superimposed

fluctuations was observed (see figure). The gradual monotonic increase in signal was attributed to the accumulation of background nonvolatile residues, whereas the fluctuations were attributed to a combination of (1) variations in the levels of both volatile and nonvolatile contaminants correlated with daily work schedules, and (2) adsorption and desorption of the volatile contaminants.

*This work was done by William D. Bowers and Raymond L. Chuan of Femtometrics for **Kennedy Space Center**. No further documentation is available.*

In accordance with Public Law 96-517, the contractor has elected to retain title to this invention. Inquiries concerning rights for its commercial use should be addressed to

Dr. W. D. Bowers
Femtometrics
1001 W. 17th St. Suite R
Costa Mesa, CA 92627

Refer to KSC-11614, volume and number of this NASA Tech Briefs issue, and the page number.
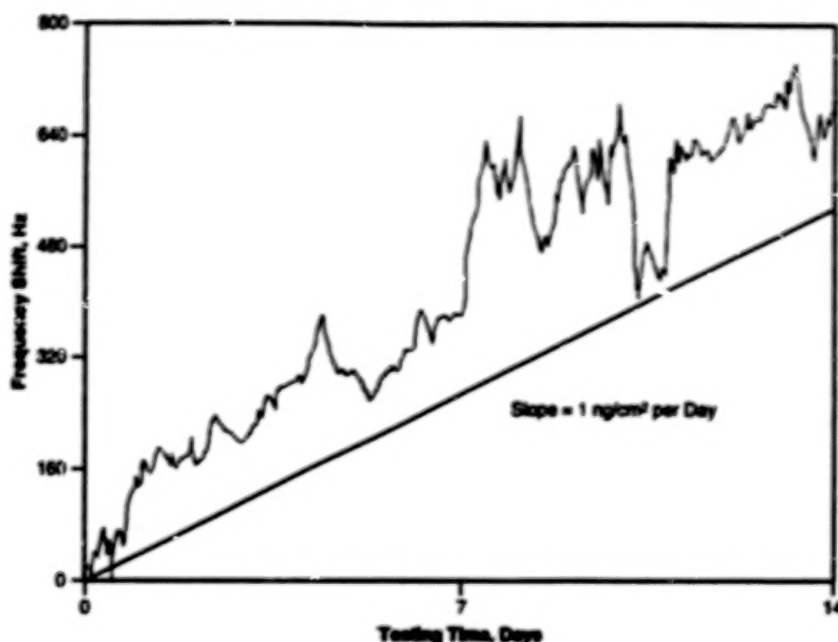
This **Beat-Frequency Shift-vs.-Time** plot was recorded on a temperature-controlled surface-acoustic-wave-resonator real-time NVR monitor over a two-week period. The increases in beat-frequency shift correspond to mass accumulation on the sensing crystal. A 100-Hz shift is equal to 2 ng/cm². Total mass accumulation over the period is 15.3 ng/cm² or 1 ng/cm² per day

Broadband, High-Temperature Ultrasonic Transducer

Materials are chosen for endurance at high temperatures and acoustic coupling and damping.

*Langley Research Center,
Hampton, Virginia*

An acoustic transducer is designed to exhibit broad frequency response and to survive temperatures close to the melting points of brazing alloys. It can be attached directly and continuously to a hot object to be monitored ultrasonically: for example, it can be attached to a relatively cool spot on a workpiece during brazing for taking ultrasonic quality-control measurements.

The transducer is a layered structure based on a piezoelectric layer of lithium niobate. A 1000-Å layer of platinum is deposited on one surface of the piezoelectric layer. Brazing alloy is melted onto a layer of copper 1/16 in. (about 1.6 mm) thick, which was as a substrate and an acoustic-coupling material. The brazing-alloy-coated copper is polished flat.

A shim of brazing alloy is placed between the platinum-coated surface of the lithium niobate and the polished brazing-alloy-coated copper, and then the copper is brazed to the platinum. Bumps of brazing alloy are applied to

the copper at various positions near the lithium niobate to provide for subsequent attachment of the ground braid (shield) of a coaxial cable and of a cover to hold the assembly together. After brazing, the exposed face of the copper is repolished flat.

On the face of the lithium niobate opposite the platinum-coated face, the following layers are added: graphite foil; a flat, parallel electrode plate with a coaxial lead; and an electrical insulator. Optionally, a ceramic frame can be placed around the assembly to insulate the layers electrically and hold them in place. The ground braid of the coaxial cable is then spot-welded to the brazing-alloy bumps.

The polished copper layer is left exposed and is pressed directly against the object to be monitored ultrasonically. Copper was selected as the acoustic-coupling material because its thermal expansion nearly equals that of lithium niobate; this minimizes differential-thermal-expansion stresses that could oth-

erwise be large enough to crack the transducer during heating or cooling. In addition, the acoustic impedance of copper lies midway between those of lithium niobate and steel (a typical object to be monitored could be made of steel) so that it couples acoustic signals between the two materials with minimum loss.

The graphite-foil layer helps to distribute the coupling pressure evenly over the lithium niobate. The graphite is soft and electrically conductive and withstands high and low temperatures. The braze between the copper and the platinum coat on the lithium niobate gives rise to sufficient damping to provide the desired broadband frequency response.

*This work was done by F. Raymond Parker, William P. Winfree, and Danny A. Barrows of **Langley Research Center**. Further information is contained in a TSP [see page 1].
LAR-14615*

# Global Geodesy Using GPS Without Fiducial Sites

Fiducial coordinates are not necessary for global geodetic measurements.

NASA's Jet Propulsion Laboratory, Pasadena, California

The Global Positioning System (GPS) can be used to make global geodetic measurements without the use of fiducial site coordinates. A fiducial site is one with coordinates that are held fixed during analysis and treated as known parameters. Traditionally, fiducial coordinates used for GPS analysis have come from Very Long Baseline Interferometry (VLBI) or Satellite Laser Ranging (SLR).

Baseline lengths and geocentric radii for each site are well determined without having to fix any site coordinates. Given n globally distributed sites, the $n(n-1)/2$ baseline lengths and n geocentric radii form a polyhedron with each site at a vertex and with the geocenter, or center of mass, at the intersection of all the radii. Geodetic information can be derived from the structure of the polyhedron and its change with time.

The no-fiducial approach was tested with data from a global GPS experiment in 1991 involving 21 sites. Baseline length precision, as determined from daily repeatability, was 2 mm + 4 parts per billion for the 17 sites in the Northern Hemisphere. Baseline length accuracy, determined by comparison with VLBI, showed an rms agreement of 2.1 parts per billion. The precision of geocentric radii indicated by daily repeatability was 15 cm. The accuracy of geocentric radii derived from comparison with VLBI yielded an rms agreement of 3.8 cm. Measurements of baseline lengths and geocentric radii determined with the no-fiducial approach are both precise and accurate.
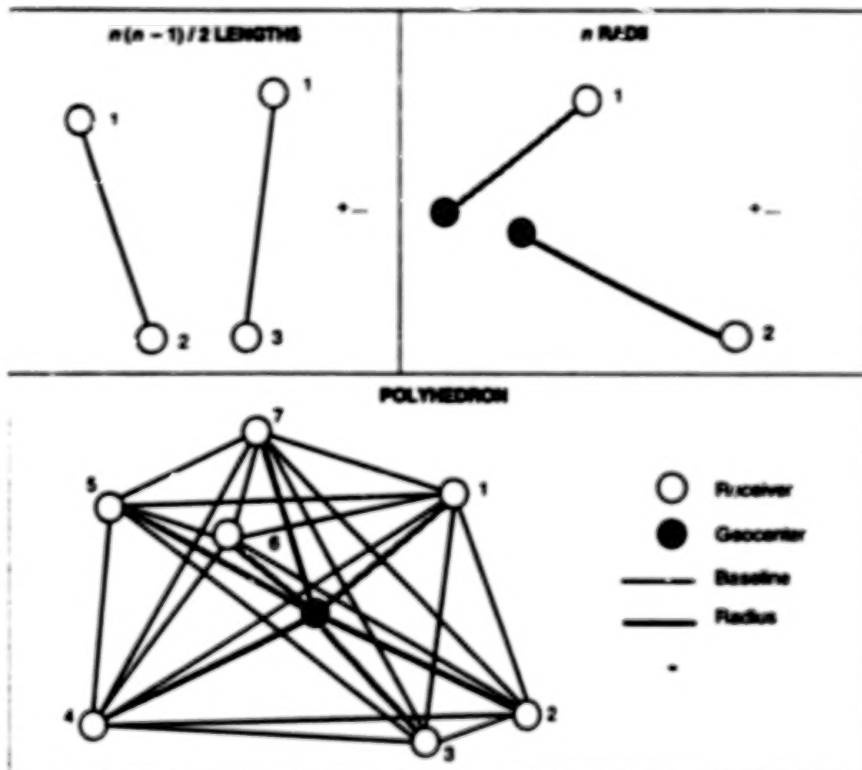
Given n Sites, the $n(n-1)/2$ baseline lengths and n geocentric radii define a closed polyhedron. In this example, $n = 7$. Geodetic information can be derived from the structure of the polyhedron and its change with time.

The no-fiducial approach can be applied to any global geodetic technique. Regional experiments can make use of it by including data from global tracking sites. Fiducial coordinates are not necessary for global geodesy, and, if they are not accurate, holding them fixed can lead to systematic errors.

Improved Raman-Scattering Gas-Species Monitor

High efficiency is achieved by multiple passes of laser beam, fast collection optics.

John F. Kennedy Space Center, Florida

The figure illustrates, schematically, an improved Raman-scattering instrument that provides real-time measurements of the concentration of a gas species of interest mixed with other gases. For example, in the original application, the instrument is used to determine whether there is a flammable or explosive concentration of leaking hydrogen present in an atmosphere that contains varying concentrations of helium, air, and possibly other gases in addition to the hydrogen.

Like other Raman-scattering gas-species-monitoring instruments, this one

offers the advantages of (1) the inherent simple proportionality between the concentration of the species of interest and the intensity of the Raman-scattered light, (2) the independence of Raman scattering from the composition, pressure, and temperature of the other gas(es) with which the gas species of interest is mixed, and (3) consequent simplicity and reliability of calibration, with no need for a second sample chamber containing a reference gas. In comparison with other Raman-scattering gas-species-monitoring instruments, this

one costs less, weighs less, and can be operated more easily, largely because the intense illumination needed to obtain sufficient Raman scattering is provided by smaller, more rugged means: Instead of passing the sample gas through a laser cavity (with consequent need for an active control system to maintain the delicate laser adjustment) or using strong externally supplied illumination (necessitating a bulky, expensive laser), the improved Raman-scattering instrument incorporates a relatively inexpensive external laser and achieves the needed
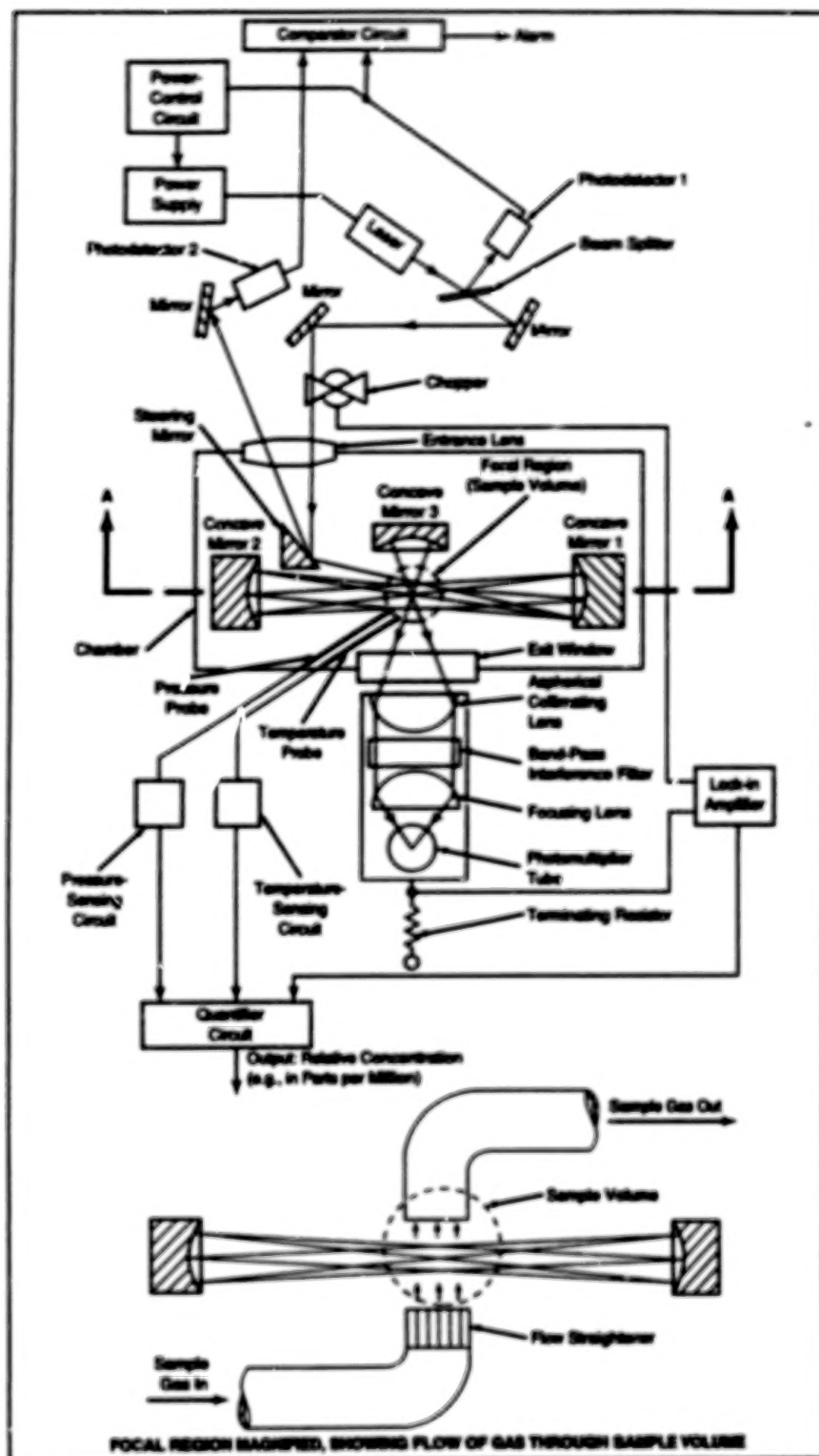
The **Improved Raman-Scattering Gas-Species Detector** indicates the relative concentration of the gas species of interest (hydrogen in this case) in the sampled gas stream that passes through the sample volume.

intensity of illumination by multiple passes of the laser beam through the sample volume. The improved instrument also features more-efficient optics for collecting the Raman-scattered light, so that the external laser can be made smaller than it would otherwise have to be.

The laser in this instrument is of the argon-ion type and operates at a wavelength of 488 nm. A small portion of the laser beam is split off and sent to photodetector 1, the output of which is used to control the laser power supply to maintain the laser beam at constant

power. The laser beam is chopped and then directed into a chamber. The combination of an entrance lens and a steering mirror focuses the beam into a small sampling volume, within the chamber, through which the sample gas mixture is pumped. After passing through the sample volume, the laser beam is reflected back through the sample volume by spherical concave mirror 1, then reflected through the sample volume yet again by spherical concave mirror 2. These mirrors are adjusted to focus in the sample volume, so that the laser beam passes through the sample volume many times (typically as many as 40).

The last bounce returns the laser beam to the steering mirror at an angle slightly different (not as shown in the figure) from that at which it entered, so that it is reflected to photodetector 2 for additional measurement of the power in the laser beam. The output of photodetector 2 is a sensitive measure of the cumulative effect of alignments of the optical components. The outputs of photodetectors 1 and 2 are sent to a comparator, which puts out an alarm if they differ by more than a preset amount, signifying fouling or misalignment of the optics.

Light Raman-scattered from hydrogen (at a wavelength of 612 nm) is collected over a large solid angle (about 1 steradian) by an aspherical collimating lens. A third concave mirror catches Raman-scattered light that travels into the opposite solid angle, reflecting it back through the sample volume and into the collimating lens, so that the amount of Raman-scattered light collected is about double what it would otherwise be. On its way out of the chamber, the light passes through an exit window, which is a glass filter colored to pass light at the hydrogen-Raman-scattering wavelength of 612 nm and suppress scattered laser light at the original 488-nm wavelength. The collimated light goes through an interference filter that passes light in a wavelength band 5 to 10 nm wide centered at 612 nm, thus providing further selectivity to separate the 612-nm Raman signal from background fluorescence, scattered laser light, and ambient light. The collimated Raman-scattered light that remains after band-pass filtering is focused onto the photocathode of a photomultiplier tube.

The output of the photomultiplier is processed via a lock-in amplifier that is synchronized with the chopper, to suppress the dc contribution of the photomultiplier dark current. The amplified

output is processed further by a quantifier circuit. Probes in the sample region measure the pressure and temperature of the sampled gas. A quantifier circuit multiplies the photodetector output by an amount proportional to the absolute temperature of the sampled gas and divides by an amount proportional to the

pressure of the sampled gas to obtain a final output in the form of the relative concentration of the gas of interest (hydrogen in this case) in the sampled gas.

This work was done by Steven Adler-Golden, Neil Goldstein, and Fritz Bien of Spectral Sciences, Inc., for **Kennedy**

Books and Reports

Comparison of Infrared Astronomical Observatories

Performances of observation systems are predicted.

A report presents a comparative study of several proposed astronomical observatories intended to operate in the infrared and submillimeter wavelength range (1 to 1,000 μm). The observatories would be, variously, spaceborne, airborne, and Earth-based. The performances of the observatories for viewing point sources were predicted on the basis of estimated telescope parameters, the celestial background emission, crowding of celestial sources, and per-

formances of detectors. None of the proposed observatories was found to be the optimum general observatory for the entire wavelength range and the full variety of intended observations, though all were found to offer much more sensitivity to weak signals than their predecessors do. For broadband observations, crowding of sources was found to be the factor that exerts the most influence over the lower limit to the detectable signal level. As a result, large apertures are more important than are low optical-system temperatures in detecting the faintest signals in broadband measurements. For moderate spectral resolution at wavelengths greater than 50 μm, the thermal background from noncryogenic telescopes is large and the coldest observatories should be the most sensi-

tive. At wavelengths less than 50 μm, none of the proposed observatories would be subject to significant emission within its optical system, and the most sensitive observatory would be the one with the largest aperture. At high spectral resolution, on the other hand, detectors would be affected very little by thermal background from any source, and for sensitivity at all wavelengths it would be necessary to use large apertures.

This work was done by Donald Rapp of Caltech for **NASA's Jet Propulsion Laboratory**. To obtain a copy of the report, "Estimation and Optimization of Performance of Aerospace Infrared and Submillimeter Observation Systems," see TSP's [page 1].
NPO-19318
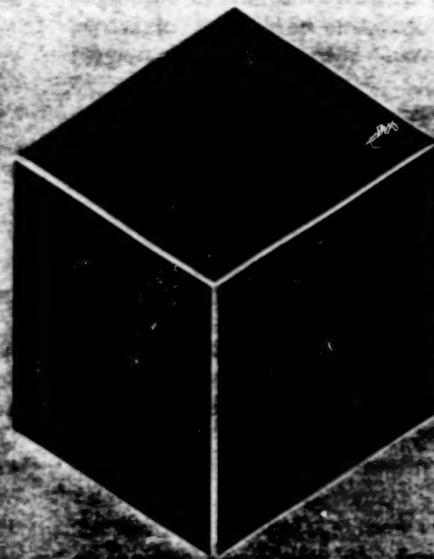
Materials

Hardware, Techniques, and Processes

Making Composite-Material Parts at Moderate to High Rates

Production lines and electron-beam curing would
replace batch processing and heat curing.

Langley Research Center,
Hampton, Virginia
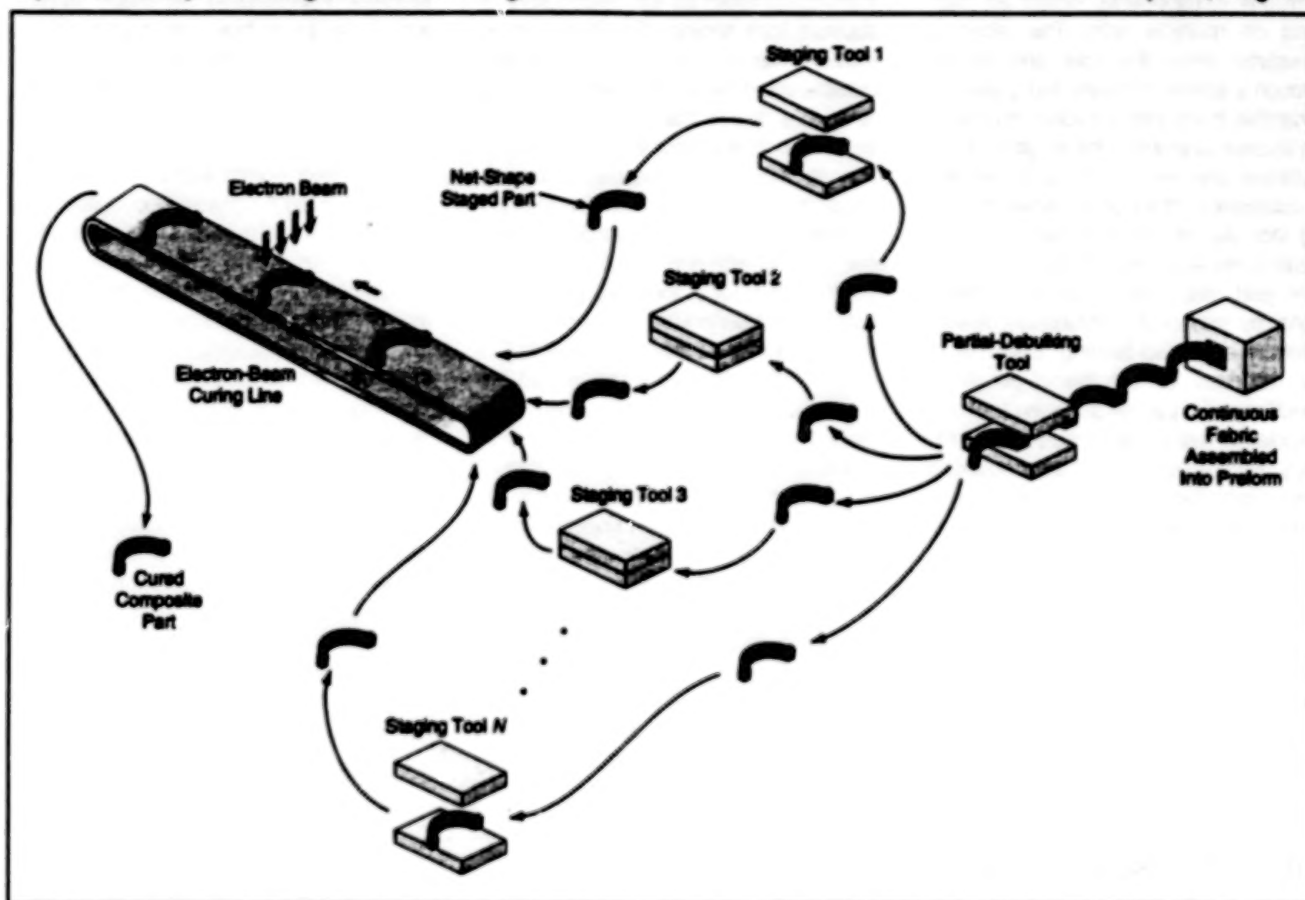
Figure 1. This **Press-Forming Process** would produce composite-material parts at moderate to high rates, in production-line fashion instead of by batches as is done now.

Composite-material (matrix/fiber) structural components would be manufactured at moderate to high rates in production-line-style processes, according to a proposal. Until now, most composite-material parts have been made in labor-intensive batch processes that include time-consuming steps like curing in autoclaves. In the proposed method, the production lines would be largely automated and would take advantage of the fact that matrix resins can be cured by electron beams in addition to heat. The net result should be reductions in production times and costs.

The automation and the continuous nature of the proposed processes would depend on the availability of fabric preforms impregnated with matrix material. The yarns used to make the preforms could be coated with matrix material by any of several commercial processes, then woven into the preforms by use of advanced techniques for producing fabric components with complicated shapes.
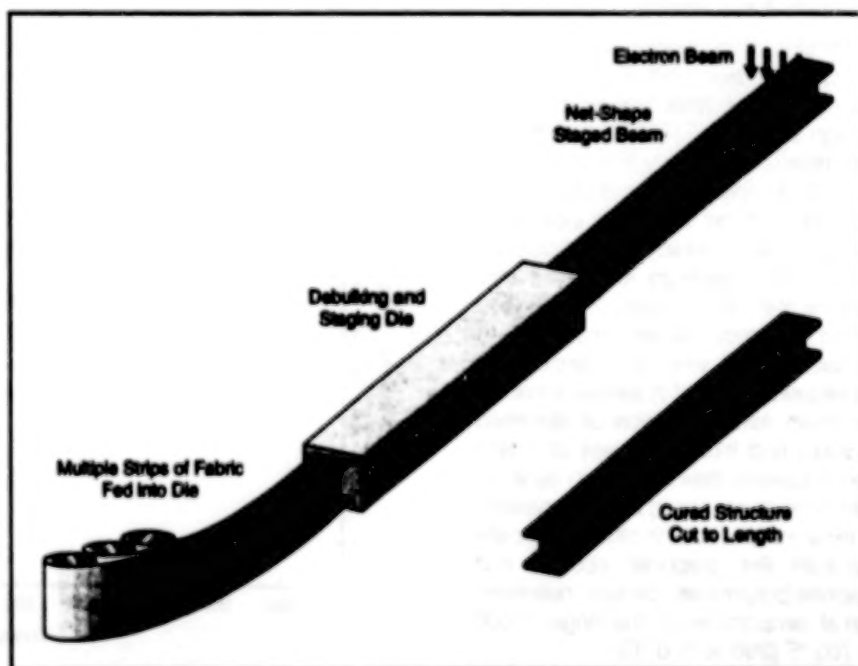
Figure 2. This **Pultrusion Process** would incorporate features of both conventional pultrusion and of the press-forming process shown in Figure 1.

Figure 1 illustrates a quasi-continuous press-forming process according to the proposal. Impregnated net-shape fabric destined to become layers of composite structural components would be supplied on multiple rolls. The fabric is unwound from the rolls and drawn through a series of rollers and guides to assemble them into a thicker, multilayer continuous preform. Unit lengths of the multilayer preform would be processed, in succession, through a partial-debulking tool. As its name implies, this tool would compress the unit lengths of preform part way toward its final dimensions, by use of a combination of mild pressure and mild heating. Because of the mildness of the partial-debulking conditions, the partial-debulking tool and associated equipment should be relatively inexpensive. Typical debulking times would be on the order of 1 min.

After partial debulking, each unit length of preform would be drawn out of the partial-debulking tool and cut from the continuous assembled fabric strip. Each resulting unit preform, now destined to become a composite structural component, would be placed in a staging tool and using heat and pressure would melt the matrix material and facilitate debulking of the preform to final dimensions.

Depending on the type of matrix material, the heating of the preform in the staging tool could partially heat-cure the matrix material to such a degree that the preform could retain its final shape without support from tooling. Non-heat curable matrix materials that are electron-beam curable could be solidified without curing to such a degree that the preform could also retain its final shape without support from tooling. The time needed for staging would be on the order of 5 min; because of greater duration of the staging cycle in comparison with the debulking cycle, a number of staging tools would be kept running simultaneously to keep up with the output of the partial-debulking tool.

The composite structure would be removed from the staging tool and placed in a chamber where the matrix material would be cured by exposure to an electron beam. Typical electron-beam-curing times are expected to be of the order of several minutes — significantly shorter than typical autoclave cure cycles. Another advantage of the proposed method is that unlike heat curing, electron-beam curing does not cause chemical reactions of the type that forms voids and other anomalies, which can weaken the finished composite parts.

Figure 2 illustrates a continuous pultrusion process, according to the proposal, for making composite I-beams. As in the proposed press-forming process, impregnated net-shape fabric would be drawn from rolls and assembled into a thicker, multilayer continuous preform. The continuous preform would be fed into a heated die, the cross section of which would taper down to the desired I-beam cross section, so that the preform would be gradually debulked to the final cross section as it moved along. The preform would continue along a constant-final-cross-section length of the die, where it would be partially cured or allowed to solidify. The composite structure would be pulled continuously from the die and cut to length as unit lengths emerge. The staged I-beams would then be electron-beam cured.

This work was done by Gary L. Farley of the U. S. Army Vehicle Structures Directorate at Langley Research Center. No further documentation is available.

Inquiries concerning rights for the commercial use of this invention should be addressed to the Patent Counsel, Langley Research Center [see page 1]. Refer to LAR-15128.

High-Temperature Graphite/Phenolic Composite

Pressure lower than usual in curing prevents high-temperature damage by trapped moisture.

Marshall Space Flight Center, Alabama

A graphite-fiber/phenolic-resin composite material retains relatively high strength and modulus of elasticity at temperatures as high as 1,000°F (538°C) (see figure). The material costs only 5 to 20 percent as much as refractory materials do. The fabrication of the composite includes a curing process in which the application of full autoclave pressure is delayed until after the phenolic resin gels. This modified curing process allows moisture to escape, so that when the composite is subsequently heated in service, there will be much less expansion of absorbed moisture and thus much less of a tendency toward delamination. In contrast, internal pressure caused by the expansion of moisture absorbed in other composite materials like graphite/ epoxies and graphite/polyimides causes delamination at temperatures in the range of 500 to 700 °F (260 to 370 °C).

The high-temperature graphite/phenolic composite was developed for the nose cone of the external fuel tank of the Space
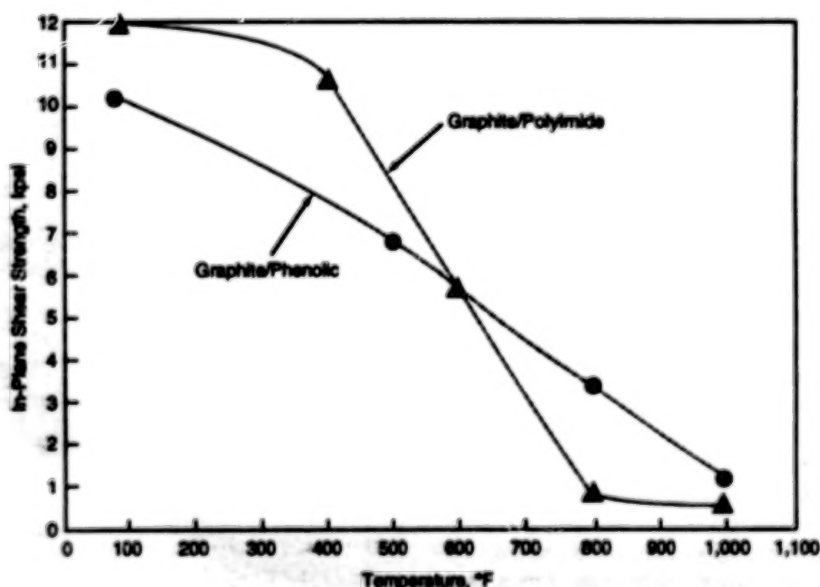
The Shear Tensile Strength of a Graphite-Fiber/Phenolic-Matrix Composite made by the modified process decreases with increasing temperature, but at 1,000 °F, it remains greater than that of a composite made of the same fiber material with a matrix of polyimide.

Shuttle. Wind-tunnel tests; high-temperature subcomponent tests; and full-scale structural, dynamic, acoustic, and damage-tolerance tests have shown that it can withstand the severe environments encountered by the nose cone in flight. Other potential aerospace applications for this material include leading edges, parts of nozzles, parts of aircraft engines, and heat shields. Potential terrestrial and aerospace applications include structural firewalls and secondary structures in aircraft, spacecraft, and ships. (Phenolic laminates have traditionally been used for secondary structures on aircraft because of their resistance to burning and low emission of smoke and toxic gases when exposed to flame; the present high-temperature graphite/phenolic material would add retention of strength at high temperature to these advantages.)

The modified curing process used to make the high-temperature graphite/phenolic composite can be adapted to composites of phenolic with other fiber reinforcements like glass or quartz. These composites might be useful as high-temperature circuit boards and electrical insulators.

The modified curing process consists of the following steps:
1. Full vacuum is applied to the composite part in an autoclave.
2. The autoclave is heated gradually, during 160 minutes, to a temperature of 175°F (79°C), then held at that temperature for 60 minutes.
3. The temperature is increased, at a rate of 1.0 to 1.5°F (about 0.6 to 0.8°C) per minute, until 220°F (104°C) is reached, then is held at that level for 78 minutes.
4. At 78 minutes, the applied autoclave pressure is ramped up to 5 psi (34 kPa) in 6 minutes, then the temperature is held for an additional 36 minutes.
5. The temperature is increased, at a rate of 1.0 to 1.5°F (about 0.6 to 0.8°C) per minute, to 240°F (116°C) and held there for 30 minutes.
6. At the same rate as in step 5, the temperature is increased to 350°F (177°C), then held there for 60 minutes.
7. The part is cooled, at a rate of 1 to 4°F (about 0.6 to 2.2°C) per minute, to 150°F (66°C).
8. The part is removed from the auto-

clave but kept under vacuum until it has cooled to 100°F (38°C).
9. The part is then subjected to a 42-hour postcure at atmospheric pressure in which its temperature is increased in steps, eventually reaching 415°F (213°C).

This work was done by Ellis C. Seal, Venu P. Bodepudi, Robert W. Biggs, Jr., and John A. Cranston of Martin Marietta Corp. for Marshall Space Flight Center. Further information is contained in a TSP [see page 1].

Title to this invention has been waived under the provisions of the National Aeronautics and Space Act [42 U.S.C 2457(f)], to the Martin Marietta Co. Inquiries concerning licenses for its commercial development should be addressed to

Martin Marietta Corporation
Attn: Gay Chin, Associate
General Counsel
6801 Rockledge Drive
Bethesda, MD 20817

Refer to MFS-28759, volume and number of this NASA Tech Briefs issue, and the page number.

Material Removes Heavy Metal Ions From Water

Unlike other ion-exchange resins, it can even remove metal ions from hard water.

Lewis Research Center,
Cleveland, Ohio

A new high capacity ion-exchange polymer material has been shown, in laboratory tests, to remove toxic metal cations from contaminated water. This material offers several advantages. It has high sensitivities for such heavy metals as lead, cadmium, and copper and is capable of reducing their concentrations in aqueous solutions to the parts-per-billion range. Another important feature of the material is that, unlike many commercial ion-exchange materials (resins), it removes the cations even when calcium is present. The calcium present in water saturates the commercial resins, thereby blocking the adsorption of heavy metal ions. Thirdly, the material can be made into a variety of forms, such as thin films, coatings, pellets, and fibers. As a result, it can be adapted to many applications to purify contaminated water, which usually is hard wherever it is found, whether in wastewater-treatment systems, lakes, ponds, industrial plants, or homes.

The electroplating and mining industries, for example, produce large amounts of wastewater that contain hazardous amounts of mercury, lead,

cadmium, silver, copper, and zinc ions. They are required by law to reduce the concentrations of these toxic metals in their wastewater before it is discharged into sewers, lakes, and streams. The technology that existed prior to the development of the high-capacity ion-exchange material appeared to be inadequate for meeting new, lower limits.

Tests of the adsorption capacity of this material were conducted on laboratory samples of aqueous solutions, each contaminated with only one of the following ions: lead, copper, mercury, cadmium, silver, chromium(III), nickel, zinc, yttrium, and mercury, without calcium. Two solutions — one containing copper and one containing lead — also contained calcium. Tests were also conducted with samples of rinse water, obtained from an electroplater, that contained a mixture of heavy-metal ions and some unknown contaminants, e.g., brighteners and chelating agents.

The most noteworthy conclusions drawn from the tests are the following:
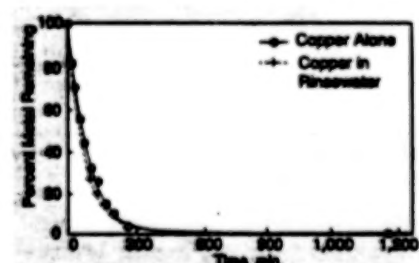• The rates of adsorption and the mass adsorbed per gram of the ion-

Figure 1. **Copper Is Adsorbed in the Ion-exchange polymer material at nearly equal rates from both a solution in which it appears alone and from rinsewater from a copper-electroplating process, in which it appears along with other elements.**
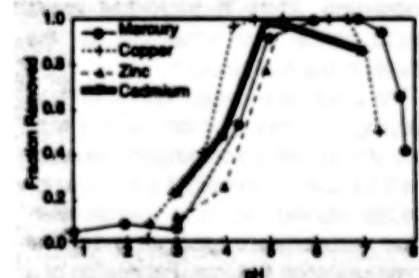

Figure 2. **The Adsorption of Metal by the ion-exchange polymer material depends on the pH of the solution.**

exchange polymer depended on the pH levels of the solutions and on the initial concentrations.

- The adsorption of an ion is not affected by the presence of other ions (including calcium) in the mixture, so long as there is sufficient ion-exchange material present to adsorb all ions. This is shown in Figure 1.
- The amount of an element adsorbed varies with the pH of the solution. This is shown in Figure 2 for cadmium, mercury, copper, and zinc.
- The final concentrations of most of the elements tested are below the allowable limits for the concentrations of those elements in discharge water as specified by the Environmental Protection Agency.

Another important feature of the ion-exchange polymer material is that the adsorbed metals can be easily reclaimed by either a destructive or a nondestructive process. In the destructive process, the spent ion-exchange polymer is burned, thereby producing carbon dioxide, water vapor, and oxides of the adsorbed metals, which can be recycled. In the nondestructive process, the heavy metals are removed from the polymer and reclaimed by an acid stripping process. The polymer is then reusable and the metal concentrate can be recycled.

Other tests have shown that the ion-exchange polymer can be made inexpensively and is

- Easy to use;
- Strong, flexible, and not easily torn; and

- Chemically stable in storage, in aqueous solutions, and in acidic or basic solution.

Although no toxicity tests have been performed, it is anticipated that this is safe and nontoxic to handle.

This work was done by Warren H. Philipp, Jr., and Kenneth W. Street of **Lewis Research Center,** *Carol Hill of the University of Akron, and Joseph M. Savino of Cleveland State University. Further information is contained in a TSP [see page 1].*

This invention is owned by NASA, and a patent application has been filed. Inquiries concerning nonexclusive or exclusive license for its commercial development should be addressed to the Patent Counsel, Lewis Research Center [see page 1]. Refer to LEW-15576.

Antisymmetric Layup of Precise Composite Laminates

Ply-orientation errors would be redistributed to cancel their effects.

NASA's Jet Propulsion Laboratory, Pasadena, California
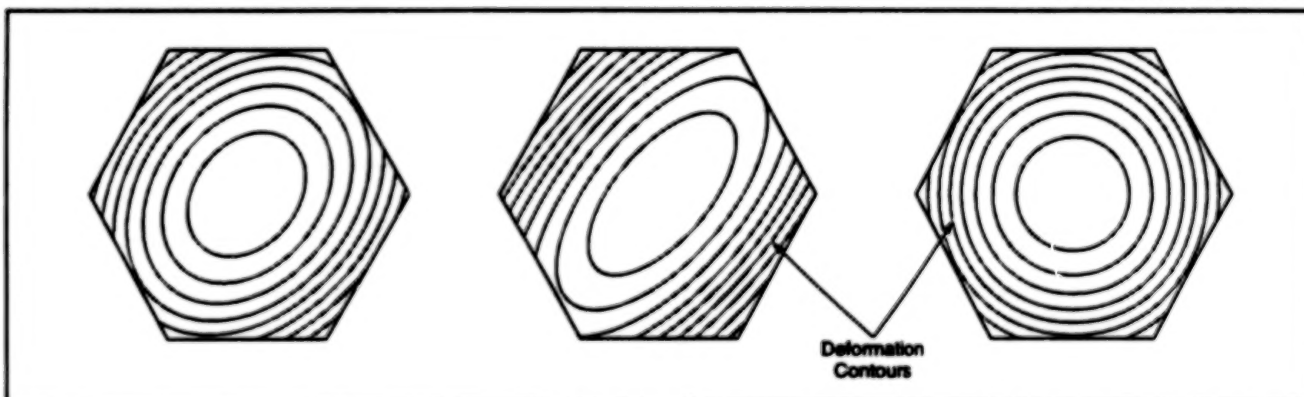
Deformation Contours computed for a 12-ply hexagonal-outline curved mirror-substrate panel demonstrate the effectiveness of the method proposed for reduction of warp.

Warping of precise composite-material (graphite-fiber/epoxy-matrix) laminated panels would be reduced, according to a proposal, by an improved combination of design and method of fabrication. The essence of the proposal is to stack the plies during fabrication in such a pattern that the effects of unavoidable ply-orientation errors in individual layers would cancel each other out, on the whole, in the final product.

The proposal emerged from a study of warping of composite-material laminated face sheets that are undergoing development for use as lightweight substrates for precise, curved mirrors in submillimeter-wave astronomical telescopes and optical communication systems. Fabrication of a typical laminated composite-material face sheet usually includes a layup of a number (usually 8 to 32) of plies of prepreg material (sheets of parallel fibers embed-

ded in uncured or partially cured matrix material). During layup, the various plies are oriented with their fibers at various angles from a reference direction. Of course, the prepreg plies are resinous materials that are difficult to handle and align precisely.

After layup, the face matrix material is cured — usually by heating. Experimental observations indicate that such face sheets tend to warp immediately after curing. In the case of a face sheet to be used as a mirror substrate, warps result in optical aberrations and in changes in curvature (which cause changes in focal lengths). In the study, experience and intuition led to the hypothesis that random ply-orientation errors constitute a major cause of warping. This hypothesis was tested by detailed finite-element mathematical modeling of a typical 12-ply face sheet, using the best available data on the

properties of the matrix and fiber materials. It was found that the magnitudes of figure errors caused by random ply-orientation errors of a few tenths of a degree to a degree were comparable to those observed experimentally. Inasmuch as random ply-orientation errors of as much as 1° are expected to routinely occur during layup, it was therefore concluded that random ply-orientation errors can account for major parts of manufacturing errors.

The proposed method is not intended to accomplish the impossible task of eliminating these errors but, instead, to reduce or eliminate the net effects of these errors on the surface figures of the face sheets. The plies in a given panel would be laid up in such a way that even though random ply-orientation errors exist, these errors would be symmetrically placed about the mid-plane of the

32

NASA Tech Briefs, March 1995

panel, so that the effects of these errors would tend to cancel each other.

To demonstrate the effectiveness of this method, a finite-element mathematical model was used to compute the deformations, under a uniform thermal load, of a 12-ply curved, hexagonal-outline mirror face sheet in which successive plies were nominally oriented at angles of $[0°,60°,-60°,60°,0°,0°,60°,-60°,60°,0°]$. The figure shows deformation contours predicted by the model. The top part of the figure shows the warp that occurs in the case of a 1° orientation error in the top ply. The middle part of the figure shows that the warp is approximately doubled

when the same 1° orientation error exists in the top and bottom plies. The bottom part of the figure shows that the warp is essentially zero when 1° orientation errors occur in both plies but the errors are in opposite directions: as desired, the effects of the errors in the top and bottom plies have canceled each other.

The method could be implemented by a proposed layup procedure that would include folding to distribute the ply-orientation errors antisymmetrically about the mid-plane of a laminate. For a 12-ply laminate, one should stack the first three plies at the usual angles 0°, 60°, and -60°, but the length of each ply should

be four times the width. The resulting elongated stack of three plies would be folded to produce a 6-ply laminate, then folded again to produce a 12-ply laminate. As a result of the folding, there would be two sets of three plies with opposite orientations of ply errors on both sides of the midplane, providing for cancellation of the effects of ply errors on the laminate as a whole.

This work was done by Donald Rapp, Michael C. Lou, and Chin-Po Kuo of Caltech for NASA's Jet Propulsion Laboratory. Further information is contained in a TSP [see page 1].
NPO-19162

Porous Silica Sol-Gel Glasses Containing Reactive V$_2$O$_5$ Groups

These materials may prove useful as sensors, scrubbers, or catalysts.

NASA's Jet Propulsion Laboratory,
Pasadena, California

Porous silica sol-gel glasses into which reactive vanadium oxide functional groups have been incorporated exhibit a number of unique characteristics. Because they bind molecules of some species both reversibly and selectively, they may be useful as chemical sensors or indicators or as scrubbers to remove toxic or hazardous contaminants. These materials have also been found to oxidize methane gas photochemically: this suggests that they may be useful as catalysts for conversion of methane to alcohol and for oxidation of hydrocarbons in general. Moreover, by incorporating various amounts of other metals into silica sol-gel glasses, it should be possible to synthesize new materials with a broad range of new characteristics.

In experiments, it was found that glasses of this type can be synthesized by the co-condensation of tris-isopropoxyvanadium oxide with tetraethylorthosilicate. The resulting porous glasses are transparent and can contain up to 0.5 mole percent vanadium oxide. Because they are purely inorganic, these glasses can be stabilized at high temperatures without affecting their bulk properties. What is particularly unique about these materials is that the vanadium oxide centers, which are integrated into the silica framework, retain most of their chemical reactivity and, in effect, form discrete reaction sites along the porous channels of the silica gel.

These materials have been shown to coordinate small molecules at the metal centers; the coordination reaction is accompanied by a change in color that

Absorbed Molecule	Color
Water	Orange
Hydrogen Sulfide	Amber
Ammonia	Yellow
Acetonitrile	Yellow
Formic or Acetic Acid	Green

Absorption of These Molecules in silica sol-gel glasses that contain reactive vanadium oxide groups is reversible and gives rise to the noted color in each case.

is specific to the type of molecules being absorbed. For example, vanadium-silica gels that have been dried and stabilized at a temperature of 500 °C are completely transparent; however, upon exposure to moist air, they slowly turn orange. The change in color induced by the uptake of water is completely reversible. In addition to water, other molecules also coordinate reversibly to the metal centers in the dried gel and impart colors. Examples of these molecules and colors are shown in the table. Clearly, the striking changes in color that accompany absorption of these molecules suggest that the developmental materials may be useful as chemical indicators.

In addition, the vanadium centers coordinate certain molecules preferentially to others. For example, formic acid displaces water, with a concomitant change in color from orange to green. Similarly, water is absorbed preferentially to hydrogen sulfide. In addition, some materials are not absorbed at all (for example, ethylene, pyridine, and formamide). In short, along with their chemical-indicating capabilities, these materials can be used to remove certain impurities from gases or liquids selectively.

Oxidation/reduction chemistry also occurs at the metal centers. A material of this type can be reduced under hydrogen gas at 420 °C or by photolysis at a wavelength > 350 nm at room temperature to yield a sapphire-blue material characteristic of vanadium(IV). More significantly, photolysis of the material under an atmosphere of pure methane also causes reduction of the vanadium and oxidation of the methane: this appears to occur through activation of the carbon-hydrogen bond in the methane molecule, as methyl radicals can be detected via electron-spin-resonance spectroscopy. Oxidation of methane is difficult, usually requiring high temperatures and pressures and has only rarely been accomplished photochemically. That these materials appear to oxidize methane efficiently and at relatively low energies suggests that they may be catalytic toward the oxidation of hydrocarbons.

This work was done by Albert E. Stiegman of Caltech for NASA's Jet Propulsion Laboratory. Further information is contained in a TSP [see page 1].

In accordance with Public Law 96-517, the contractor has elected to retain title to this invention. Inquiries concerning rights for its commercial use should be addressed to

William T. Callaghan, Manager
Technology Commercialization
JPL-301-350
4800 Oak Grove Drive
Pasadena, CA 91109
Refer to NPO-19135, volume and number of this NASA Tech Briefs issue, and the page number.

Cubic GaS: A Surface Passivator for GaAs

Thus passivated, GaAs can be a substrate material for metal/insulator/semiconductor (MIS) capacitors.

Lewis Research Center,
Cleveland, Ohio

Thin films of the cubic form of gallium sulfide (GaS) can be formed on the surfaces of gallium arsenide (GaAs) substrates via metal/organic chemical vapor deposition (MOCVD). As formed in nature and in other chemical processes, GaS normally has a hexagonal crystal lattice. The cubic form is an artificial form created by MOCVD from the engineered single source precursor material [(t-Bu)GaS]$_4$, where "t-Bu" denotes the tertiary butyl [C(CH$_3$)$_3$] group (see Figure 1).

The deposited cubic GaS, the crystalline lattice of which is matched to that of the substrate GaAs, neutralizes electrically active defects on the surfaces of both n-doped and p-doped GaAs. This enables the important GaAs-based semiconducting materials to serve as substrates for metal/insulator/semiconductor (MIS) capacitors, which are critical components of many high-speed, low-power semiconductor devices.

Cubic GaS may also enable the fabrication of ZnSe-based blue lasers and light-emitting diodes. Because GaS is optically transparent, it could also be deposited to form window layers for such optoelectronic devices as light-emitting diodes, solar optical cells, and semiconductor lasers. Its transparency may also make it useful as an interconnection material in optoelectronic integrated circuits. It may also be useful in peeled-film technology because it can be selectively etched from GaAs.

With respect to utility in most electronic devices, GaAs has properties superior to those of silicon: it has higher electron mobility and drift velocity and a shorter minority-carrier lifetime than does silicon. Typically, a GaAs-based device exhibits 6 to 10 times the speed and Y_{10} to Y_6 the power consumption of a Si-based device of otherwise similar design and function. Until now, however, gallium arsenide has usually not been the semiconductor of choice because it lacked a suitable insulating layer necessary for the formation of MIS capacitors.

By physical and chemical mechanisms that are not yet fully understood, a deposited layer of cubic GaS neutralizes electrically active defects on the surface of GaAs. Presumably, the defects are unpaired bonds at the gallium and arsenic lattice sites. The experi-
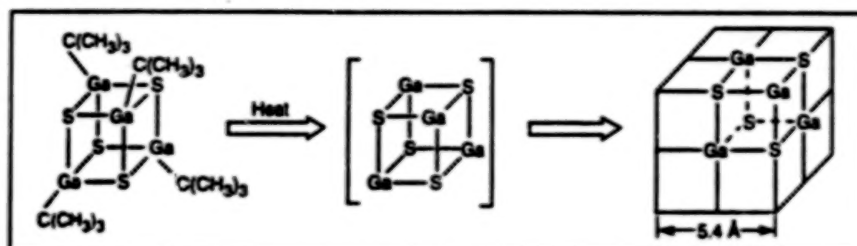
Figure 1. A Passivating Layer of Cubic GaS is deposited on the surface of GaAs at a temperature less than 400 °C, by use of an engineered precursor material that yields the desired cubic crystal lattice.
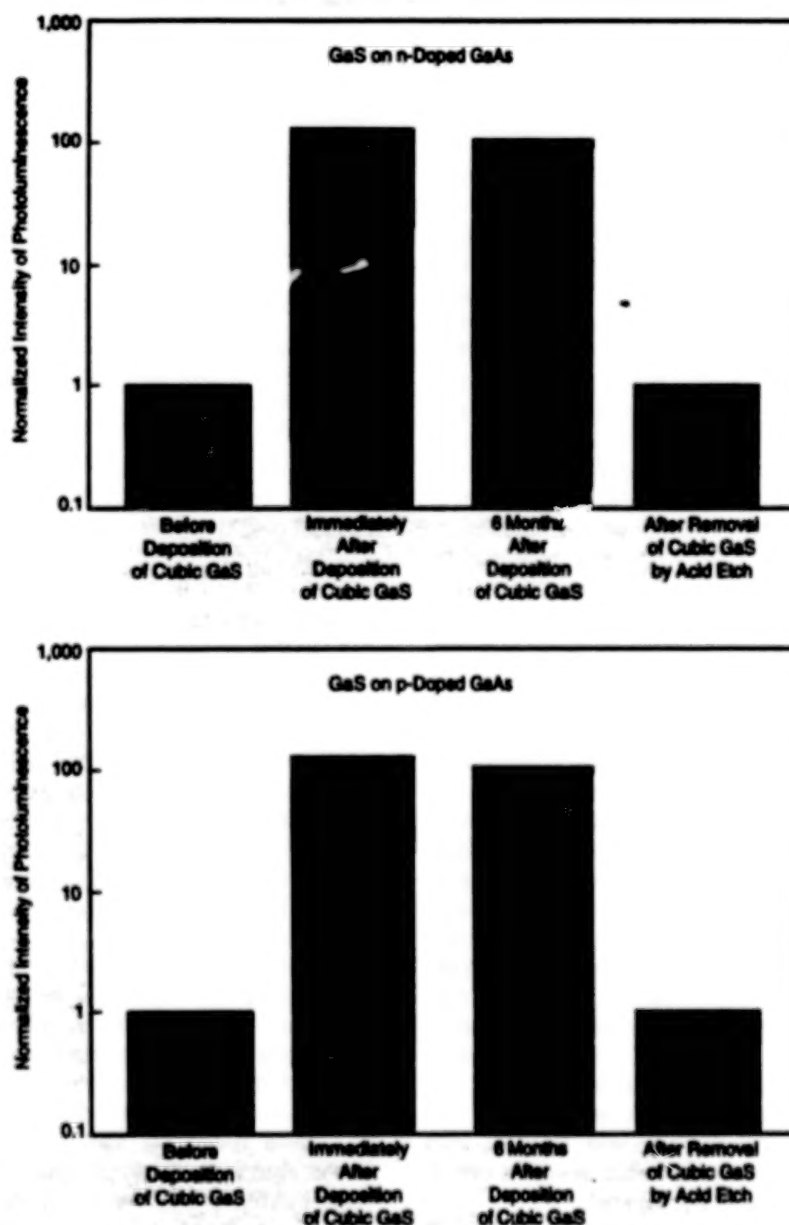
Figure 2. Normalized Photoluminescence Intensities were obtained on specimens of GaAs with and without passivating layers of cubic GaS.

mental evidence available when the information was submitted for this article suggests that the lattice of GaS is matched to that of GaAs and that GaS terminates the unpaired bonds lattice point by lattice point. Another possibility is that the GaS supplies sulfur (a known passivator of GaAs) to the GaAs surface and simultaneously covers the sulfur-terminated GaAs with a layer of GaS that prevents the absorption of oxygen, which would normally destroy the sulfur passivation.

Passivation of GaAs surfaces by cubic GaS was observed in experiments by comparing photoluminescence from GaAs surfaces with and without GaS overlayers. The intensity of the photoluminescence resulting from the generation of electron/hole pairs via irradiation at a wavelength of 514 nm by an argon-ion laser was found to increase with passivation because the passivation eliminated the surface states that give rise to nonluminescent pathways of recombination. As shown in Figure 2, the intensities of photoluminescence from passivated n-doped and p-doped GaAs increased by a factor of about 100 over those of the bare n-doped and p-doped GaAs surfaces. After the GaS layers were etched off by use of HCl, the intensities of photoluminescence of the bare GaAs surfaces returned to their starting values, indicating that the bulk properties were not altered by the deposition of cubic GaAs. Most strikingly, there was little decrease in the intensities of photoluminescence even after storage in ambient laboratory conditions, with no attempt to exclude oxygen or atmospheric moisture, for 6 months after deposition.

Computer Programs

Electronic Components and Circuits

Physical Sciences

Mechanics

Machinery

Mathematics and Information Sciences

Computer Programs

Electronic Components and Circuits

Program for Optimization of Antenna Structures

This program calculates path-length and pointing errors.

The JPL-ANTOPT computer program is designed to help engineers optimize microwave antenna structures by use of path-length- and pointing-error-analysis calculations. This program is a package of codes and subroutines to be added to the MSC/NASTRAN program.

Lengths of signal-propagation paths and pointing errors are important measures of structure-related performance of an antenna. JPL-ANTOPT treats the errors as scalar displacements in static-loading cases. These scalar displacements can be subject to constraint during an optimization process. The path-length and pointing-error calculations in JPL-ANTOPT supplement the other optimization and sensitivity capabilities of NASTRAN. The analysis and design functions are implemented as "DMAP ALTERs" to the Design Optimization (SOL 200) Solution Sequence of MSC/NASTRAN version 67.5.

The path-length error is calculated as the weighted root-mean-square error of a paraboloid that best fits the deformed primary reflector surface in a half-path-length sense. The antenna-pointing-error calculation combines the orientation of the best-fitting paraboloid with the displaced positions of the secondary reflector and the phase center of the microwave feed. This error can be calculated relative to the position of an elevation-angle transducer on the antenna. The results of the path-length and pointing-error analyses are reported in tables

for each static sub-case. The added codes for analysis and design of antennas do not modify or interfere with the operation of the original optimization code and are compatible with all the other sensitivity and design options in SOL 200.

JPL-ANTOPT is written in MSC/NASTRAN's Direct Matrix Abstraction Programming (DMAP) language for use on any computer running MSC/NASTRAN 67.5. A test problem is included on the distribution medium. All files are in ASCII format. The standard medium for distribution of JPL-ANTOPT is a 3.5-in. (8.89-cm), 1.44MB diskette in UNIX tar format. Alternate distribution media and formats are available on request. JPL-ANTOPT was developed in 1993 and is a copyrighted work with all copyright vested in NASA.

MSC/NASTRAN is a trademark of the MacNeal-Schwendler Corporation.

This program was written by Douglas Strain of Caltech for NASA's Jet Propulsion Laboratory. Further information is contained in a TSP [see page 1].
NPO-19349

Physical Sciences

Program for Displaying Computed Electromagnetic Fields

EM-ANIMATE displays and animates near-field and surface-current outputs of programs like MOM3D.

The EM-ANIMATE computer program is a specialized visualization program that displays and animates the output data on near fields and surface currents computed by an electromagnetic-field program — in particular MOM3D (LAR-15074). The EM-ANIMATE program is based on windows and contains a user-friendly, graphical interface for setting viewing options, selecting cases, manipulating files, and the like.

EM-ANIMATE displays the magnitudes of fields and surface currents as smooth, shaded color fields (color contours), ranging from minimum to maximum values. The program can display either the total or the scattered electric

field in either time-harmonic animation mode or in root-mean-square (rms) average mode. The default setting is an initial setting that matches the maximum and minimum values within the sets of field and surface-current data. The user can also optionally control the setting. Field and surface-current values are animated by calculating and viewing the solution at increments of time that correspond to increments of phase selectable by the user in the range from 0 to 2π radians.

The surface currents can also be displayed in either time-harmonic animation mode or in rms average mode. In rms mode, the color contours do not vary with time, but show the time-averaged magnitudes of the field and surface-current solutions. In either time-harmonic or rms average mode, the magnitude and direction of the electric field and of the surface current can be displayed as a scaled vector arrow at each field grid point or surface node point. The vector-arrow display for the field and the vector-arrow display for the surface current can be put on separately or concurrently. The speed of animation is increased by turning off the display of vector arrows. The vector arrows must be shown as varying with time even in the rms mode because otherwise the time-averaged vectors would have zero lengths.

Optionally, some properties of surfaces can be viewed. These include surface grids, the value of resistance assigned to each element of the grid, and the power dissipated in each such element.

The EM-ANIMATE program accepts as many as 10 different surface-current cases, each consisting of as many as 20,000 node points and 10,000 triangle definitions, and animates one of these cases. This capability is used to compare distributions of surface currents in the presence of initial excitations incident from various directions and/or various orientations of the electric fields. The program can accept as many as 50 planes of field data, each plane containing a grid of 100 by 100 field points. These planes of data are selectable by the user and can be viewed individually or concurrently.

With the preset limits described above, the program requires 55 megabytes of core memory to run.

These limits can be changed in header files to accommodate the available core memory of an individual work station. The amount of memory needed to store the field and surface-current data can be estimated as follows: Approximate memory in bytes equals [the number of nodes on each surface × the number of surfaces × 14 (the number of variables) × the number of bytes per word (typically 4 bytes per floating point)] + [the number of field planes × the number of nodes per plane × 21 (the number of variables) × the number of bytes per word]. The total size of memory needed then equals approximately 400,000 bytes plus the amount for data estimated as explained above.

The animation calculations are performed in real time at any time step set by the user. For Silicon Graphics work stations that include multiple processors, this program has been optimized to perform these calculations on multiple processors to increase the speed of animation. The optimized program uses the SGI PFA (Power FORTRAN Accelerator) library. On single-processor computers, the parallelization directives are seen as comments in the program and have no effect on compilation or execution.

EM-ANIMATE is written in FORTRAN 77 for implementation on SGI IRIS work stations running IRIX 3.0 or later. A minimum of 55Mb of random-access memory is needed for execution of this program. However, the code can be modified to accommodate the available memory of an individual work station. For execution of the program, 24-bit, double-buffered color capability is suggested but not required. Sample input and output files and a sample executable code are provided on the distribution medium. Electronic documentation is provided in PostScript format and includes ASCII help files. The standard distribution medium for EM-ANIMATE is a 0.25-in. (6.35-mm) streaming-magnetic-IRIX-tape cartridge in UNIX tar format. EM-ANIMATE is also available as part of a package, COS-10048, that includes MOM3D, an IRIS program that computes near-field and surface-current solutions of electromagnetic-field equations. This program was developed in 1993.

This program was written by Kam W. Horn of **Langley Research Center**. *Further information is contained in a TSP [see page 1].*
LAR-15075

Method-of-Moments Code for Electromagnetic Scattering

This program computes scattered and total near fields and scattering matrices.

MOM3D is a FORTRAN computer program that implements a method-of-moments algorithm for analysis of electromagnetic waves on open or closed three-dimensional, perfectly conducting or resistive surfaces. The primary emphasis in analysis is upon computation of radar cross section under plane-wave illumination. However, the program also provides for excitation via local ports for computation of gain patterns and input impedances of antennas.

The electric-field-integral form of Maxwell's equations is solved by use of a local triangle couple basis and testing functions with a resultant system impedance matrix. The emphasis in analysis is not only upon routine predictions of radar-cross-section patterns, but also on phenomenological diagnostics: bistatic imaging, currents, and both scattered and total near electric fields. The output data on images, currents, and near fields are in a form suitable for animation.

MOM3D computes the full backscatter and bistatic radar-cross-section polarization scattering matrix (amplitude and phase), body currents, and scattered and total near fields under plane-wave illumination. MOM3D also incorporates a new bistatic k-space imaging algorithm for computing down-range/cross-range diagnostic images by use of only matrix inversion in each case.

MOM3D has been made efficient, with respect to memory and central-processing-unit time, by use of symmetric matrices, symmetric geometry, and partitioned fixed and variable geometries suitable for design-iteration studies. MOM3D can be run interactively or in batch mode on IBM 486 and compatible personal computers, UNIX work stations, or larger computers. A 486 personal computer that has 16 megabytes of memory has the potential to solve the equations for a 30-square-wavelength symmetric configuration, which involves 3,000 unknowns. The geometry of a given problem is described by use of a triangular-mesh input in the form of a list of vertex points and a triangle-join-connection list.

MOM3D is written in FORTRAN 77. Two machine versions are available from COSMIC. One of them is the UNIX version (LAR-15074), which is designed to be executed on SGI-series computers running IRIX and, with modifications that are described in the documentation, has been implemented successfully on a Sun4-series computer running SunOS. The other version is the IBM PC version (LAR-15130), which has been implemented successfully on a IBM-PC-compatible computer running MS-DOS and version 5.1-EM32 of Lahey FORTRAN. The amount of random-access memory needed for MOM3D varies with the size of the problem being solved. Sample input and output files are provided for each version. The UNIX and PC versions include an SGI executable code and an MS-DOS executable code, respectively. The UNIX version also includes electronic documentation in PostScript format, while the PC version includes electronic documentation in WordPerfect format.

The standard distribution medium for the UNIX version is a 0.25-in. (6.35-mm) streaming-magnetic-IRIX-tape cartridge in UNIX tar format. It is also available on a 0.25-in. (6.35-mm) streaming-magnetic-tape cartridge (SUN QIC-24) in UNIX tar format. The standard distribution medium for the PC version (LAR-15130) is a set of four 5.25-in. (13.335-cm), 360K MS-DOS-format diskettes. The contents of the diskettes are compressed by use of the PKWARE archiving software tools. The utility software to unarchive the files, PKUNZIP.EXE, is included. The UNIX version of MOM3D is also available as part of a package, COS-10048, that includes EM-ANIMATE, an IRIS program capable of displaying and animating MOM3D results. This program was developed in 1992.

This program was written by John F. Shaeffer of Denmar, Inc., for **Langley Research Center**. *Further information is contained in a TSP [see page 1].*
LAR-15074/15130

Computing Interactions of Free-Space Radiation With Matter

A user-friendly program provides dosimetric information for use in design.

The High Charge and Energy Transport (HZETRN) computer program is a computationally efficient, user-friendly package of software that addresses the problem of transport of,

and shielding against, radiation in free space. HZETRN is designed as a "black box" for design engineers who are not concerned with the physics of the underlying atomic and nuclear radiation processes in a free-space environment, but rather are primarily interested in obtaining fast and accurate dosimetric information for the design and construction of modules and devices for use in free space. Computational efficiency is achieved by a unique algorithm based on a deterministic approach to the solution of the Boltzmann equation rather than the computationally intensive statistical Monte Carlo method.

HZETRN is based on a space-marching formulation of the Boltzmann transport equation with a straight-ahead approximation. Furthermore, due to the long range of the Coulomb force and the large percentage of volume of material occupied by electrons, the interaction of radiation with electrons is treated as a continuous slowing process. In developing the formalism for HZETRN, the nature of the transport coefficients (atomic and nuclear stopping power, nuclear scattering and absorption cross sections, and nuclear fragmentation cross section) had to be considered. Atomic (electronic) stopping powers with energies above a few MeV were calculated by use of Bethe's theory including Bragg's rule, Ziegler's shell corrections, and effective charge. At sufficiently low energies, at which nuclear stopping power becomes important, the nuclear stopping power theory of Lindhard, Scharff, and Schiott as modified by Ziegler was used. Nuclear absorption cross sections were obtained by use of fits to quantum calculations, and total cross sections were obtained by use of a Ramsauer formalism. Nuclear fragmentation cross sections were calculated from a semiempirical mathematical model of fragmentation by abrasion and ablation.

HZETRN includes a numerical algorithm for interpolation, extrapolation, and integration and for generation of grids. This algorithm also controls local truncation and the propagation error. Consideration is given to minimization of the number of energy grids to maintain efficiency. Since fluxes of cosmic rays vary most rapidly at energies below 1 A GeV, HZETRN has been made to select a uniform logarithmic scale for the range grid, and the corresponding energy grid is calculated on the basis of this selection.

A design engineer using HZETRN can quickly obtain the integral flux, absorbed dose, or dose equivalent in tissue (water) in units of either centiGray (cGy) or

centiSievert (cSv). These calculations are based on ICRP26 and ICRP60 quality factors behind various thicknesses of aluminum shield exposed to GCR at seven provided solar minima or maxima taken from 1958 to present. The flux and dosimetric results are presented for 59 individual particle field isotopes. Cumulative results are presented for six charge groups (the values of Z, the atomic number, being 0, 1, 2, 3-10, 11-20, and 21-28) or as total dose for the entire transported particle field at various thicknesses. Furthermore, flux and absorbed doses are calculated as functions of linear energy transfer for biological studies. Typical run time for the case of an aluminum shield of 20 grams per square centimeter and a tissue (water) target of 5 grams per square centimeter is a few minutes on a VAX 4000 computer.

HZETRN is written in FORTRAN for DEC VAX-series computers running VMS version 5.5. The amount of random-access memory needed depends on the size of the problem being solved. Documentation for HZETRN consists of six pages that detail the operation of the program, setup of input files, and how to interpret output. An electronic copy of the documentation is available in ASCII format on the distribution medium. The standard medium for distribution of this software is a 1,600 bit/in. (~630-bit/cm), 9-track magnetic tape in DEC VAX BACKUP format. It is also available on a TK50 tape cartridge in DEC VAX BACKUP format. HZETRN was developed in 1992.

This program was written by J. W. Wilson, F. A. Cucinotta, J. L. Shinn, and L. W. Townsend of **Langley Research Center**; *F. F. Badavi and R. K. Tripathi of Christopher Newport University; R. Silberberg and C. H. Tsao of the Naval Research Laboratory; and G. D. Badhwar of Johnson Space Center. Further information is contained in a TSP [see page 1]. LAR-15225*

Mechanics

Computing Effects of Hypervelocity Impacts on a Spacecraft

MLITEMP estimates damage and thermal effects.

The MLITEMP computer program is a design software tool that utilizes empirical equations to predict the damage and

the thermal effects of impacts of hypervelocity particles on spacecraft. (One of the thermal effects predicted by MLITEMP is the amount of condensate formed.) A Whipple style of spacecraft wall (which consists of multiple layers of insulation and a "bumper" layer in addition to a pressure wall) is assumed. Three different techniques for empirically predicting the damage caused by hypervelocity impacts are used in MLITEMP: an "inverse-R" prediction technique, a polynomial-function prediction technique, and a nondimensional-parameter prediction technique.

The "inverse-R" prediction-technique uses a prediction equation of very general form that can be applied in the same manner to all problems. Thus, the user is not required to develop a suitable form for the prediction, and additional independent variables can be incorporated easily as needed. This method is designed to use a data base that can be updated continuously as new experimental data become available. The method automatically takes advantage of the most appropriate data in the data base for a given set of independent variables. The measured data points that are used for prediction can be considered to "radiate" information to an interpolation point. The farther the data point is from the interpolation point, the weaker the "radiation."

The polynomial-function prediction technique is based on the concepts associated with the finite-element method (FEM). In the FEM, polynomials of relatively low order are used to interpolate a function of interest over a small portion (a finite element) of the domain wherein the function is active. The coefficients of the polynomial are derived from known values of the function of interest at points called nodes on the boundary of the element. For this application, the nodal values of the function of interest are measured experimentally and are thus known quantities. This technique involves selecting a sufficient number of experimental data (nodal) points and then determining the coefficients of the polynomial from these data.

The nondimensional-parameter prediction technique has been found to be the best method to represent empirical functions in many applications. The coefficients of the functions are determined by use of an optimization routine to adjust the values of the coefficients so as to maximize the coefficient of determination of each of the functions. The

nondimensional functions are adjusted to match the experimental results as closely as possible in a least-squares sense. This approach to evaluation of coefficients is suitable for any form of prediction function — linear or nonlinear.

The thermal behavior of the pressure wall, the multiple insulating layers, and the bumper layer are all explicitly modeled by use of an axisymmetric finite-difference analysis technique. Steady-state thermal conditions are also modeled.

The condensate-prediction subprogram is used to determine the height of condensate for a given distribution of temperature on the surface of the spacecraft. Two sets of conservation equations are solved: one for the condensate layer and one for the vapor layer, with appropriate interface conditions. The boundary-layer theory breaks down near the center of the circular region, so that the full Navier–Stokes (conservation-of-momentum) equations must be considered.

MLITEMP is written in BASIC for IBM PC-series and compatible computers running MS-DOS. This package includes sample executable codes, which were compiled under the Microsoft BASIC Professional Development System (BPDS). Although written for completion under Microsoft BPDS, the programs of MLITEMP that do not use the menu, window, and mouse toolbox of BPDS can be modified and recompiled using Microsoft Quick-Basic 4.5. Earlier versions of Microsoft QuickBasic may not compile the MLITEMP source code properly. The minimum requirements for the proper execution of MLITEMP include an 80286 processor, a math coprocessor, and an EGA or VGA graphics card and monitor. The standard distribution medium for this program is a set of three 5.25-in. (13.34-cm), 360K MS-DOS-format diskettes. The contents of the diskettes are compressed by use of the PKWARE archiving software tools. The utility program to unarchive the files, PKUNZIP.EXE, is included. MLITEMP was developed in 1992.

This program was written by William K. Rule of Marshall Space Flight Center and V. Gridharan of The University of Alabama. Further information is contained in a TSP [see page 1].

Inquiries concerning rights for the commercial use of this invention should be addressed to the Patent Counsel, Marshall Space Flight Center [see page 1]. Refer to MFS-26239

Computing Trimmed, Mean-Camber Surfaces at Minimum Drag

This program utilizes a vortex lattice method mathematical model.

The VLMD computer program determines the subsonic mean-camber surfaces of trimmed noncoplanar planforms with minimum vortex drag at a specified lift coefficient. Up to two planforms can be designed together. The method used is that of the subsonic vortex lattice method of chord loading specification, ranging from rectangular to triangular, left to be specified by the user.

In VLMD, a Trefftz-plane analysis is used to determine the optimum span loading for minimum drag. The program then solves for the mean-camber surface of the wing associated with this loading. Pitching-moment or root-bending-moment constraints can be employed at the design lift coefficient. Sensitivity studies of vortex-lattice arrangements have been made with this program and comparisons with other theories show generally good agreement. The program is very versatile and has been applied to isolated wings, wing/canard configurations, a tandem wing, and a wing/winglet configuration.

The design problem solved with this code is essentially one of optimization. A subsonic vortex lattice is used to determine the span load distribution(s) on bent lifting line(s) in the Trefftz plane. A Lagrange multiplier technique is used to determine the required loading, which is used to calculate the mean-camber slopes, which, in turn, are then integrated to yield the local elevation surface. The problem of determining the necessary circulation matrix is simplified by having the chordwise shape of the bound circulation remain unchanged across each span, though the chordwise shape may vary from one planform to another. The circulation matrix is obtained by calculating the spanwise scaling of the chordwise shapes. A chordwise summation of the lift and pitching moment is utilized in the Trefftz-plane solution, on the assumption that the trailing wake does not roll up and that the general configuration includes specifiable chord-loading shapes.

VLMD is written in FORTRAN for IBM PC-series and compatible computers running MS-DOS. This program requires

360K of random-access memory for execution. The Ryan McFarland FORTRAN compiler and PLINK86 are necessary to recompile the source code; however, a sample executable code is provided on the distribution medium. The standard medium for distribution of VLMD is a 5.25-in. (13.335-cm), 360K MS-DOS-format diskette. VLMD was originally developed for use on CDC 6000-series computers in 1976. It was originally ported to the IBM PC in 1986, and, after minor modifications, the IBM PC version was released in 1993.

This program was written by John E. Lamar and William T. Hodges of Langley Research Center. Further information is contained in a TSP [see page 1].
LAR-15160

Machinery

Program for Analysis of Axial-Flow Compressors

Computations based on simplifying assumptions quickly yield approximate results for design studies.

CSPAN (Compressor SPanline ANalysis) is a FORTRAN 77 computer program that assists in the design of axial-flow compressors. This program enables the design engineer to study the relationships among the number of stages, the flow-path radii, the gas velocities, the flow angles, and the resultant variation of compressor efficiency. It also rapidly provides conceptual designs for preliminary design studies of air-breathing engines.

The program is based on the assumption of isentropic simple radial equilibrium. Maximum rotor-tip and stator-hub loadings, maximum turning at the rotor hub, and maximum stator-hub mach number are specified as design constraints. Many advanced compressor designs require reductions in tip radii to provide adequate blade heights at the exits. Therefore, this program includes an input for direct specification of the change of tip radius across each row of blades. The hub-ramp-angle limit is a constraint that is included to avoid excessive wall slope. The mass-flow rate can be specified by the user and used to calculate the inlet-tip axial velocity, which

can optionally be specified directly by the user. Two built-in loss correlations are available to the user: one for stage polytropic efficiency, and the other for the blade-element pressure-loss coefficient. The velocity diagrams and stage-by-stage performance are calculated along with overall performance.

CSPAN is written in FORTRAN 77, and requires a compiler which supports NAMELIST input. It was originally written on an IBM mainframe running VM/CMS. This version has also been successfully implemented on a DEC VAX series computer running VMS. The standard distribution medium for CSPAN is a 9-track 1600-bit/in. (630-bit/cm) magnetic tape in DEC VAX FILES-11 format. Upon request, it is also available on a TK50 tape cartridge in DEC VAX BACKUP format or on a 5.25-in. (13.335-cm) 360K MS-DOS format diskette. CSPAN, which was developed in 1992, is an update of the program N34 previously available from COSMIC as part of LEW-10765.

This program was written by Arthur J. Glassman of the University of Toledo for **Lewis Research Center**. *Further information is contained in a TSP [see page 1].* LEW-15609

Mathematics and Information Sciences

Program Helps Decompose Complex Design Systems

DeMAID groups modular subsystems on the basis of interactions among them.

Many engineering systems are large and multidisciplinary. Before the design of such new complex systems as large platforms in outer space can begin, the possible interactions among subsystems and their parts must be determined. Once this is done, the proposed system can be decomposed to identify its hierarchical structure.

The DeMAID (A Design Manager's Aid for Intelligent Decomposition) computer program is a knowledge-based software system for ordering the sequence of modules and identifying a possible mul-

tilevel structure for the design problem. DeMAID displays the modules in the format of an $N \times N$ matrix (called a design structure matrix). As used here, "module" denotes any process that requires input and generates an output. A module could also be a process (e.g., an initialization process) that generates an output but does not require an input. Although DeMAID requires an investment of time to generate and refine the list of modules for input, it could save a considerable amount of money and time in the total design process, particularly in a new design problem in which the order of the modules has not been defined.

The decomposition of a complex design system into subsystems depends on the judgment of the design manager. DeMAID reorders and groups the modules on the basis of the links (interactions) among the modules, helping the design manager make decomposition decisions early in the design cycle. The modules are grouped into circuits (the subsystems) and displayed in an $N \times N$-matrix format. Feedback links, which indicate an iterative process, are minimized and occur only within a subsystem. Since there are no feedback links among the circuits, the circuits can be displayed in a multilevel format. Thus, a large amount of information is reduced to one or two displays that are stored for later retrieval and modification. The design manager and leaders of the design teams then have a visual display of the design problem and the intricate interactions among the different modules.

The design manager could save a substantial amount of time if circuits on the same level of the multilevel structure are executed in parallel. DeMAID estimates the time saved on the basis of the number of available processors. In addition to decomposing the system into subsystems, DeMAID examines the dependencies of a problem with independent variables and dependent functions. A dependency matrix is created to show the relationship.

DeMAID is based on knowledge-base techniques to provide flexibility and ease in adding new capabilities. Although DeMAID was originally written for design problems, it has proven to be applicable to any problem containing modules (processes) that take inputs and generate outputs. For example, one group is applying DeMAID to gain understanding of the flow of data associated with a very large computer program. In this

example, the modules are the subroutines of the program.

The design manager begins the design of a system by determining the level of modules that must be ordered. The level is the "granularity" of the problem. For example, the design manager may wish to examine disciplines (a coarse model), analysis programs, or the data level (a fine model). Once the system is divided into these modules, the input and output of each model is determined, creating a data file for input to the main program.

DeMAID is executed through a system of menus. The user can choose to plan, schedule, display the $N \times N$ matrix, display the multilevel organization, or examine the dependency matrix. The main program calls a subroutine that reads a rule file and a data file, asserts facts into the knowledge base, and executes the inference engine of the artificial-intelligence/expert-system program, CLIPS (C Language Integrated Production System).

To determine the effects of changes in the design process, DeMAID includes a "trace effects" feature. Two methods of tracing the effects of a change in the design process are available. The first method involves tracing forward through the outputs to determine the effects of an output with respect to a change in a particular input. The second method involves tracing backward to determine what modules must be re-executed if the output of a module must be recomputed.

DeMAID is available in three machine versions: a Macintosh version written in Symantec's Think C 3.01, a Sun version in C language, and an SGI IRIS version in C language. The Macintosh version requires system software 6.0.2 or later and CLIPS 6.0. The source code for the Macintosh version is not compilable under version 4.0 of Think C; however, a sample executable code is provided on the distribution media. QuickDraw is required for plotting. The Sun version requires GKS 4.1 graphics libraries, OpenWindows 3, and CLIPS 6.0. The SGI IRIS version requires CLIPS 6.0. The documentation for CLIPS 6.0 is not included in the documentation package for DeMAID; however, it is available from COSMIC separately as the documentation for MSC-21208. The standard distribution medium for the Macintosh version of DeMAID is a set of four 3.5-in. (8.9-cm), 800K Macintosh-format diskettes. The standard distribution medium

for the Sun version of DeMAID is a 0.25-in. (6.35-mm) streaming-magnetic-tape cartridge (QIC-24) in UNIX tar format. The standard distribution medium for the IRIS version is a 0.25-in. (6.35-mm) IRIX-compatible streaming-magnetic-tape cartridge in UNIX tar format. All versions include sample input. DeMAID was originally developed for use on VAX VMS computers in 1989. The Macintosh version of DeMAID was released in 1991 and updated in 1992. The Sun version of DeMAID was released in 1992 and updated in 1993. The SGI IRIS version was released in 1993.

This program was written by James L. Rogers, Jr., of Langley Research Center and Laura E. Hall of Unisys Corp. Further information is contained in a TSP [see page 1].
LAR-15099

Program Implements Variable-Sampling Procedures

Tedious procedures are automated.

The MIL-STD-414 Variable Sampling Procedures (M414) computer program has been developed to automate the calculations and the acceptance/rejection procedures of MIL-STD-414, "Sampling Procedures and Tables for Inspection by Variables for Percent Defective." Prior to the development of M414, the use of MIL-STD-414 could be cumbersome and confusing to a nonstatistician: MIL-STD-414 requires some calculations plus extensive referral to the tables in making a decision to accept or reject a lot. The process of calculation and reference to the tables is tedious and confusing and can, therefore, result in errors. These difficulties have probably discouraged the use of MIL-STD-414 and led to mistakes in applying it.

M414 automates the entire calculation-and-decision process by use of computational algorithms that determine threshold acceptability values for lots. M414 is menu-driven and user-friendly. The use of M414 can reduce the burden of manual operations, thus promoting variable-sampling practice in industry in lieu of "go/no-go" inspection.

M414 is written in BASIC for IBM PC-series and compatible computers running MS-DOS. The program requires 512K of random-access memory, an 80

× 87 math coprocessor, and a CGA monitor for execution. The Microway 87SFL Math Function Software Library (Kingston, MA; 508-746-7341) and Microsoft QuickBasic v2.0 are needed to compile the source code. The standard distribution medium is one 5.25-in. (13.335-cm) diskette in MS-DOS format. Documentation is included in the price of the program. M414 was developed in 1993.

This program was written by Zhaofeng Huang of Rockwell International Corp. for Marshall Space Flight Center. Further information is contained in a TSP [see page 1].
MFS-30004

Program for Editing Graphical Displays of Schedules

This program provides WYSIWYG editing capabilities.

XOPPS is a window-based software tool for graphics that provides easy and fast "what you see is what you get" (WYSIWYG) on-screen editing capabilities. It provides an area, analogous to a canvas, on which it displays a full image of a schedule being edited. The canvas contains a header area (for text) and a schedule area (for plotting graphical representations of milestone objects in a flexible time line).

XOPPS is object-oriented, but it is unique in its capability for creation of objects that have date attributes. Each object on the screen can be treated as a unit for moving, editing, and other operations. There is a mouse interface for simple control of location of a pointer. The user can position objects to pixel resolution, but objects with which dates are associated are positioned automatically in their correct time-line positions in the schedule area.

The schedule contains horizontal lines across a page, with capabilities for multiple pages and for editing the number of lines per page and the line grid. The text on a line can be edited, and a line can be moved in which case all objects on the line move with the line. The time-line display can be edited to plot any time period in a variety of formats from fiscal year to calendar year and from days to years. Text objects and image objects (rasterfiles and icons) can be created for placement anywhere on the page.

Milestone event objects, each with a single associated date (and optional text and milestone symbol) and activity objects with beginning and ending dates (and an optional completion date) include unique editing panels for entering data. A representation for schedule slips is also provided with the capability to automatically convert a milestone event to a slip. A milestone schedule can be saved to an ASCII file on another computer to be read by XOPPS. The program can also print a schedule to a PostScript file. Dependencies between objects can also be displayed on the chart by use of precedence lines.

This program is not intended to replace a commercial scheduling-and-project-management program. Because XOPPS includes an ASCII file interface, it can be used in conjunction with a project-management software tool to produce schedules with an appearance of quality.

XOPPS is written in C language and runs under X/Motif on a Sun Workstation with SunOS 4.0 or higher. The memory required for use of XOPPS consists of 375KB of main memory and 1.5MB of free disk space. XOPPS was developed in 1992, based on the Sunview version OPPS developed in 1990. XOPPS is a copyrighted work with all copyright vested in NASA.

SunOS and Sunview are trademarks of Sun Microsystems, Inc. Sun Workstation is a registered trademark of Sun Microsystems, Inc. X/Motif is a trademark of Open Software Foundation (OSF). PostScript is a trademark of Adobe Systems Incorporated.

This program was written by Cassie L. Mulnix and Kevin Miller of Caltech for NASA's Jet Propulsion Laboratory. Further information is contained in a TSP [see page 1].
NPO-19348

Program Helps Standardize Documentation of Software

IDMS helps a program manager in tailoring a documentation standard to a project.

The Intelligent Documentation Management System (IDMS) computer program was developed to assist project managers in implementing the information system documentation standard known

as NASA-STD-2100-91 (NASA STD, COS-10300) of NASA's Software Management and Assurance Program. The standard consists of data-item descriptions (DID's), or templates, each of which governs a particular component of software documentation. For example, one DID governs the user's guide, another the quality-assurance requirements, and so on. The DID's are hierarchically interrelated to one another, forming a DID hierarchy, or inverted tree structure.

It is up to the project manager (PM) of a given project to determine which of the DID's apply to a particular project and which are not applicable. Also, if any one of the DID's grows too large to be comfortably embedded as an in-line section of a parent document, the PM may roll it out as a separate volume, but must maintain traceability between this volume and its parent document.

IDMS functions as a decision-support system that automates the process of tailoring the DID hierarchy. IDMS uses an embedded expert-system program

called the Project Manager Advisor (PMA) to advise the PM on how the standard should be tailored on the basis of such qualitative project criteria as level of risk, security and/or privacy aspects, and the like. IDMS then provides the PM with the capability to custom-tailor the DID hierarchy for a particular project, to assign and manage writing responsibility for individual DID's to members of the project team, to maintain configuration management of the pieces of documentation in process, and to compile these pieces of documentation periodically into draft and/or final versions of a complete set of documentation. IDMS has been designed to be data-independent, such that it can be adapted easily to virtually any documentation standard that involves hierarchically related DID templates.

IDMS is written in C language for IBM PC-series and compatible computers running MS-DOS. The program requires at least 5 Mb of disk space and a VGA or EGA graphics display. The source code can be compiled properly only with

the inclusion of files from the Vermont Views software package (available from Vermont Creative Software, Richford, VT, 802/848-7731); however, an executable code is provided on the distribution medium. The executable code requires at least 640K of random-access memory and MS-DOS v3.1 or higher. Printing of IDMS-produced documents requires WordPerfect v5.0, or higher. The standard distribution medium for this program is a set of four 5.25-in. (13.34-cm), 1.2-Mb diskettes in MS-DOS format. The program price includes a copy of the NASA STD package (COS-10300) diskette as well as the IDMS documentation. IDMS was developed in 1992.

This program was written by G. Howe of Systems Research and Applications Corp. for Lewis Research Center. Further information is contained in a TSP [see page 1].
LEW-15589
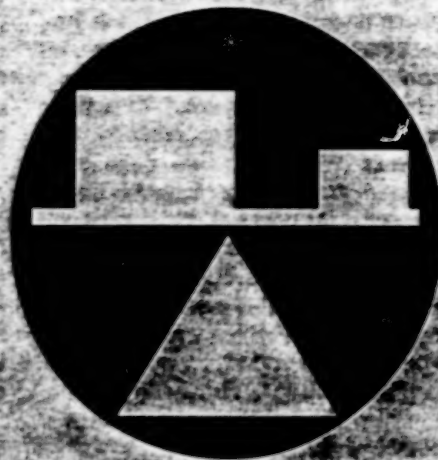
Mechanics

Hardware, Techniques, and Processes

Improved Selection of Structural-Load Safety Factors

A more rational approach offers potential for optimization of design.

Marshall Space Flight Center, Alabama

An improvement in the deterministic method of selection of structural-load safety factors should make it possible to design structures that are more nearly optimum with respect to competing demands for both reliability and attributes that detract from reliability (principally lighter weight, smaller size, and lower cost). Safety factors are the factors by which structures and components thereof are strengthened in design to withstand loads greater than nominal design loads, the purpose being to ensure against failures under initially unknown but reasonably foreseeable overloads. In the deterministic method (which is really partly subjective, despite its name), safety factors are selected arbitrarily or on the basis of experience. For example, the conventional safety factor for tensile strength of a component is the ratio between the ultimate tensile stress that the material can resist and the stress applied by the nominal maximum design load. Normally, the maximum design load would not be allowed to exceed the tensile yield stress, so that the lower limiting value of the conventional deterministic safety factor (called the "lean" safety factor) is the ratio between the ultimate and yield tensile stresses.

In the deterministic method as practiced until now, strengths of materials and load-induced stresses have been treated as single-valued parameters, while universal safety factors that are not equally realistic for all structural materials have been used to account for uncertainties. This practice has led to overdesign of some noncritical components; on occasion, it has led to underdesign of critical components and consequent failures. In the improved deterministic method, the selection of safety factors is guided partly by statistical data on deviations of loads, stresses, and strengths of materials from expected values. Instead of considering the single safety factor of the conventional deterministic method, one considers three safety factors, which are specified independently with respect to loads, stresses, and materials respectively. These safety factors are combined into a single safety index, which is then used to support design trades among them and to compare the safety of different
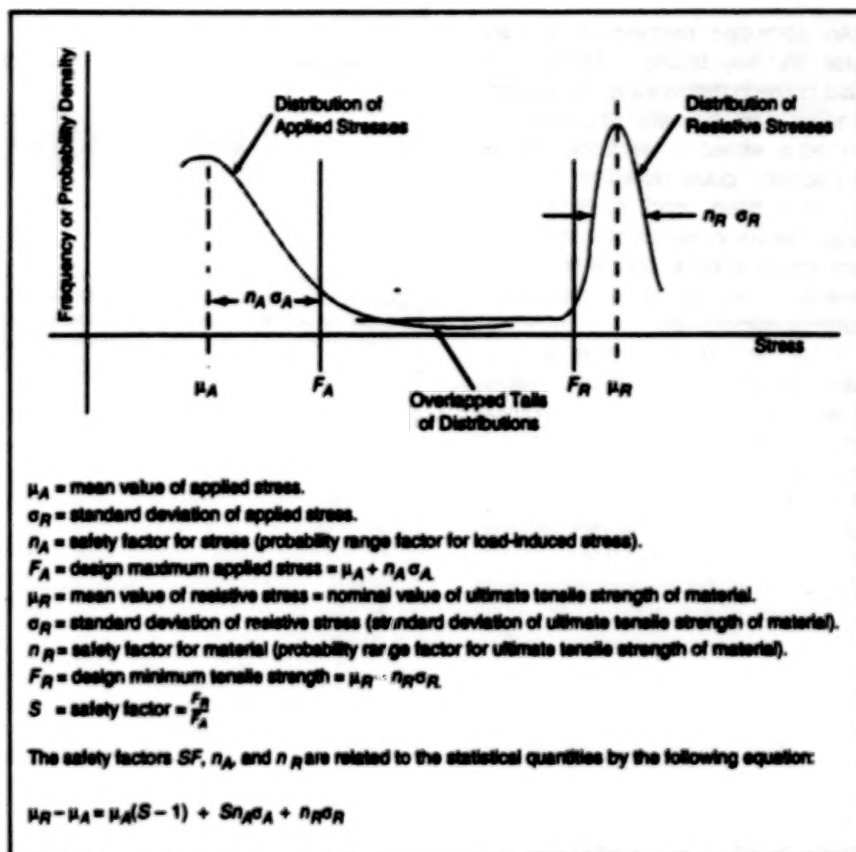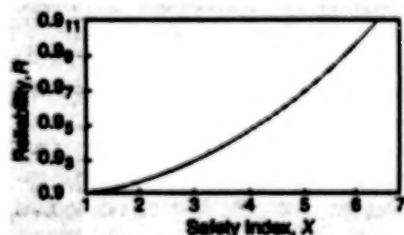
stressed regions in the same structure or in different structures.

By incorporating the use of some statistical data, the improved deterministic approach involves some probabilistic elements, but not the complexity of a fully probabilistic approach. Figure 1 presents an example of a simple component under uniaxial tensile stress to illustrate the statistical and probabilistic aspects of the improved approach and the relationships among the various safety factors. The deterministic safety index is computed from the safety factors and the statistical parameters indicated in Figure 1; the deterministic safety index summarizes the information on the anticipated reliability of the stressed component in the following way: the probability that the applied stress will not exceed the ultimate tensile stress that the material can resist is a function (typically, a cumulative normal distribution function) of the safety index (see Figure 2).

μ_A = mean value of applied stress.
σ_R = standard deviation of applied stress.
n_A = safety factor for stress (probability range factor for load-induced stress).
F_A = design maximum applied stress = $\mu_A + n_A \sigma_A$.
μ_R = mean value of resistive stress = nominal value of ultimate tensile strength of material.
σ_R = standard deviation of resistive stress (standard deviation of ultimate tensile strength of material).
n_R = safety factor for material (probability range factor for ultimate tensile strength of material).
F_R = design minimum tensile strength = $\mu_R - n_R \sigma_R$.
S = safety factor = $\frac{F_R}{F_A}$

The safety factors SF, n_A, and n_R are related to the statistical quantities by the following equation:

$$\mu_R - \mu_A = \mu_A(S-1) + Sn_A\sigma_A + n_R\sigma_R$$

Figure 1. A **Margin of Safety** can be considered to lie in the middle region of overlap of the tails of the statistical distributions of the applied and resistive stresses.

Notes:
1. Safety Index =

$$Z = \frac{(S-1) + S(n_A C_A) + (n_R C_R)\mu_R/\mu_A}{[C_A^2 + (C_R \mu_R/\mu_A)^2]^{\frac{1}{2}}}$$

where $C_A = \frac{\sigma_A}{\mu_A}$ and $C_R = \frac{\sigma_R}{\mu_R}$.

2. $R = \Phi(Z)$ is the cumulative normal distribution function.

Figure 2. The **Reliability of a Component** (in terms of the probability that the stress caused by an applied load will not exceed its strength) is a cumulative probability density function of the safety index.

Detecting Structural Failures via Acoustic Impulse Responses

Adaptive lattice filtering of echoes yields data on
sizes and locations of failures.

NASA's Jet Propulsion Laboratory,
Pasadena, California

An advanced method of acoustic pulse reflectivity testing is being developed for use in determining the sizes and locations of failures within structures. The method is related to electronic, optical, and acoustic pulse reflectivity methods that have been used successfully to detect breaks in electrical transmission lines, detect faults in optical fibers, and determine mechanical properties of materials, respectively.

In this method as in other acoustic pulse methods, the structure is vibrationally excited with an acoustic pulse (a "ping") at one location and the acoustic response is measured at the same or a different location (see Figure 1). The measured acoustic response is digitized, then processed by a finite-impulse-response (FIR) filtering algorithm that is unique to this method and that is based on the acoustic-wave-propagation and -reflection properties of the structure.

One important feature of the underlying wave-propagation and -reflection theory is that the cross-sectional areas of structural elements can be computed directly in terms of the reflection coefficients of an optimal (adaptive) FIR Wiener filter realized in lattice form. This is fortunate in that many practical on-line techniques for estimating the parameters of optimal Wiener FIR filters are already available. This leads to the present elegant method for detecting and localizing structural failures by using recursive, on-line techniques of estimation. This method offers several advantages over older failure-detection methods: it does not require training, does not require prior knowledge of a mathematical model of the acoustic response of the structure, enables the detection and localization of multiple failures, and yields data on the extent of damage at each location.

Figure 1 illustrates schematically the application of the method to a simple bar, which was the structure that was mathematically modeled in the initial development of the method. First, the impulse response of the bar is measured. By use of the acoustic input/output measurement data, the optimal FIR inverse transfer function of the bar is computed. The bar is then represented as a series of M sections (M is constrained by the output-sampling period) and the reflection coefficient (proportional to the cross-sectional
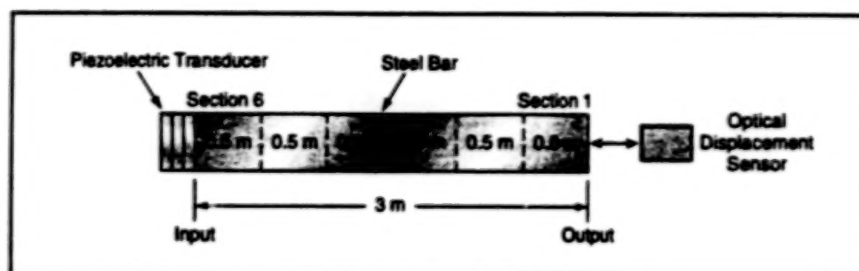

Figure 1. The Bar is Vibrationally Excited at one end by using the piezoelectric transducer to apply an acoustic pulse. The resulting lengthwise acoustic displacements are measured optically at the other end. For purposes of analysis of the response, the bar is arbitrarily divided into $M = 6$ sections; more or fewer than 6 could be used.
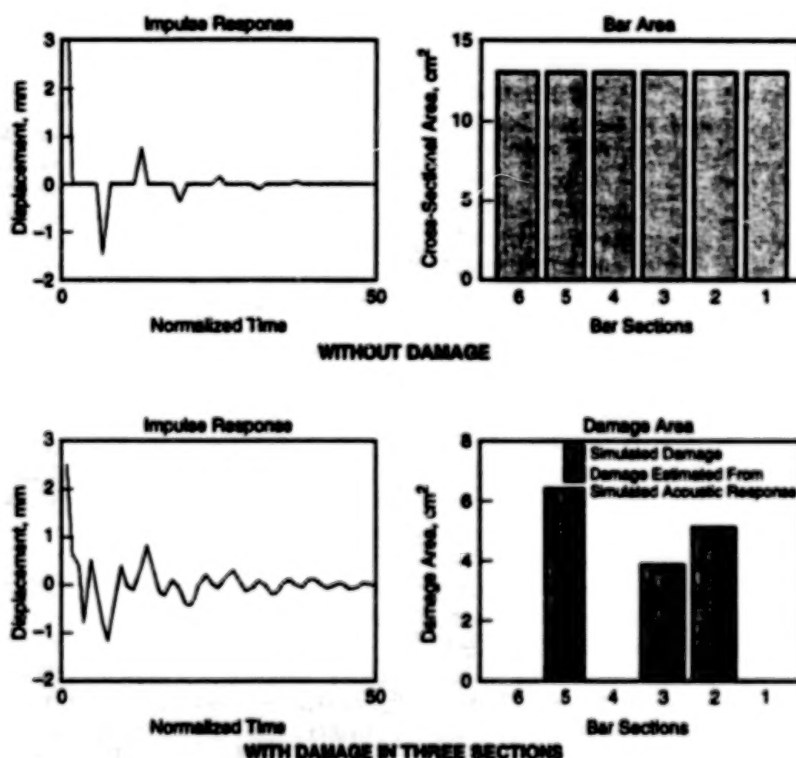

Figure 2. In a Computational Simulation of the Test Illustrated in Figure 1, the acoustic responses of the bar without and with damage in three sections were analyzed by the method described in the text. The analysis was successful in identifying the damaged sections and in estimating the extent of damage (reduction in cross-sectional area) in each damaged section.

area) of each section is calculated as in a lattice filter.

Ideally, the acoustic impulse response of the bar is measured repeatedly and used to update the reflection coefficients and/or cross-sectional areas at the M-1 locations of the boundaries between the M sections of the bar. When some damage occurs, the cross-sectional area at the damage location changes, resulting in a corresponding change in the reflection coefficient for that location. Thus, from the amount of change in, and iden-

tity of, the changed reflection coefficient, the extent and location of the damage are immediately known (see Figure 2). If damage occurs between two boundary locations, the reflection coefficients for both locations change.

Active Suppression of Vibrations on Aircraft Structures

Sensors, controllers, and actuators generate
compensatory vibrations.

Langley Research Center,
Hampton, Virginia
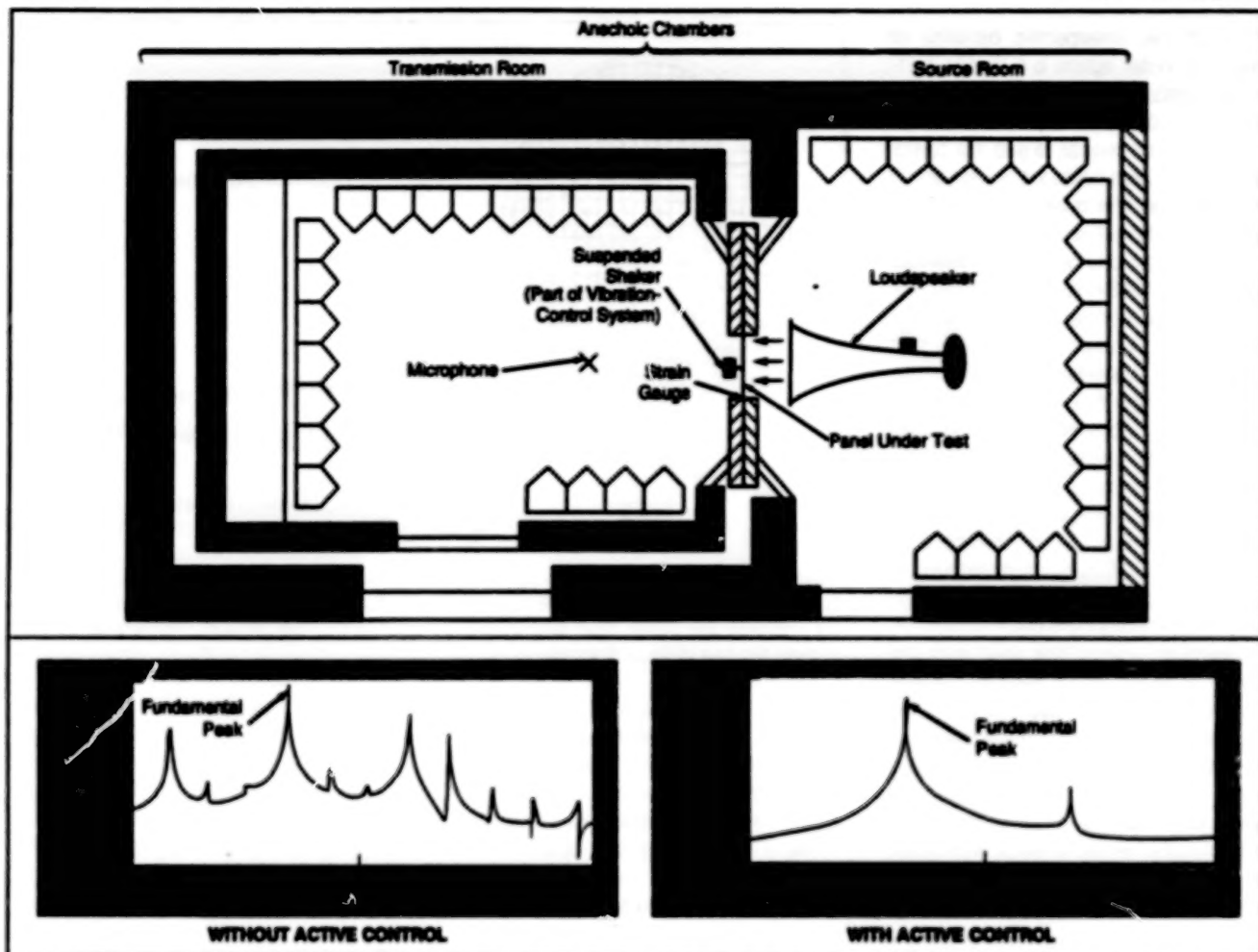
Vibrational Spectra were measured in an experiment with and without active control. Active control channeled energy from the fundamental to the harmonics and subharmonics via phase cancellation.

A method of active suppression of non-linear and nonstationary vibrations is being developed to reduce sonic fatigue and interior noise in high-speed aircraft. The structure of such an aircraft exhibits periodic, chaotic, and random vibrations when forced by high-intensity sound from jet engines, shock waves, turbulence, and separated flows. The developmental method of suppressing vibrations involves feedback control: Strain gauges or other sensors mounted in the paths of propagation of vibrations on the structure sense the vibrations; the outputs of the sensors are processed into a control signal that is applied to the actuator mounted on the structure, inducing compensatory forces.

The basic active-vibration-suppression concept describes a feedback technique applied to the control of nonlinear vibration. One approach is directed toward the control of periodic motion of a panel that responds nonlinearly in the sense that it

vibrates in harmonic and subharmonic modes, as well as in a fundamental mode, when acoustically excited at its resonant frequency (the frequency of the fundamental mode). The number, positions, and orientations of the sensors are chosen so that the array of sensors yields sufficient information on the directions of arrival, amplitudes, and phases of vibrations. In response, the control circuitry chooses amplitudes and phases of the compensatory vibrations such that the net amplitudes of the subharmonic and harmonic vibrations decrease, while the amplitude of the fundamental vibration increases. That is, the energy in the harmonics and subharmonics is channeled into the fundamental (see figure) with conservation of overall vibrational energy. Stated in yet another way, the state of vibration is converted from nonlinear to linear.

A second approach is directed toward suppression of vibrations that are both non-

stationary and nonlinear — e.g., vibrations forced by impingement of shocks or from exhaust from a nearby supersonic jet engine. It is the first time that nonlinear, nonstationary structure response has been successfully controlled. In this approach, opposing vibrations are generated at whichever frequency is momentarily that of the greatest vibrational spectral peak. In this approach, energy is not conserved: instead, energy is channeled from the greatest spectral peak to its harmonics, but with a net overall reduction in vibrational energy and in acoustic radiation from the structure.

This work was done by Lucio Maestrello of Langley Research Center. Further information is contained in a TSP [see page 1].

Inquiries concerning rights for the commercial use of this invention should be addressed to the Patent Counsel, Langley Research Center [see page 1]. Refer to LAR-15071.

Improved Tennis Racquets Have Tapered Strings

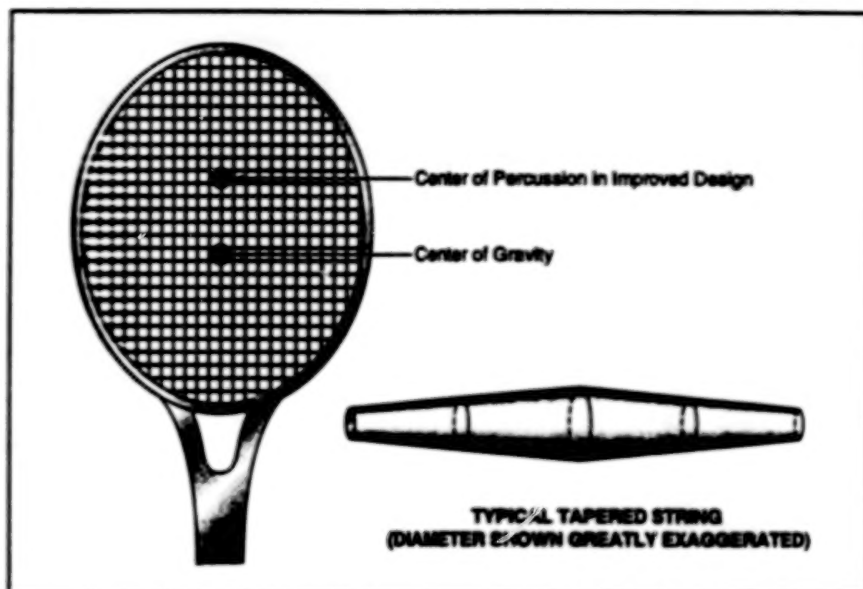The center of percussion is moved outward for better performance.

Marshall Space Flight Center, Alabama

One of the unexpected benefits of research in outer space is a design concept for a better performing tennis racquet. The essence of the concept is to taper the strings in such a way as to shift the center of percussion (also called the "sweet spot") toward the toe (the outer end of the racquet, farthest from the player's hand).

This concept originated more than 20 years ago in NASA studies of networks of strings for connecting platforms in outer space. Researchers found that changing the diameters of strings could radically change the stability of a network against vibration. This idea was inspired by an experiment in which a space-borne spider was coaxed to spin a good web and was observed to make its web with threads of nonuniform size.

The major difficulty in designing a high-performance tennis racquet arises from the difference between the position of maximum speed (the toe) and the position of optimum vibration (the sweet spot). In a typical older design, the sweet spot is at the geometric center of the strung area of the racquet. The impact of the ball on the sweet spot causes minimal kick or jar to be transmitted to the player's hand. However, the average player tends to strike the ball farther out toward the toe, and to obtain maximum power on serves, it is necessary to strike the ball as close as possible to the toe. Thus, performance can be improved by moving the sweet spot outward (see figure).

In addition to increasing power on serves, tapering the strings to move the sweet spot outward improves the player's control and the feel of the racquet in the player's hand. An important element of improved control is increased stability: the

Center of Percussion in Improved Design

Center of Gravity

**TYPICAL TAPERED STRING
(DIAMETER SHOWN GREATLY EXAGGERATED)**

Displacement of the Center of Percussion away from the center of gravity and toward the toe improves the power, feel, and control achievable with the racquet. The improvement involves the use of tapered strings.

racquet is less likely to twist in the player's hand on off-center shots. An important element of better feel is better absorption of vibrations; this is especially important for players who have chronic arm problems.

The optimization of the tapers of the strings for a given racquet design is based on the fundamental physics of vibrating strings. A computer performs the optimization numerically, by use of a genetic algorithm. As its name suggests, a genetic algorithm implements a mathematical evolutionary process that resembles biological evolution in some respects and that arrives at an optimized design (distribution of mass along each string) by following a sequence of random design changes and preserving those changes that improve performance.

The string material can be nylon, animal gut, or other naturally or artificially spun threads. The string can be attached to a conventional racquet frame. The required distribution of mass along each string can be achieved by spinning the string thicker or bundling different string materials along a central braid in the string.

This work was done by David A. Noever of Marshall Space Flight Center. Further information is contained in a TSP [see page 1].

Inquiries concerning rights for the commercial use of this invention should be addressed to the Patent Counsel, Marshall Space Flight Center [see page 1]. Refer to MFS-26922.

Constant-Flow Mixing Valve

A ball valve provides continuous variation of mixture without altering net flow.

Marshall Space Flight Center, Alabama

The ball valve shown partially in the figure mixes two liquid flows in any desired proportion. The valve admits the liquids at ports A and B and releases the combined liquids at the outlet (port C). Turning the ball adjusts the outlet flow continuously from 100 percent liquid A to 100 percent liquid B.

The orifices in the ball are contoured so that, together, they provide a constant rate

of flow at the outlet and a constant pressure drop through the valve of the ball.
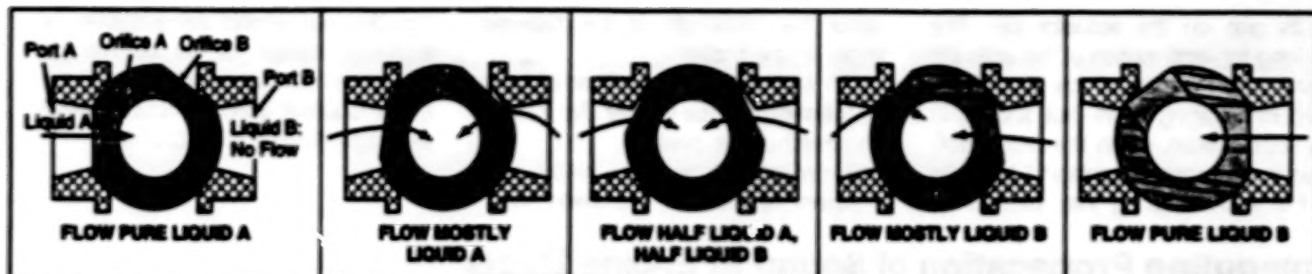
This work was done by Joe Sega and Neil A. M. Peters of Allied Signal, Inc., for Marshall Space Flight Center. Further information is contained in a TSP [see page 1].

Title to this invention has been waived under the provisions of the National Aeronautics and Space Act (42 U.S.C. 2457(f))

to Allied-Signal Aerospace Inc. Inquiries concerning licenses for its commercial development should be addressed to

Allied-Signal Aerospace Inc.
111 South 34th Street
P.O. Box 5217
Phoenix, AZ 85010
Refer to MFS-28864, volume and number of this NASA Tech Briefs issue, and the page number.

| FLOW PURE LIQUID A | FLOW MOSTLY LIQUID A | FLOW HALF LIQUID A, HALF LIQUID B | FLOW MOSTLY LIQUID B | FLOW PURE LIQUID B |

When Orifice A of the Ball is Coaxial with inlet port A, the outlet flow consists entirely of liquid A. As the ball is rotated clockwise, the part of orifice A exposed to port A decreases and the part of orifice B exposed to port B increases. The proportion of liquid B therefore increases, and that of liquid A decreases. The outlet flow (to port C) is not shown.

Probe-and-Socket Fasteners for Robotic Assembly

Self-alignment and simplicity of actuation make this mechanism amenable to robotic assembly.

Lyndon B. Johnson Space Center,
Houston, Texas
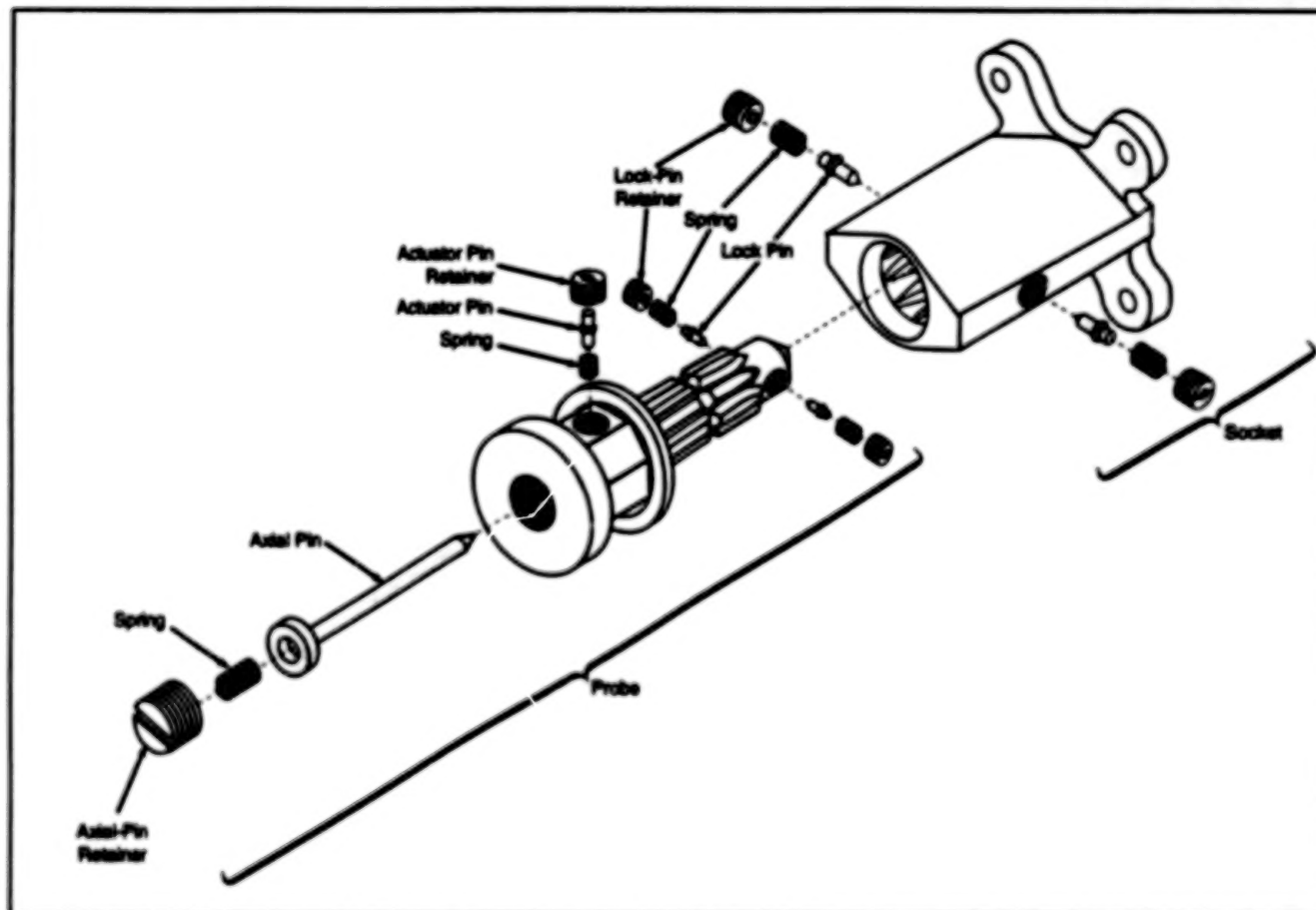
Lockpins in the Probe engage radial holes (not shown) in the socket. Depressing the actuator pin temporarily retracts the lockpins into the probe so that the probe can be inserted in the socket.

A probe-and-socket fastening mechanism is designed to be operated by a robot. The mechanism is intended to enable a robot to set up a workstation in a hostile environment, for example. The workstation can then be used by an astronaut, aquanaut, or other human, who would thus spend minimum time in the environment. The human can concentrate on performing quality work rather than on setting up equipment, with consequent reduction of risk.

The mechanism (see figure) includes (1) a socket, which would be mounted on a structure at the worksite, and (2) a probe, which would be mounted on a piece of equipment to be attached to the structure at the socket. The probe-and-socket mechanism is intended to be used in conjunction with a fixed target that would aid in the placement of the end effector of the robot during grasping, and with a handle or handles on the structure. The robot would move the probe near the socket

and depress the actuator pin in the probe. The inward motion of the actuator pin would cause rearward motion of the axial pin, thereby allowing two spring-loaded lockpins to retract into the probe. The robot would then begin to insert the probe into the socket.

Tapered grooves in the socket mesh with tapered ridges on the probe, thereby aligning the fastener parts and preventing binding. When the probe bottoms out in the socket, the robot releas-

es its grip on the actuator pin. The resulting forward motion of the axial pin pushes the lockpins of the probe outward into mating holes (not shown) in the socket. Also, when the probe bottoms in the socket, additional lockpins in the socket spring into detents at about the midlength of the tapered ridges on the probe.

This work was done by Karen Nyberg of **Johnson Space Center.** *No further documentation is available.*

This invention is owned by NASA, and a patent application has been filed.

Inquiries concerning nonexclusive or exclusive license for its commercial development should be addressed to the Patent Counsel, Johnson Space Center [see page 1]. Refer to MSC-22028.

Computing Propagation of Sound in Engine Ducts

An updated computer program is easier to use.　　　　　　　　*Marshall Space Flight Center, Alabama*

The Frequency Domain Propagation Model (FREDOM) computer program accounts for acoustic loads applied to components of engines. In particular, the program models the propagation of noise through fluids in ducts between components and through passages within components. It can be used not only to analyze hardware problems, but also for design purposes. FREDOM is an updated version of the FREQPL program, which was first developed in 1959.

These programs were devised specifically for use in analyzing the acoustic loads in rocket engines, where noise generated in pumps, combustion chambers, and duct bends can be so intense as to cause mechanical failures, and where resonances in ducts can amplify the effects of noise. The underlying physical and mathematical concepts implemented in these programs should also be applicable to acoustic propagation in other enclosed spaces; they might be useful, for example, in analyzing process plumbing and ducts in industrial buildings with a view toward reducing noise in work areas.

The older program, FREQPL, is basically a matrix solver with plotting capabilities. Before running FREQPL, the user had to do all the preparatory theoretical and computational work, which included (1) writing the often complicated wave equations, flow equations, and other equations as they apply to the system to be analyzed, (2) putting the equations into matrix-vector form, and (3) entering the matrix elements into the computer by responding to program prompts one element at a time. This preparatory work required an engineer with a high level of sophistication in acoustics and detailed knowledge of the system, consumed much time, and was highly susceptible to theoretical and typing errors. Also, the matrix for FREQPL was set up to solve for a specific variable. Most of the time, results are needed at many locations (different variables) of the system. When using FREQPL, the
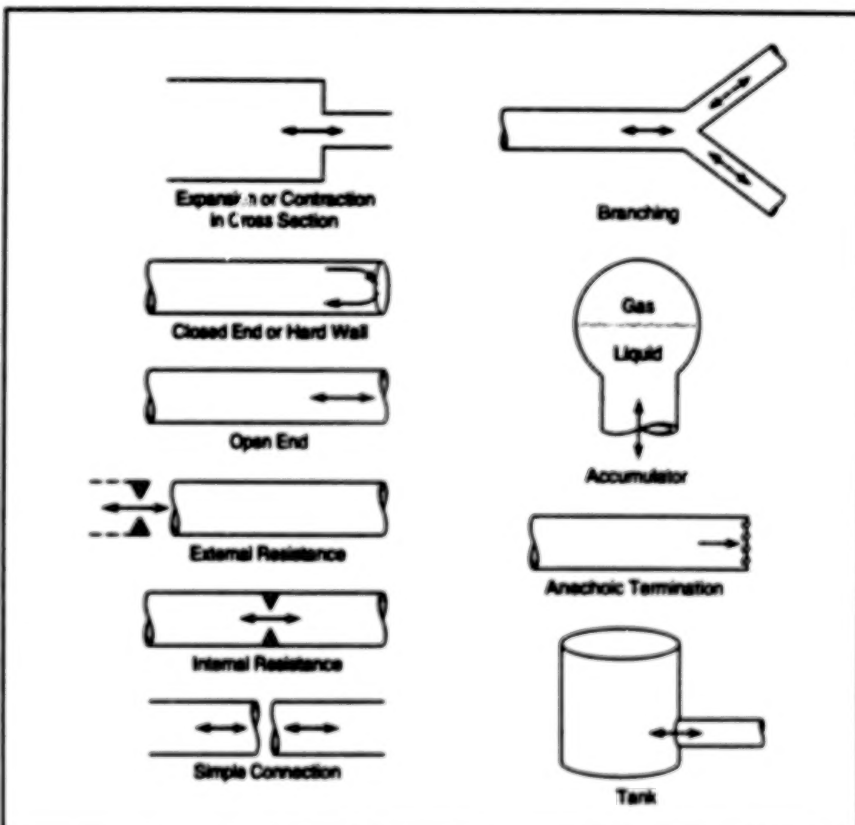

Figure 1. **Various Boundary Conditions** are treated automatically and routinely. FREDOM even provides for small changes in cross-sectional area of a duct due to the distensibility of the duct material.

preparatory work had to be repeated for each new variable.

FREDOM incorporates the matrix solver of FREQPL, but it also automates the preparatory theoretical work, thereby greatly reducing the probability of errors. FREDOM is a user-friendly and menu-driven code. It guides the user step by step through the analysis. The user needs only a good knowledge of acoustics.

The user provides data that describe the duct or passage geometry, connections, and properties of the fluid in the system via four input files. FREDOM also accounts for boundary conditions of the system automatically. The user merely states the type(s) of boundary condition(s) and the code incorporates the coefficients of the corresponding equa-

tion(s) into the coefficient matrix. Figure 1 shows the variety of boundary conditions handled by FREDOM. For example, if an accumulator is needed, the user need merely specify its location, the type of gas, and initial pressure and volume. For most boundary conditions, it suffices to specify locations only.

FREDOM then constructs the matrix from the data provided by the user — that is, FREDOM automatically does the equivalent of what the user would do in writing the acoustic equations for the system, but does it faster and more accurately. The matrix in FREDOM differs from that in FREQPL: the FREDOM matrix contains the coefficients of the system equations that have been manipulated to put all variables on the left side;

that is, the right sides of all the equations are set equal to zero. This matrix, along with the information used to create it, is stored in a "system file". Once the system file is obtained, any of the variables can be set on the right side of the equations for calculation of the applicable frequency response, without having to create a new matrix for each variable. Results can be plotted (see Figure 2) and/or tabulated.

FREDOM works directly in the frequency domain. In this respect, FREDOM offers a great advantage over a time-domain code, the output data of which would have to be postprocessed to convert them into the frequency domain. Postprocessing could add several hours to the overall computational process. In a large iterative analysis (for example, probabilistic analysis of a system), a frequency-domain approach takes several days less than does a time-domain approach.

This work was done by Silvie Saylor of Rockwell International Corp. for Marshall Space Flight Center. Further information is contained in a TSP [see page 1].
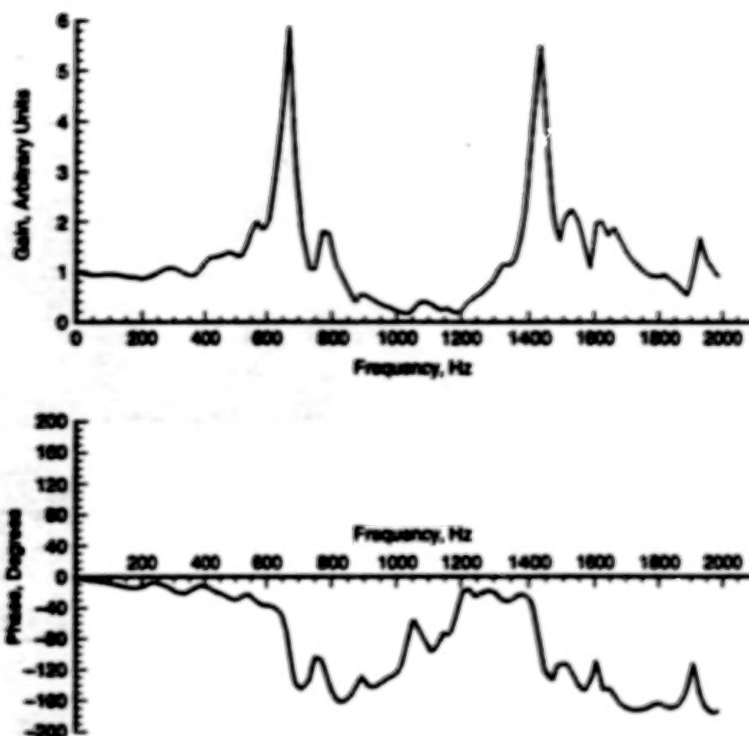MFS-29971

Figure 2. The Frequency Response plotted here is a transfer function that represents the acoustic response at one point along a duct to an acoustic excitation at another point along the duct. The peaks in the gain plot indicate the resonances of the duct. Also note a customary phase change in the accompanying phase plot at the resonance peaks.

Service Cart for Engines

This unit assists a lone worker in moving an engine.   *Langley Research Center, Hampton, Virginia*

A cart supports the rear-mounted air-cooled engine from a Volkswagen or Porsche automobile (see figure). With it, one person can remove, repair, test, and reinstall the engine of a car, van, or home-built airplane.

The cart consists of a framework of wood, steel, and aluminum components supported by four wheels. The engine is lifted from the vehicle by a hydraulic jack and gently lowered onto the waiting cart. The jack is then removed from under the engine. The rear of the vehicle is raised just enough that the engine can be rolled out from under it. The cart cradles the engine without denting or scratching it. The cart holds the engine low enough to clear the car and high enough to clear the jack.

Once loaded on the cart, the engine is accessible for removal and installation of parts. The engine can also be tested in operation on the cart. The cart easily supports a 200-lb (90-kg) engine. It can also be used to hold a transmission. With a removable sheet-metal top, the cart can also be used as portable seat.

This work was done by Gim Shek Ng of Langley Research Center. Further information is contained in a TSP [see page 1].
LAR-14858
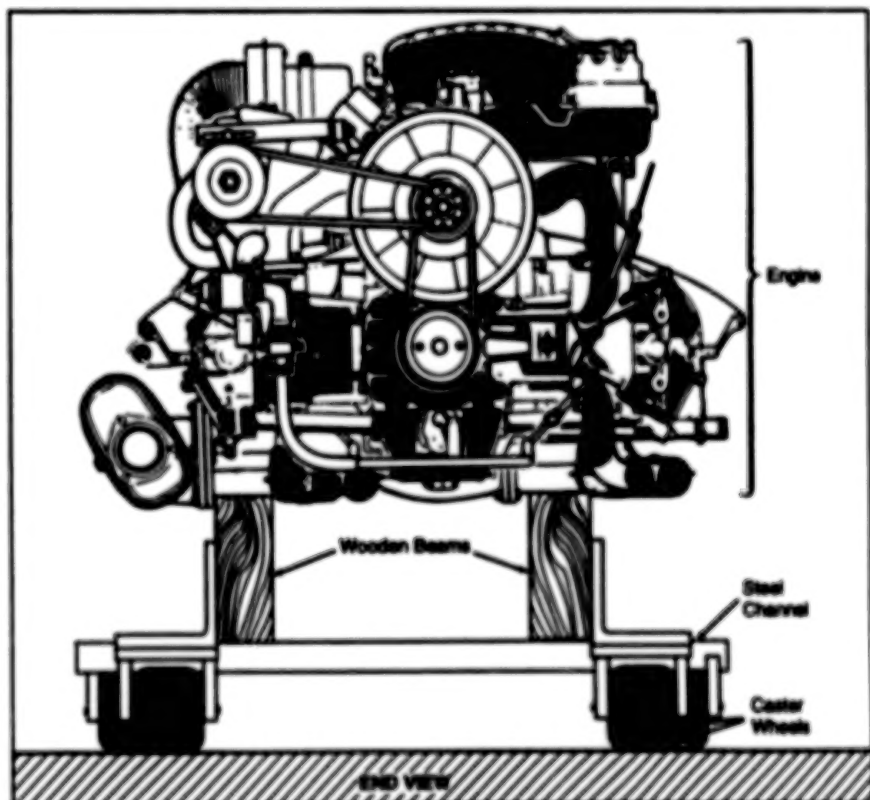
The Service Cart is made from readily available materials. Fabrication of the cart involves only straight cuts and no complicated machining.
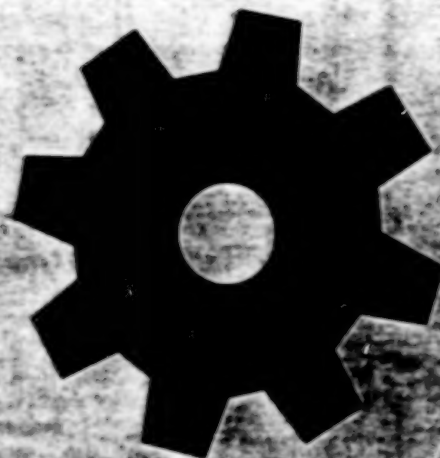
Machinery

Hardware, Techniques, and Processes

Roller/Gear Drives for Robotic Manipulators

Features include zero backlash, high efficiency, smooth motion, and back-drivability.

Lewis Research Center, Cleveland, Ohio

A pitch/yaw (two-axis) roller/gear drive and a wrist-roll (single-axis) roller/gear drive have been designed to incorporate several features that are desirable in robotic-joint actuators. These features include zero backlash, high efficiency, smooth motion (little ripple in torque and in speed ratio), and a high degree of back-drivability. Drives like these can be designed and fabricated readily. Since the mechanical complexity and tolerances of these drives are no more severe than are those of competing drives, costs of production should be comparable.

In the pitch/yaw drive (see Figure 1), torques are transmitted through bevel gears and bevel rollers acting in parallel. Pairs of bevel rollers associated with pairs of bevel gears are compressively loaded against each other at all times by Belleville springs. Dual input shafts are coupled to two sets of input bevel pinions and input bevel rollers. The motion of each input shaft can be clockwise or counterclockwise, independent of the motion of the other input shaft.

Motion is transmitted from the input pinions and rollers to intermediate bevel gears and bevel rollers. Each pair of intermediate gear and roller is mounted with a transversing bevel gear and transversing bevel roller. Motion is transmitted from both transversing-gear-and-roller pairs to a single output bevel gear and associated roller.

Turning both input shafts in the same direction at the same angular speed results in an output motion about the yaw axis. Turning both input shafts in opposite directions at the same speed results in output motion about the pitch axis. Other combinations of input angular velocities result in various combinations of output pitch and yaw.

At startup, the compressively loaded rollers transmit torque until the gears are in full contact. In so doing, the rollers eliminate the backlash that would occur with an ordinary gear train. As the rollers transmit torque, they undergo creep (very small slippage), which allows the gear teeth to come into contact and assume the torque-transmitting function. The rollers also react the radial components of the gear-tooth contact forces, so that the gears transmit only tangential forces: this helps to smooth tooth action, reducing cogging.
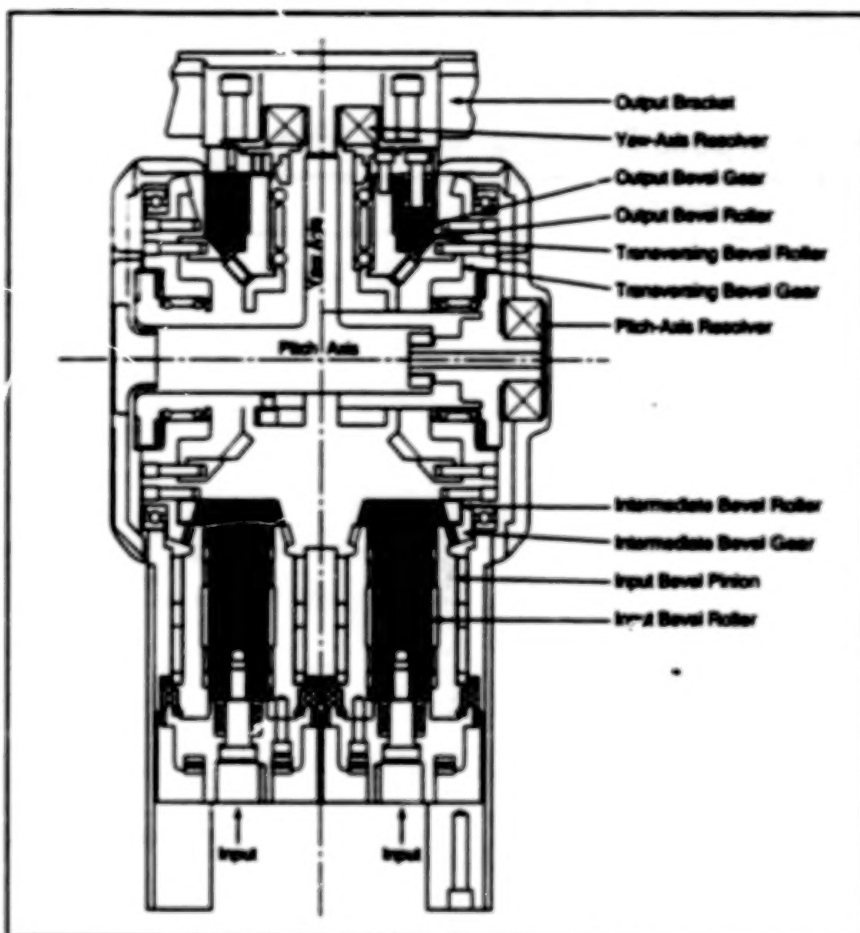

Figure 1. The Pitch/Yaw Drive is a novel two-axis drive that contains a combination of gears, rollers, and springs that act together to eliminate backlash and cogging.
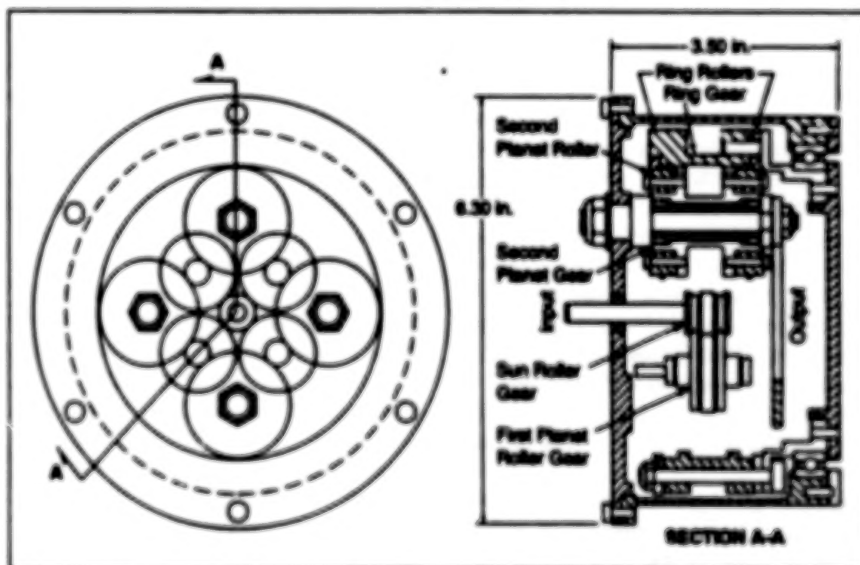

Figure 2. The Wrist-Roll Drive is a more-conventional single-axis drive that offers advantages like those of the pitch/yaw drive.

In the wrist-roll drive (see Figure 2), an input shaft is connected to a sun roller/gear. Torque is transmitted through the sun roller/gear to four first-row planet gears, then to four second-row planet gears, then to a ring roller/gear, then to an output shaft. The ring rollers are sized so that when they are assembled over the cluster of other rollers, they compressively load the other rollers.

At startup, as in the pitch/yaw drive, the compressively loaded rollers transmit torque until the gears are in full contact. As in the pitch/ya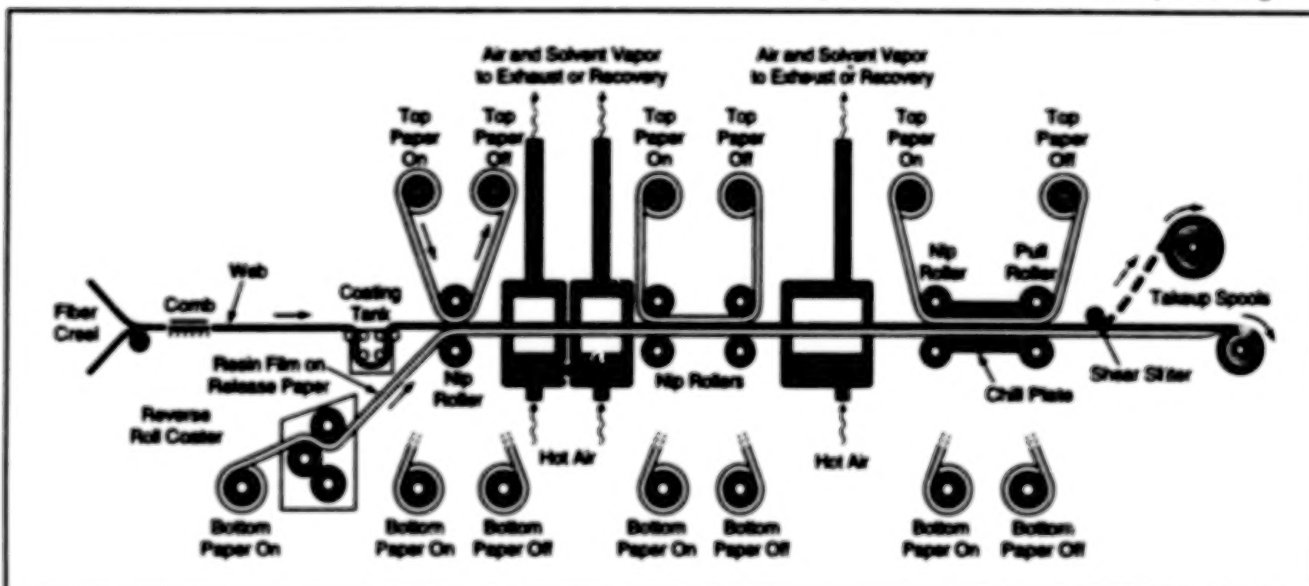w drive, the rollers eliminate backlash, bear the radial components of gear-tooth contact forces, and smooth the motion.

Multipurpose Prepregging Machine

Modularity imparts versatility.   *Langley Research Center, Hampton, Virginia*

The **Multipurpose Prepregging Machine** comprises modules that can be operated in a variety of configurations and sequences according to the materials used and the desired parameters of the product.

A machine has been designed and built for a variety of uses that involve coating or impregnating ("prepregging") fibers, tows, yarns, or webs or tapes made of such fibrous materials with thermoplastic or thermosetting resins. The prepreg materials thus produced are used to make matrix/fiber composite materials.

The machine (see figure) comprises modules that can be operated individually, sequentially, or simultaneously, depending on the nature of the specific prepreg material and prepregging technique to be used. It can be used, in particular, to make prepreg tapes from various materials by any one or a combination of any of the following techniques:
- solution prepregging with a dip tank,
- direct on-line solution or hot-melt prepregging by use of a reverse roll coater,
- application of pre-cast resin film (usually, a hot-melt thermosetting resin) that is made off line by a reverse roll coater and carried to the web on release paper, or
- collation and fusing of prepreg tows.

The first nip roller is used in direct on-line prepregging and in application of pre-cast resin film but not in solution coating because the web is not amenable to nipping until it has been dried in the first oven. Hot air is circulated through the oven, and evaporated solvent is recovered from the oven exhaust. The second, third, and fourth nip rollers are essential for elimination of splits and gaps formed in the prepreg web during evaporation of solvent.

An optional hot-sled module (not shown in the figure) is designed to provide the pressure needed to impregnate the web with a highly viscous polymer solution or melt. The chill plate cools the impregnated web in preparation for takeup and storage of the web, effectively freezing the resin and thereby preventing the loss that would otherwise be caused by squeezing resin out when the impregnated web is wound (along with takeup or release paper) on the takeup spool(s).

The machine incorporates a number of safety features. Emergency-stop buttons are located at several positions. In an emergency stop, the rolls open, clutches disengage, and motors and heaters are turned off. A "light curtain" sensor subsystem initiates an emergency stop if any part of an operator's body or an extraneous object enters the light curtain, which lies along the entire length of the machine. Temperature and solvent-vapor sensors help to alert the operator to hazardous conditions that necessitate emergency stops. Sprockets and drive chains are covered and positioned so that the operator will not inadvertently become caught in them.
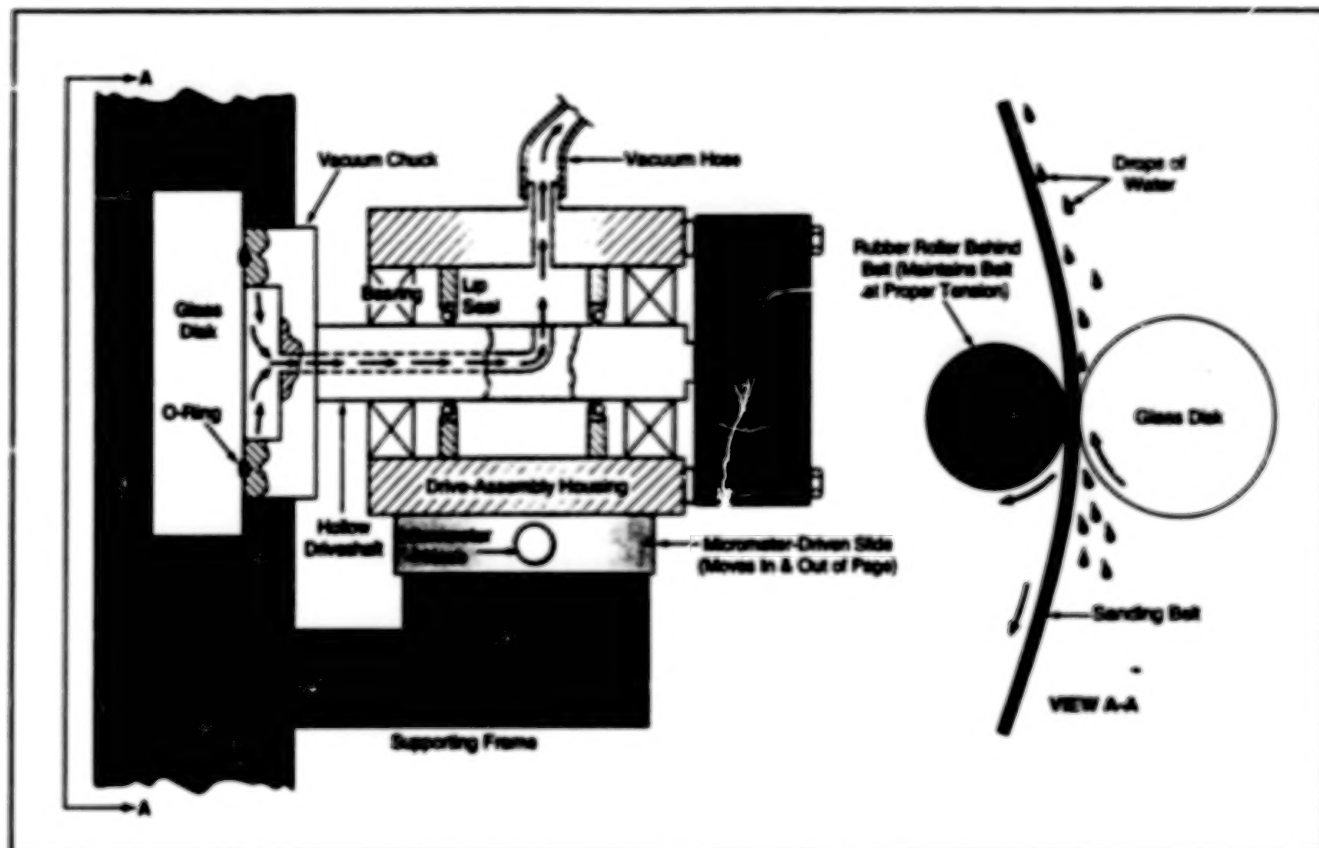
Grinding Glass Disks on a Belt Sander

An attached unit shapes disks to dimensions
within tolerances of most uses.

Goddard Space Flight Center,
Greenbelt, Maryland

Held on the Driveshaft by Vacuum, the glass disk is rotated while its periphery is ground by a continuous sanding belt.

A small machine that is attached to a table-top belt sander makes it possible to use the belt sander to grind a glass disk quickly to a specified diameter within a tolerance of about ±0.002 in. (about 0.05 mm). The belt sander with this machine attached is intended to be used in place of a production-shop glass grinder, which is more versatile (able to grind tapers, cones, and other shapes as well as cylindrical disks), but is far more expensive, slower, larger, and more accurate than necessary for most applications. Whereas a typical production-shop glass grinder costs about $100,000, the attachment-and-sander combination costs only about $6,000 (1993 prices).

The belt sander is a standard commercial unit equipped with a gravity-feed water-drip system that cools and lubricates the disk and belt at the point of contact. The belt is of a diamond-abrasive type that cuts faster and lasts about 1,000 times longer than carborundum-type belts. A motor turns the 64-in. (1.63-m) belt at 1,725 r/min.

The attachment includes a supporting frame, a motor-driven drive assembly, and a micrometer-driven slide that is used to adjust the position of the drive assembly (see figure). The drive assembly holds the glass disk to be ground, pressing the edge of the disk against the sanding belt and rotating the disk in a direction opposite the motion of the belt. A technician adjusts the micrometer, which is graduated in increments of 0.001 in. (0.0254 mm), until the glass disk has been ground down to the specified diameter.

The glass disk is held by a vacuum chuck on the outer end of a hollow driveshaft that protrudes from the drive assembly. The drive assembly rotates the shaft to turn the glass disk against the sanding belt at 18 r/min. An O-ring seals the glass disk to the vacuum chuck. The vacuum is supplied by an external vacuum pump through a hose to a cavity in the drive-assembly housing, then through a side hole into the axial hole in the hollow driveshaft. A pair of pressure-assisted lip seals around the driveshaft in the cavity of the drive-assembly housing prevents leakage of air into the vacuum line.

The vacuum chuck makes it unnecessary to fasten the disk with wax, as is done on production-shop grinders. Mounting the disk on the vacuum chuck takes only seconds instead of as much as a half hour when wax is used. The disk is released just as quickly, and there is no wax to clean from either the chuck or the disk.

*This work was done by James J. Lyons III of **Goddard Space Flight Center**. Further information is contained in a TSP [see page 1].*

This invention is owned by NASA, and a patent application has been filed. Inquiries concerning nonexclusive or exclusive license for its commercial development should be addressed to the Patent Counsel, Goddard Space Flight Center [see page 1]. Refer to GSC-13580.

# Controlling Flows of Two Ingredients for Spraying

Closed-loop control with feedback from flowmeters provides steady flows at specified rates.

Marshall Space Flight Center, Alabama

A closed-loop servo control subsystem has been incorporated, as a modification, into a system that controls the flows of two ingredients (designated "A" and "B") that are mixed and sprayed to form thermally insulating foams on large tanks. In the unmodified system, the overall speed of pumping both ingredients is controlled, in open-loop fashion, by a manually adjusted pressure regulator. In comparison with the foams produced by the unmodified system, the foams produced by the modified system are smoother and of higher quality. Continued use of the modified system is expected to result in substantial reduction in cost stemming from close control of application of foam and consequent reduced use of material.

The system (see figure) includes two constant-displacement pumps driven by a single linear hydraulic double-acting drive cylinder. The motion of the drive cylinder is modulated as needed to provide constant flow of each ingredient: this is done by applying the appropriate feedback command to a high-frequency-response servo valve that controls the flow of hydraulic fluid in the drive cylinder. At the end of each cylinder stroke, a rocker arm activates a limit switch, triggering a relay that changes the polarity of signals from a servo amplifier to the servo valve and thus reverses the direction of the cylinder.

Flows of both ingredients are monitored by flowmeters. The outputs of the flowmeters are processed through frequency-to-voltage converter circuits to supply feedback to the servo amplifier, and to a computer. The servo set-point voltage (corresponding to the desired overall rate of flow) can be set manually through a variable resistor. Alternatively, the set point
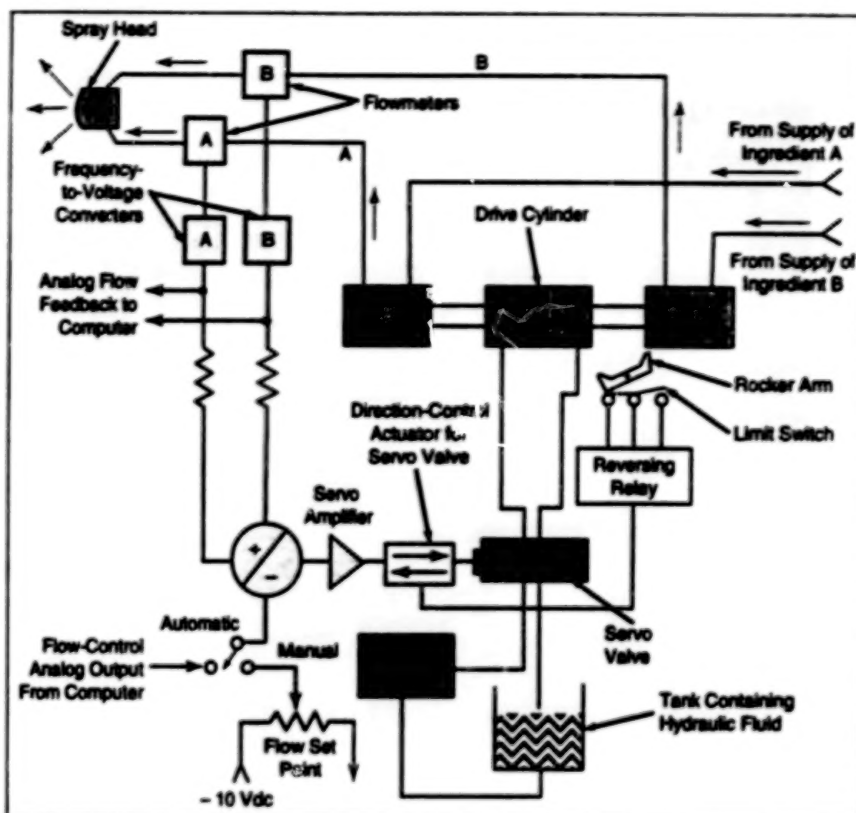
This **Material-Dispensing System** with feedback control can be set manually or by computer to pump ingredients A and B at a variable overall rate but at a constant ratio.

can be controlled from the computer, in coordination with computer control of the position and orientation of the spray head relative to the workpiece, to make the thickness of the foam vary with position on the workpiece according to specifications. As the flow of each ingredient increases or decreases, feedback from the associated flowmeter also increases or decreases, and the amplified feedback signal gives rise to a compensating decrease or increase in the rate of pumping that ingredient in an effort to

maintain the flow at the set-point rate. Accumulators keep the rates of flow nearly constant during the change of direction at the end of each stroke.

This work was done by Huel H. Chandler of Martin Marietta Corp. for Marshall Space Flight Center. Further information is contained in a TSP [see page 1].

Inquiries concerning rights for the commercial use of this invention should be addressed to the Patent Counsel, Marshall Space Flight Center [see page 1]. Refer to MFS-28824.

Computing Dynamics of a Robot of 6+n Degrees of Freedom

An improved formulation is widely applicable and requires less computation than do prior methods.

Lyndon B. Johnson Space Center, Houston, Texas

An improved formulation speeds and simplifies the computation of the dynamics of a robot arm of n rotational degrees of freedom mounted on a platform that has three translational and three rotational degrees of freedom. This formulation is intended for use in dynamical modeling of robotic manipulators

attached to such moving bases as a spacecraft, aircraft, vessel, or land vehicle. Such modeling is an important part of the simulation and control of robotic motions.

Prior formulations have been limited, for the most part, to stationary-base industrial robots that have specific configurations,

and have required more computation than could be performed in real time. The new formulation overcomes both limitations, offering the potential for real-time modeling, on typical computer workstations, of the dynamics of both fixed- and moving-base robotic manipulators that have a variety of configurations.

The improved formulation begins with Lagrange's equations of motion for the 6+n-degree-of-freedom system. (Gravitation, friction, backlash, and other complicating effects are not considered in the present version, but are expected to be taken into account in subsequent versions.) The kinetic energy of the system is partitioned into translational and rotational components: This expedites the simplification of the equations through the use of basic vector identities. The resulting components are summed to obtain an overall generalized set of equations of motion. The velocities and accelerations of the links of the robot arms are parameters in the generalized equations. Equations for these parameters are obtained by differentiation, with respect to time, of the equations for the positions of the centers of mass of the links.

The generalized equations of motion are put in matrix-vector form. Intermediate parameters are introduced for simplification. Coriolis, centrifugal, and cross-coupling terms are combined into a generalized forcing-function term, and inertial terms are factored out to form a mass matrix, in which elements are
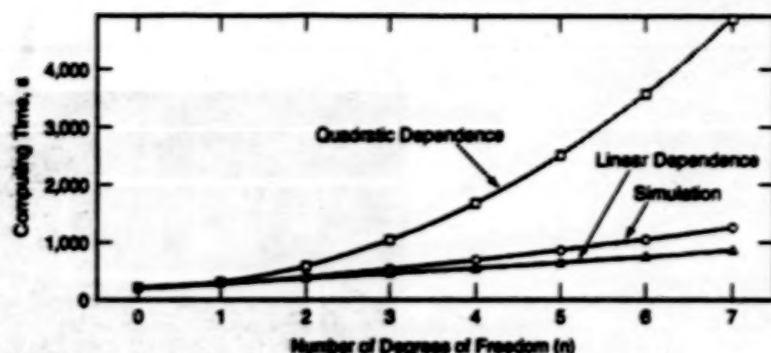
The Computing Time required to conduct a representative dynamical simulation was found to increase only slightly more steeply than linearly with n. Typically, in prior formulations, the computing times increase more steeply with n, making real-time simulation impractical.

arranged in three block-diagonal groups that represent the translational degrees of freedom of the base, the rotational degrees of freedom of the base, and the rotational degrees of freedom of the joints of the manipulator, respectively. In this form, the forward dynamics problem (given the forces and torques, find the accelerations) can be solved.

The new formulation was tested in representative simulations involving the six degrees of freedom of the platform

and various n from 0 to 7. As shown in the figure, the computation time increased slightly more steeply than a simple linear dependence on n, but much less steeply than a quadratic dependence on n.

This work was done by Leslie J. Quiocho of Johnson Space Center and Robert W. Bailey of Lincom Corp. Further information is contained in a TSP [see page 1].
MSC-21751

Improved Program for Calculation of Heat-Load Multiplier

Repetitive calculations are accelerated and partly automated.

Marshall Space Flight Center, Alabama

The PRM1940 computer program computes a heat-load multiplier for use in the Power Balance Model (PBM) computer program. PBM calculates hundreds of operating parameters of the main engine of the space shuttle from relatively few measurement data. PRM1940 is a stand-alone program which incorporates only those PBM calculations necessary to compute the heat-load multiplier. PRM1940 was developed to accelerate and partly automate the calculation of the heat-load multiplier; previously, the heat-load multiplier was calculated in a time-consuming, labor-intensive procedure that involved multiple runs of PBM. Although these programs are specific to the space shuttle application, they may be of interest to engineers concerned with monitoring of conditions in turbines, chemical-processing plants, and

other high-temperature flow machinery.

One of the parameters that PBM calculates is the rate of coolant flow in the main combustion chamber of the engine. It determines this rate in an iterative fashion by varying the rate until two independent methods of calculating the rise in enthalpy of the main-combustion-chamber coolant yield values that agree with each other. One of these enthalpy-rise calculations is based on measured temperatures and pressures. The other is based on a main-combustion-chamber reference heat load, which is scaled by the heat-load multiplier. Previously, the user supplied the heat-load multiplier. The user "tuned" the rate of flow to a desired value by use of this multiplier.

PRM1940 reads files of data specified by the user and performs only those cal-

culations that are necessary for the PBM iterative calculation the rate of flow. PRM1940 calls an algorithm (known as the Osugi algorithm) that determines the desired rate of flow, then varies the heat-load multiplier until the rate of flow calculated via the PBM methodology matches the Osugi rate of flow.

The resulting heat-load multiplier is written to a file in a format in which it can be incorporated directly into the PBM input file. The user enters this multiplier into PBM, which then calculates a rate of flow matched to the Osugi rate.

This work was done by Mark D'Valentine of Rockwell International Corp. for Marshall Space Flight Center. Further information is contained in a TSP [see page 1].
MFS-30019
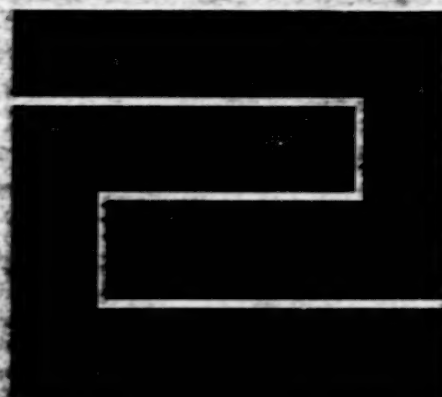
Fabrication Technology

Hardware, Techniques, and Processes

Truss Fastener Operable by Robot

A chuck key is the only tool required.

Lyndon B. Johnson Space Center,
Houston, Texas

A fastener assembly for use in erecting a truss structure can be assembled by a robot equipped with one arm and one gripper. The fastener assembly makes it easier for a robot or human technician to build such a structure in outer space or on Earth.

The fastener assembly features an extremely large capture envelope; it can accommodate initial lateral misalignments of truss members of as much as 0.4 in. (1 cm) and rotational misalignments as large as 26° and still produce a sound structural connection.

The fastener assembly goes together loosely while it grossly aligns itself, producing low forces and rarely jamming. When it is tightened, however, it produces very large alignment forces as it is seated.

The fastener assembly includes two primary subassemblies: the receptacle (which is attached to a ball at one of the nodes of the truss structure) and the joint (which is attached to a truss strut). A hammerhead probe protrudes from the joint (see figure). The curved surfaces of the hammerhead give the fastener its ability to recover from large misalignments.

Holding the joint by its gripper-alignment grooves, the robot assembles the fastener by inserting the hammerhead into the receptacle. The contours of the hammerhead slide with a camlike action on chamfers of the insertion hole. The chamfers guide the head and shaft into the receptacle.

The robot inserts a chuck key that engages a ring gear in the joint, and rotates the key to retract the shaft into the joint housing, thereby pulling the hammerhead into its seat in the receptacle. A clocking (alignment) stub on the joint engages the receptacle, removing any remaining rotational misalignment between joint and receptacle. The robot continues to rotate the chuck key until Belleville washers in the joint housing are compressed, preloading the receptacle and joint and completing the structural connection. For disassembly, the procedure is simply reversed.

This work was done by George F. Parma of Johnson Space Center and Mark H. Vandeberghe and Steve C. Ruiz of Lockheed Engineering and Sciences Co. Further information is contained in a TSP [see page 1].
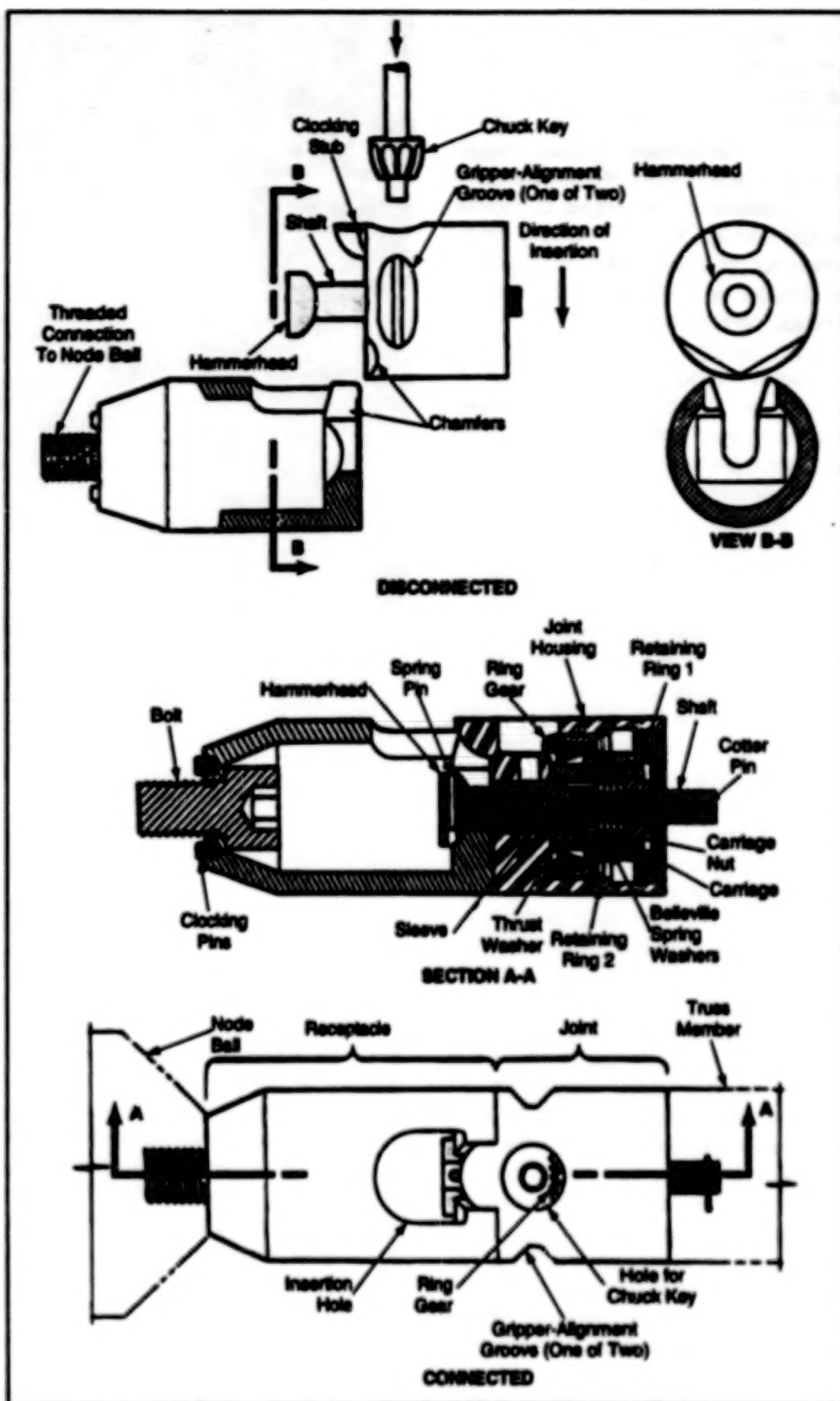
The Hammerhead is inserted in the chamfered receptacle slot. After the hammerhead is seated and the ring gear is rotated by use of a chuck key, the joint and receptacle constitute a stiff unit (bottom).

Etching Semiconductors With Beams of Reactive Atoms

Hyperthermal beams of atoms are directed at masked substrates.

A method of etching semiconductors with energetic beams of electrically neutral, but chemically reactive, species is undergoing development. The method, when fully developed, should enable etching of straight walls into semiconductor substrates at the edges of masks without damage to the underlying semiconductor material. Unlike etching with ion beams or plasmas, there are no charged particles bombarding the wafer. Charge damage is manifested during reactive ion etching (RIE) in two ways: (1) nonuniform ion current to the wafer which may result in differential charging of adjacent regions and subsequent electrical breakdown through the underlying semiconductor, and (2) charging of insulating photoresist masks which may affect the profile of the sidewalls by altering ion trajectories. In addition to elimination of charge damage, the new etching technique reduces substrate bombardment damage because the translational energy of the neutral species is in the range 2 to 12 eV, below the damage threshold of many semiconductor materials. Furthermore, the low-energy neutrals cause no mask erosion (typically seen in RIE), thereby allowing for etching features with very high aspect ratios.

Atomic fluorine was used as the reactive species in preliminary experiments to demonstrate the feasibility of the method. The experiments were performed with an apparatus designed originally for studying the effects of bombardment by atomic oxygen on spacecraft materials in low orbit around the Earth. A pulse of sulfur hexafluoride was introduced into the small end of a conical nozzle, where a focused, 5-J pulse from a CO_2 laser induced breakdown in the gas and heated the plasma to a temperature over 20,000 K. The SF_6 precursor gas was completely dissociated in the hot plasma. As the plasma expanded rapidly from the con-
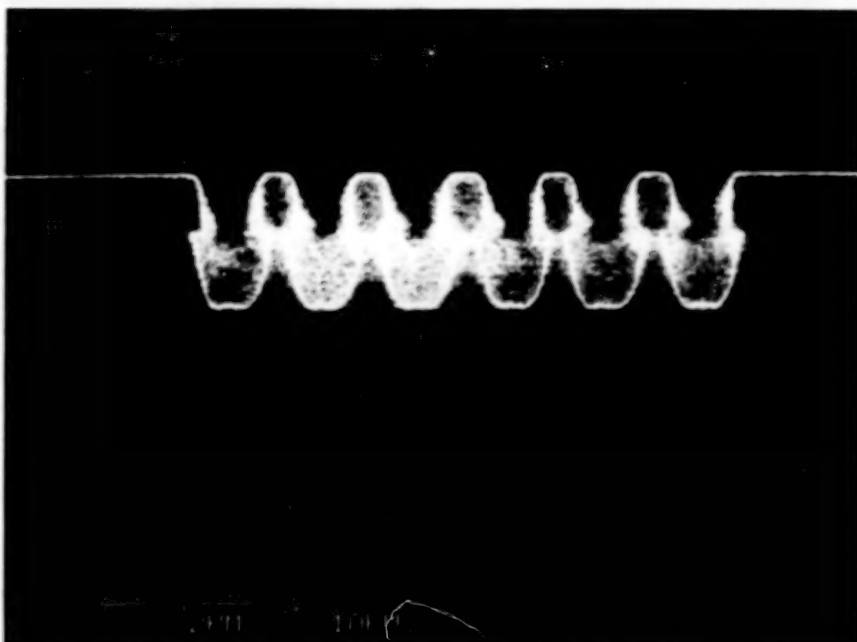
This Scanning Electron Micrograph shows a cross-sectional view of trenches that were etched into a silicon wafer by a hyperthermal beam of directed fluorine atoms. The undercutting is a common phenomenon in the industry, but is expected to be eliminated or at least reduced in subsequent refinement of this method.

finement of the nozzle cone, efficient electron-ion recombination took place, resulting in a directed beam of fluorine atoms with an average translational energy of approximately 5 eV.

The beam was found to etch, at a rate of 300 Å/min, a silicon wafer placed at a distance of 30 cm from the source. However, etched features at this location exhibited 50 percent undercutting of the mask. By increasing the source-to-wafer distance to 92 cm and collimating the beam with an aperture, which also allowed for differential pumping of the source and etching chambers, the undercutting was reduced to 15 percent (see figure). This undercutting is expected to be reduced further by minimizing the energy and flux of scattered fluorine atoms which do not react upon initial impingement on the surface but which

may react during secondary collisions with the sidewalls.

This work was done by Timothy K. Minton, Konstantinos P. Giapis, and Teresa A. Moore of Caltech for NASA's Jet Propulsion Laboratory. Further information is contained in a TSP [see page 1].

In accordance with Public Law 96-517, the contractor has elected to retain title to this invention. Inquiries concerning rights for its commercial use should be addressed to

William T. Callaghan, Manager
Technology Commercialization
JPL-301-350
4800 Oak Grove Drive
Pasadena, CA 91109
Refer to NPO-19203, volume and number of this NASA Tech Briefs issue, and the page number.

Improved Growth of Cadmium Telluride Crystals From Vapors

High-quality crystals can be grown efficiently.

Effusive ampoule physical vapor transport (EAPVT) is an improved technique for growing high-quality crystals from vapors. EAPVT is likely to be used commercially for efficiently growing vari-

ous semiconductor compounds in the form of single crystals of high structural and compositional uniformity.

Because crystals are grown from vapors at temperatures lower than

those used to grow crystals from melts, the crystals grown from vapors are often purer and more nearly structurally perfect. However, growth of crystals from vapors has largely been limited to

preparation of layers rather than bulk crystals. This is because most workers in vapor growth have observed slow growth and complex transport behavior. Recent research has shown that these difficulties are not inherent features of crystallization from vapors but are largely consequences of traditional vapor-growth technology, which provides for only limited control of parameters of transport and growth. In particular, fluid-dynamic studies of vapor transport in closed ampoules have shown that the limitations on transport result from accumulations of gaseous impurities around growing crystals.

The development of EAPVT was guided by these insights. In EAPVT (see figure), impurity vapors and excess (incongruent) components of the growth vapor(s) are continuously removed from the vicinity of the growing crystal by effusion through predetermined leaks to a vacuum. Transport under the resulting congruent vapor conditions is so rapid that it is necessary to take measures to limit transport rates to values conducive to a high degree of structural perfection of new growth onto a single-crystal seed plate. Accordingly, transport rates are controlled by use of capillary restrictions between the vapor source and the growing crystal. The EAPVT apparatus also includes an infrared-reflective viewing port for optical in situ monitoring of the structure of the growing crystal, thereby enabling the efficient determination of optimal thermal and transport operating conditions.

In an experiment, EAPVT was used to grow cadmium telluride, which is important for making optoelectronic devices. Largely-single-crystal boules 25 mm in diameter and 25 mm long were produced within 48 hours. This demonstrated rates
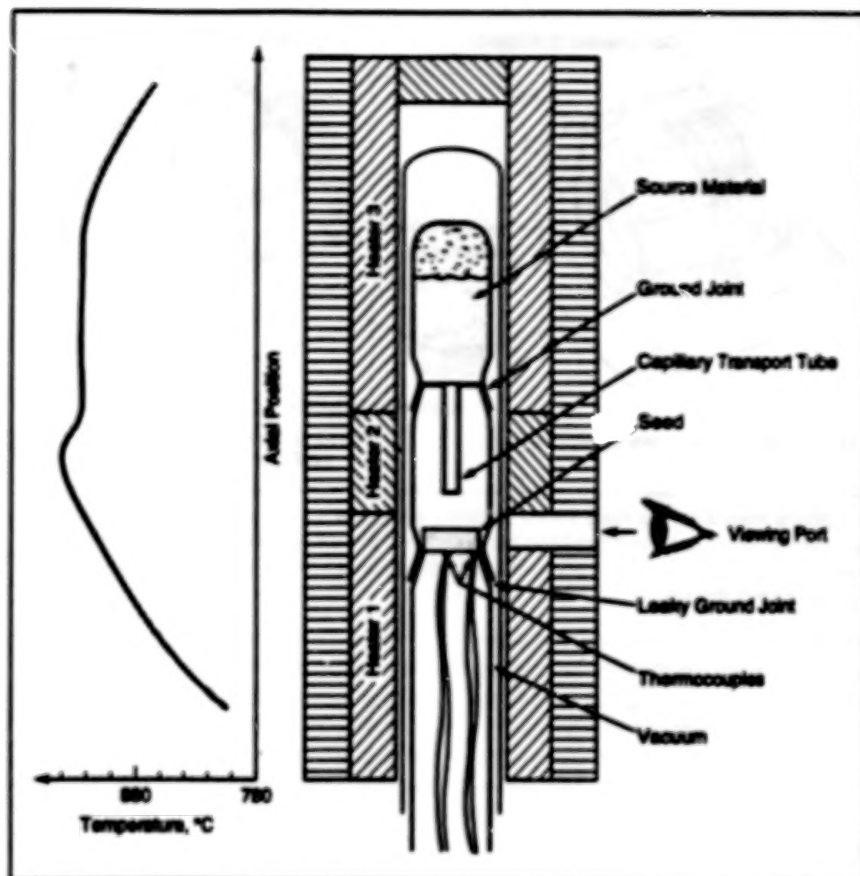
The **EAPVT Apparatus** is shown here in schematic cross section along with an idealized axial temperature profile.

of growth that approach those obtained in melt growth of cadmium telluride. The boules exhibited dislocation (etch-pit) densities as low as 2×10^3 cm^{-2}, low twin densities, and carrier concentrations = 8×10^{15} cm^{-3}. Tellurium precipitates were limited to grain and twin boundaries, and optical absorption measurements indicated high purity of the material.

This work was done by Franz Rosenberger and Michael Banish of The University of Alabama in Huntsville and Walter M. B. Duval of **Lewis Research**

Center. Further information may be found in NASA TM-103786 [N92-16158/TB], "Vapor Crystal Growth Technology Development — Application to Cadmium Telluride."

Copies may be purchased [prepayment required] from the NASA Center for AeroSpace Information, User Services Division, Linthicum Heights, Maryland, Telephone No. (301) 621-0394. Rush orders may be placed for an extra fee by calling the same number.
LEW-15737

Quick-Connect, Slow-Disconnect Nut

The nut would snap into engagement but would be turned conventionally for removal.

Marshall Space Flight Center, Alabama

The figure illustrates a proposed quick-connect, slow-disconnect nut that would be installed simply by pushing it onto a standard bolt or threaded stud. Once installed, it could be removed only by unscrewing it in the manner of a conventional nut.

The nut would include a hexagonal outer case that would resemble an ordinary nut and would hold several shells in its hole. Each shell would include a key that would protrude radially outward and

engage a lengthwise groove in the case: this would prevent rotation of the shell relative to the case. Most of the inner surface of the hole would be conical, and each shell would have a conical outer surface that would slide axially on the conical inner surface of the hole. Except in the gaps between the shells, the inner surfaces of the shells would collectively constitute a standard threaded surface. Two C-shaped spring clips would be snapped into recesses at the

ends of the shells. These clips would push the shells outward against the conical inner surface of the hole, thereby also pushing them axially toward the wide end of the cone. A coil spring would provide sufficient force to overcome the axial force from the C-clips, pushing the shells axially toward the narrow end of the cone, where they would be stopped by a flange.

In preparation for installation of the nut on a bolt, the nut would be oriented

SHELLS SHOWN IN NORMAL POSITION   SHELLS SHOWN PUSHED AXIALLY AGAINST COIL SPRING
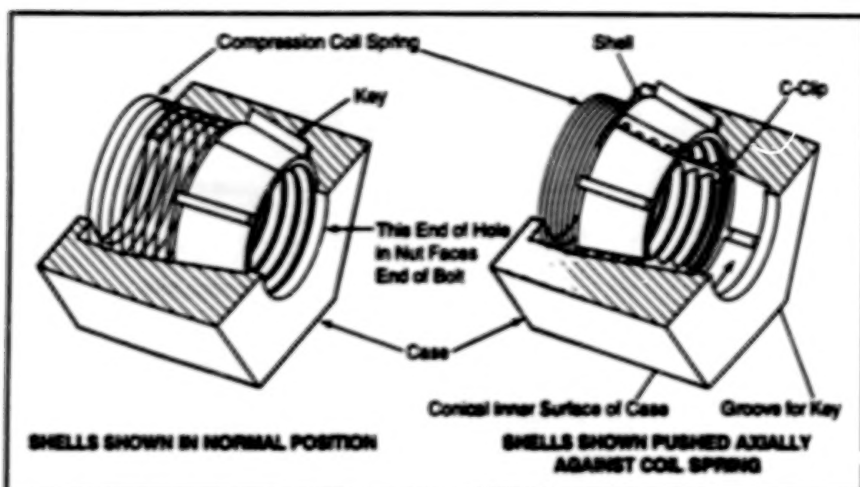
The Shells Would Be Pushed toward the wide end of the cone during installation, causing the shells to slide over the threads on the bolt. Then the spring would push the shells back toward the narrow end of the cone, causing the threaded inner surfaces of the shells to engage the bolt thread.

with the narrow end of the cone nearest the nut. The nut would then be pushed axially onto the bolt, causing the bolt to push the shells, against the coil spring, toward the wide end of the cone, while the C-clips would push the shells radially outward. The shells would then slip past the external thread on the stud.

Once the nut had been pushed as far as possible onto the bolt, the coil spring would again force the shells toward the narrow end of the cone, causing the shells to move radially inward and engage the bolt thread. Thereafter, the nut would be retained by the bolt; trying to pull the bolt out of the hole would only cause it to engage the nut more securely.

The nut would then be secured further by rotating it clockwise in the usual way. The keys would force the shells to rotate with the outer case. This motion would drive the shells toward the narrow end of the cone until they squeezed radially inward against the bolt thread and/or were stopped by the flange at the narrow end of the cone. In acting as a hard stop, the flange would limit the outward force exerted by the shells on the case, thereby preventing splitting of the case in the tightened condition. To remove the tightened nut, one would simply rotate it counterclockwise in the usual way until it disengaged from the bolt thread.

This work was done by Bruce Weddendorf of Marshall Space Flight Center. Further information is contained in a TSP [see page 1].

This invention is owned by NASA, and a patent application has been filed. Inquiries concerning nonexclusive or exclusive license for its commercial development should be addressed to the Patent Counsel, Marshall Space Flight Center [see page 1]. Refer to MFS-28833.

Automated Hardware-Identification System

Compressed symbology will be used to reduce paperwork and coordinate flows of information and hardware.

Marshall Space Flight Center, Alabama

Computer-controlled peening and engraving machines have been used to apply compressed symbology to hardware components made of a variety of metals, as part of a continuing effort to develop "paperless" systems for manufacturing and for tracking inventories. "Compressed symbology" denotes an emerging technology that involves one- and two-dimensional arrays of surface depressions to form optically readable dots. These patterns are more durable and are generally denser than common bar codes are. Like bar codes, they convey identification data in binary form and are read by optoelectronic sensors. Computers and the compressed-symbology engraving machines that they control will eventually constitute subsystems of "paperless" hardware-tracking and -identification systems that will coordinate flows of both identifying information and the identified parts themselves, along with ancillary information like work orders.

The computer in an experimental subsystem of this type identifies appropriate marking devices, converts identification data into marking code, and automatically drives the marking operation. The software that controls these functions guides the marking-machine technician through a brief, easy-to-understand question-and-answer session. Future modifications of the software are expected to accelerate marking operations, eliminate the need for trial or practice marking, and reduce the incidence of errors. These modifications will include incorporation of optimum hardware-marking parameters and/or marking-machine-setup information for each major type of material to be marked. In addition, import and export links to the user's host computer are being incorporated to enable verification of serial numbers and other part numbers before marking operations begin. Eventually, the computer will select the marking sequence on the basis of the data on the identity of each part.

Plans for a prototype part-identifying subsystem call for a portable pen computer with symbol-decoding software operating in conjunction with a hand-held charge-coupled-device video camera. A host computer will write the electronic equivalent of work-authorizing documents, which will be downloaded to the portable computer. Using the portable computer, a technician will call up the documents and use them to perform manufacturing operations. By use of the camera, data on identities will be acquired from compressed symbology on parts, employee badges, and menus that reside in the affected work areas. These data will be incorporated into the appropriate places in the electronic documents. Upon completion of manufacturing operations, updated information on the work status of identified parts will be downloaded to the host computer via radio transmission.

This work was done by Harry F. Schramm, Jr., of Marshall Space Flight Center and Donald L. Roxby of Rockwell International Corp. Further information is contained in a TSP [see page 1].

Inquiries concerning rights for the commercial use of this invention should be addressed to the Patent Counsel, Marshall Space Flight Center [see page 1]. Refer to MFS-28776.
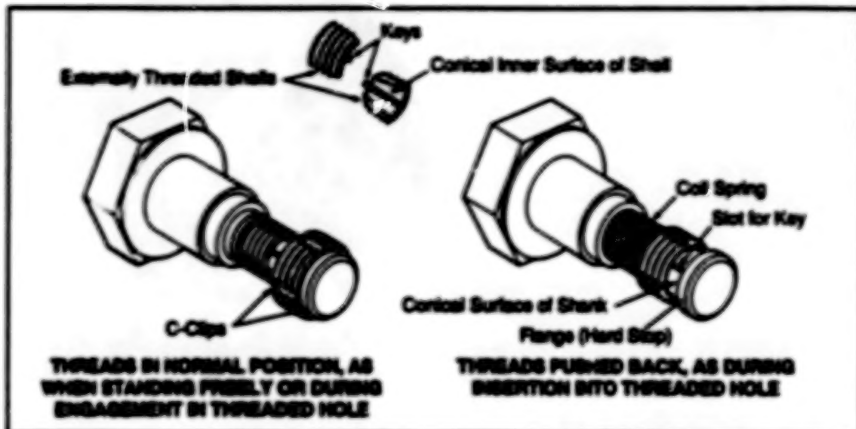
62

Quick-Connect, Slow-Disconnect Bolt

The bolt would be installed by pushing, but removed conventionally by rotation.

Marshall Space Flight Center, Alabama

The figure illustrates a proposed bolt that would function similarly to the device described in the accompanying article, "Quick-Connect, Slow-Disconnect Nut" (MFS-28833). The bolt would be installed in a standard threaded hole simply by pushing it into the hole. Once inserted, the bolt could be withdrawn only by turning it in the conventional way.

The bolt would include circumferential shells, each having a conical inner surface that would slide on the conical outer surface of a shank. A key would protrude radially inward from each shell and would engage a lengthwise slot in the shank: this would prevent rotation of the shell relative to the shank. Except in the gaps between the shells, the outer surfaces of the shells would constitute a standard external thread. Each shell would have circumferential grooves at both ends. A C-shaped spring clip would wrap around all shells at each end, holding them against the conical surface of the shank. A coil spring would provide sufficient force to overcome the axial force from the C-clips, pushing the shells axially toward the tip of the shank (toward the wide end of the cone).

When the bolt was pushed into a threaded hole, the first thread in the hole would drive the shells back, away from the end of the bolt compressing the coil spring. As the shells moved toward the narrow end of the cone, the C-clips would urge them radially inward. This action would reduce the outside diameter of the shells to less than the minor diameter of the thread in the hole. The shells would thus slip into the hole.

THREADS IN NORMAL POSITION, AS WHEN STANDING FREELY OR DURING ENGAGEMENT IN THREADED HOLE

THREADS PUSHED BACK, AS DURING INSERTION INTO THREADED HOLE

During installation, the externally threaded shells would be pushed back toward the narrow end of the cone, so that they would slide readily, into the threaded hole. Once the bolt had been inserted as far as possible into the hole, the coil spring would push the shells outward on the cone so that they would engage the thread in the hole.

Once the bolt had been pushed as far as possible into the hole, the coil spring would again force the shells toward the wide end of the cone. As the shells moved outward on the cone, they would come into engagement with the thread in the hole. At this point, the bolt would be positively retained in the hole; pulling the bolt would only drive the shells more firmly into the thread in the hole.

Installation would be completed by turning the bolt clockwise to tighten it in the conventional manner. The keys in the shells would force them to rotate with the shank when the bolt head was turned: this motion would drive the shells toward the wide (outer) end of the cone, until they are stopped by the flange at the end of the bolt. This flange serves to carry almost all of the tension load of the bolt, with a

small component carried by the conical surface. By increasing the diameter of the conical surface, it can be made to carry more of the tension, which will produce a radial force to lock the fastener if desired. To loosen the bolt, one would simply turn it counterclockwise in the usual way until it disengaged from the threaded hole.

Enhancement of Water-Jet Stripping of Foam

A robotic water-jet system removes foam only; adjacent areas are spared.

Marshall Space Flight Center, Alabama

An improved robotic high-pressure-water-jet system strips foam insulation from parts without removing adjacent coating materials like paints, primers, and sealants. The robot can even inject water into crevices and blind holes to clean out foam, without harming adjacent areas. Developed for postflight refurbishing of aft skirts of booster rockets, the system includes a six-axis robot that has been provided with a special end effector and specially written control software, called Altfoam. The system should be adaptable to cleaning and stripping in other industrial settings.

The robotic system is used in place of a manually operated water-jet cleaner that inevitably removed peripheral coatings as well as the foam. It was then necessary to completely strip the coating by walnut-hull blasting, then recoat the surfaces. The use of the robotic system eliminates both the cost of full stripping and recoating and the problem of disposing of toxic solutions used in preparation for coating. Now, only minor touching up is needed on the surfaces adjacent to the removed foam.

The robotic foam-stripping system blends readily into the existing production environment. The special foam-stripping

end effector is designed to be highly reliable and requires only normal maintenance. No additional safety procedures are required.

Mathematics and Information Sciences

Hardware, Techniques, and Processes

Books and Reports

Detecting Faults by Use of Hidden Markov Models

**The frequency of false alarms can be reduced.**

NASA's Jet Propulsion Laboratory, Pasadena, California

Faults in a complicated dynamic system (e.g., an antenna-aiming system as shown in the figure, a telecommunication network, or a human heart) can be detected automatically by a method of automated, continuous monitoring. The basic idea is to obtain time-series data by sampling multiple sensor outputs at discrete intervals of t and to process the data via an algorithm that determines whether the system is in a normal or faulty state. The algorithm implements, among other things, a hidden first-order temporal Markov model of the states of the system. A mathematical model of the dynamics of the system is not needed.

The present method is the "prior" method mentioned in "Improved Hidden-Markov-Model Method of Detecting Faults" (NPO-18982), *NASA Tech Briefs*, Vol. 18, No. 8 (August 1994), page 44. The monitoring problem can be stated as a data-classification problem: Let there be k sensors, the collective outputs of which constitute a k-dimensional output vector $y(t)$, where t is time. Given the sequence of $y(t)$ sampled at discrete intervals of t, infer the current state of the system; that is, assign the data to a class that represents the current state of the system.

In the present method, one assumes that at any given time, the system can be in only one state (the ith state, denoted ω_i), which is a member of a finite set of m states. Only the state ω_1 is deemed normal; the other states (ω_2 through ω_m) are deemed faulty. It is assumed that all faults and their symptoms can be identified in advance by testing, simulation, and/or use of design information, and that a data base called a "fault library" can be generated for both the normal and faulty states: the fault library consists of pairs of symptom vectors and class (state) labels of the form $(y_j, \omega_{\omega j})$, $1 \leq j \leq N$, where N is the total number of pairs in the library.

The sampled data $y(t)$ are not used directly but instead are first preprocessed into feature vectors $\theta(t)$ that represent relevant statistical characteristics of the time series and are assumed to be sufficient to characterize the system. For this purpose, consecutive sampling intervals τ are grouped into consecutive blocks of time, each $T = W\tau$ long (where W is an integer), and the
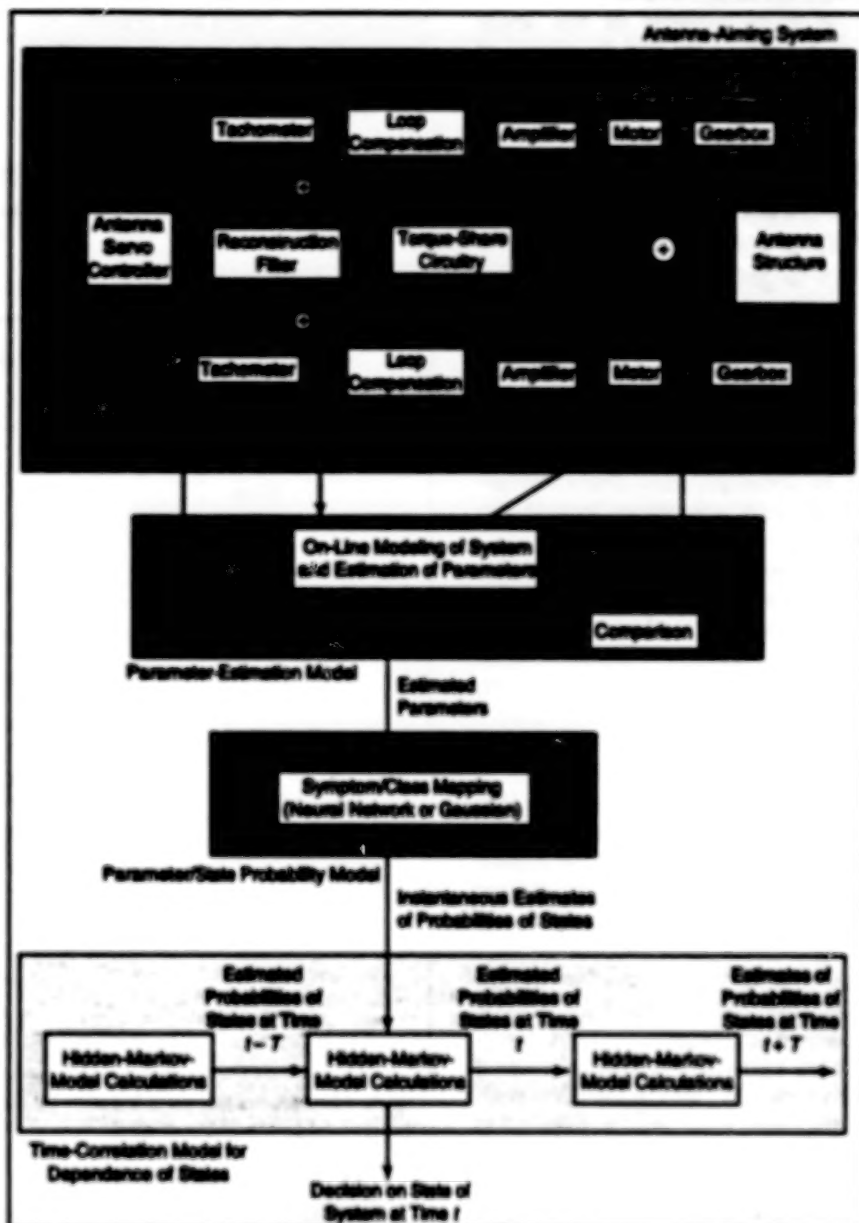
The **Hidden-Markov-Model Method Was Tested** by using it to diagnose faults in the electronic/electromechanical aiming system of a large astronomical antenna. This method yielded fewer incorrect diagnoses of normal or faulty conditions than did other methods.

feature vector for the block at time t is given by

$$\theta(t) = f\big(y(t), y(t-\tau), ..., y(t-T)\big)$$

The state of the system is not directly observable but must be inferred from $\theta(t)$.

The first-order temporal Markov model used in this method involves the assumption that

$$p\big(\omega_i(t)\,|\,\omega_j(t-T)\,\omega_j(t-2T)..., \omega_j(T)\big)$$
$$= p\big(\omega_i(t)\,|\,\omega_j(t-T)\big)$$

where p denotes conditional probability. This equation means that the conditional probability of any current state, given knowledge of all previous states, is the same as the conditional probability of the current state, given knowledge of the state at time $t - T$. Hence, assuming stationarity, to calculate the probability of any state at time t, one need know only $p(\omega_i(t)\,|\,\omega_j(t-T))$ plus the initial state probabilities $\pi = p(\omega_1(0), ..., \omega_m(0))$, which can be derived from mean times between failures or other gross failure statistics. The $m \times m$ matrix A,

given by $a_{ij} = p(\omega_j(t)|\omega_i(t-T))$, is known as the transition matrix and characterizes the Markov model. Given A and π, one can calculate the probability of any state at any time t.

The space available for this article does not allow a detailed description of the use of the hidden Markov model. Briefly, one computes the current poste-rior probabilities of the states by a recursive algorithm that involves Bayes' rule, the present feature vector, the immediately preceding posterior probabilities, and the transition matrix. The use of the hidden Markov model thus provides for incorporation of the temporal context in conjunction with traditional classification. The Markov-model approach can reduce the false-alarm rate significantly by taking advantage of any time-domain redundancy that may be present.

This work was done by Padhraic J. Smyth of Caltech for NASA's Jet Propulsion Laboratory. Further information is contained in a TSP [see page 1]. NPO-18946

Synthetic-Aperture Coherent Imaging From a Circular Path

Imaging algorithms are based on exact point-target responses.

NASA's Jet Propulsion Laboratory, Pasadena, California

Algorithms have been developed for use in reconstructing the image of a target from data gathered by a radar, sonar, or other transmitting/receiving coherent-signal sensory apparatus that follows a circular observation path around the target. Potential applications include the following:

- Wide-beam synthetic-aperture radar (SAR) from aboard a spacecraft in circular orbit around a target planet;
- SAR from aboard an airplane flying a circular course at constant elevation around a central ground point, toward which a spotlight radar beam is pointed;
- Ultrasonic reflection tomography in a medical setting, using one transducer moving in a circle around the patient or else multiple transducers at fixed positions on a circle around the patient ; and
- Sonar imaging of the sea floor to high resolution, without need for a large sensory apparatus.

These algorithms include processing steps similar to those of the chirp-scaling algorithm, which has been limited to process SAR data from straight line paths but with a very narrow radar beam angle in along-track. The present algorithm, however, can be applied to circular paths without limitation of the radar beam angle.

The present algorithms process the return-signal data in the two-dimensional Fourier-transform domain. The processing involves multiplication of fast Fourier transforms (FFTs) of the raw data by a reference function derived from the two-dimensional spectrum of the exact range-and-azimuth response of a point target as a function of time. The reference function is the inverse of this two-dimensional spectrum.

The algorithm for processing data from a wide-beam sensory apparatus comprises the following steps:
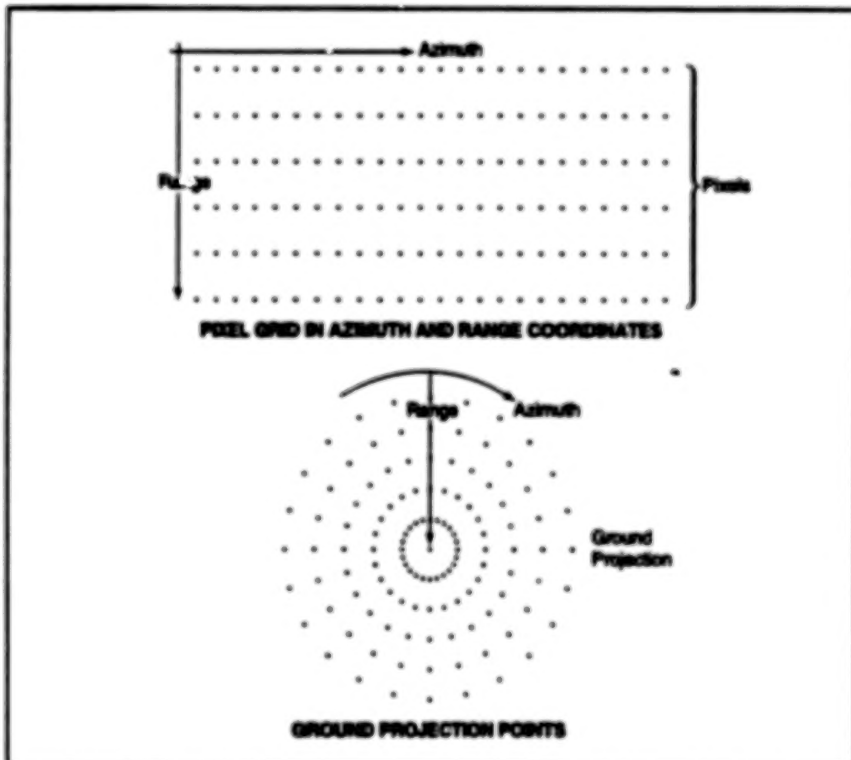
This Plot Shows the Mapping between (a) pixels generated from step 2 of the spotlight algorithm and (b) points on the ground.

1. Compute the raw SAR or other data in the azimuth dimension.
2. Multiply by the phase perturbation for the range curvature (chirp-scaling phase).
3. Compute the FFT in the range dimension.
4. Multiply by the complex (both magnitude and phase) azimuth reference function and by a range-compression-filter function.
5. Compute the inverse FFT in the range dimension.
6. Multiply by the phase correction needed for chirp scaling and for the focusing adjustment made necessary by the variation, along the slant range, of the rate of change of Doppler frequency.
7. Compute the inverse FFT in azimuth dimension.
8. Perform geometric rectification according to a selected projection grid.

The algorithm for processing data acquired with a spotlight beam is similar, except that some of the steps at the beginning and end are modified. The processing steps specific to the spotlight mode are the following:

1. Perform subsampling of echo pulses according to the radius of the spot area. This step is not necessary if the pulse-repetition frequency of the apparatus is tuned to the radius such that there are no redundant data.
2. Perform SAR correlation, using the exact reference function. This step

68

NASA Tech Briefs, March 1995

can be repeated over the same data block, each time tuned to a different subset of the range samples. This is necessary when the depth of focus is particularly small.

3. Perform geometric resampling to correct for the geometry and grid spacing (see figure).

This work was done by Michael Y. Jin of Caltech for NASA's Jet Propulsion Laboratory. Further information is contained in a TSP [see page 1].
NPO-19024

Books and Reports

Reliability-Engineering Manual

This book shows the importance of reliability engineering as a distinct, emerging discipline.

A tutorial book discusses principles and practices of reliability engineering. It begins with a brief historical discussion that illustrates the growing awareness of concepts of reliability and the consequent emergence of reliability engineering as a discipline. It reviews aspects of algebra, calculus, probability theory, and failure physics pertinent to reliability calculations. Mathematical models of reliability based on exponential distributions are explained. Examples of prediction using rates of failure are presented, along with a technique for allocating rates of failure to elements of a system. A discussion of the probability-density and cumulative probability functions [with emphasis on the normal (Gaussian) distribution] provides the basis for analysis of tolerance and wearout failure. Methods of testing for reliability are discussed. Mathematical models of the reliability of software are presented. Types of software, defects in software, and the concept of software quality are presented, followed by a discussion of how software quality is implemented. The final chapter discusses what is involved in setting up a reliability-management program and organization. Practice problems and references to the literature are provided. Appendices provide additional data in the form of tables, graphs, equations, examples of reliability testing, and answers to the practice problems.

This book was compiled by Vincent R. Lalli of Lewis Research Center, and Henry A. Malec of Digital Equipment Corp. along with a team of contributors. Further information may be found in NASA RP-1253 [N92-32456/TB] "Reliability Training."

Copies may be purchased [prepayment required] from the NASA Center for AeroSpace Information, User Services Division, Linthicum Heights, Maryland, Telephone No. (301) 621-0394. Rush orders may be placed for an extra fee by calling the same number.
LEW-15857

Life Sciences

Hardware, Techniques, and Processes

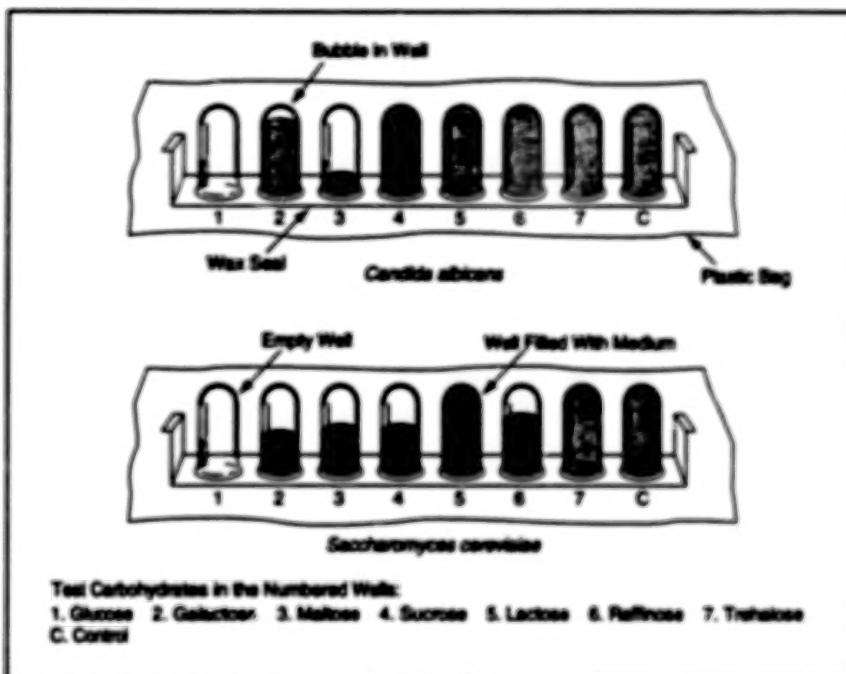# Microfermentation Test for Identification of Yeast

Results can be obtained in days
instead of weeks.

Lyndon B. Johnson Space
Houston, Te

A microfermentation test has been developed as a supplementary method for use in identifying yeasts, especially in clinical and environmental studies. In comparison with traditional fermentation tests, the microfermentation test is simpler and easier, and it requires less equipment, material, and laboratory space. The microfermentation test is also faster; it yields a conclusive result within 3 to 5 days, whereas a traditional fermentation can take 3 to 4 weeks. The greater speed of the microfermentation test can sometimes make a great difference in a clinical setting; in the case of a potentially fatal yeast infection, treatment must be started promptly, and the correct treatment depends on the identification of the yeast species.

The microfermentation test differs from traditional fermentation tests in the details of implementation, but is based on the same principle. The basic idea is that each species of yeast ferments one or more carbohydrate(s), producing carbon dioxide. Thus, an unknown species of yeast in a suspension of cells can be identified by incubating samples of the suspension in media that contain different carbohydrates and looking for the presence (positive result) or absence (negative result) of carbon dioxide after the incubation period.

The microfermentation test is performed in a microtiter plate, which is essentially a plastic strip or plate dimpled with small wells that are numbered for identification. The volume of each well is a fraction of a milliliter. Usually, the microfermentation test is performed with eight different media; a control medium that contains no carbohydrate, and seven media that are similar except that each contains a different carbohydrate. In preparation for the microfermentation test, a microtiter plate of at least eight wells (one well for each medium) is sterilized with ultraviolet light.

Test Carbohydrates in the Numbered Wells:
1. Glucose 2. Galactose 3. Maltose 4. Sucrose 5. Lactose 6. Raffinose 7. Trehalose C. Control

Two Different Species of Yeast — *Candida albicans* and *Saccharomyces cerevisiae* — yielded positive results in different carbohydrate media in a microfermentation test.

The control medium is a basal medium that consists of distilled water containing peptone at a concentration of 7.5×10^{-3} g/mL and yeast extract at a concentration of 4.5×10^{-3} g/mL. Solutions of the seven carbohydrates are prepared, each solution consisting of one of the carbohydrates at a concentration of 8.5×10^{-2} g/mL in distilled water. A volume of 100 μL of the basal medium is placed in each well. Then to each well except the control well, 50 μL of the carbohydrate solution designated for that well is added. Next, 50 μL of the suspension that contains the unknown yeast cells is added to each of the eight wells. Each well is then sealed by pouring 25 μL of a molten, sterile, soft wax into the well on top of the liquid contents.

After allowing the wax to cool, the microtiter plate is placed with the sealed side down in a sterile Ziploc™ (or equivalent) closable plastic bag in an incubator at a temperature of 30 °C. The wells are observed daily for the production of CO_2 gas. In a well with a positive result, part or all of the medium is forced out by the formation of gas, as indicated by a bubble or by complete emptying of the well (see figure). In the control well and in any other well with a negative result, no gas is formed, as indicated by the fact that the well remains completely filled with its liquid medium.

National Aeronautics and
Space Administration

70

END

DATE FILMED

08/24/95